



Improving permafrost physics in the coupled Canadian Land Surface Scheme (v. 3.6.2) and Canadian Terrestrial Ecosystem Model (v. 2.1) (CLASS-CTEM)

Joe R. Melton¹, Diana L. Verseghy^{2,*}, Reinel Sospedra-Alfonso³, and Stephan Gruber⁴

¹Climate Research Division, Environment and Climate Change Canada, Victoria, B.C., Canada

²Formerly at Climate Research Division, Environment and Climate Change Canada

³Canadian Centre for Climate Modelling and Analysis, Climate Research Division, Environment and Climate Change Canada, Victoria, B.C., Canada

⁴Department of Geography and Environmental Studies, Carleton University, Ottawa, Canada

*Retired

Correspondence: Joe R. Melton (joe.melton@canada.ca)

Abstract. The Canadian Land Surface Scheme and Canadian Terrestrial Ecosystem Model (CLASS-CTEM) together form the land surface component of the Canadian Earth System model (CanESM). Here we investigate the impact of changes to CLASS-CTEM that are designed to improve the simulation of permafrost physics. Eighteen tests were performed including changing the model configuration (number and depth of ground layers, different soil permeable depth datasets, adding a surface moss layer), and investigating alternative parameterizations of soil hydrology, soil thermal conductivity and snow properties. To evaluate these changes, outputs from CLASS-CTEM were compared to 1570 active layer thickness (ALT) measurements from 97 observation sites that are part of the Global Terrestrial Network for Permafrost (GTN-P), 105 106 monthly ground temperature observations from 132 GTN-P borehole sites, a blend of 5 observation-based snow water equivalent (SWE) datasets (Blended-5), remotely-sensed albedo, and seasonal discharge for major rivers draining permafrost regions. From the tests performed, the final revised model configuration has more ground layers (increased from 3 to 20) extending to greater depth (from 4.1m to 61.4 m) and uses a new soil permeable depths dataset with a surface layer of moss added. The most beneficial change to the model parameterizations was incorporation of unfrozen water in frozen soils. These changes to CLASS-CTEM cause a small improvement in simulated SWE with little change in surface albedo but greatly improve the model performance at the GTN-P ALT and borehole sites. Compared to the GTN-P observations, the revised CLASS-CTEM ALTs have a weighted mean absolute error (wMAE) of 0.41 - 0.47 m (depending on configuration), improved from > 2.5 m for the original model, while the borehole sites see a consistent improvement in wMAE for most seasons and depths considered, with seasonal wMAE values for the shallow surface layers of the revised model simulation at most 1.2 °C greater than those calculated for the model driving screen-level air temperature compared to observations at the sites. Sub-grid heterogeneity estimates were derived from the standard deviation of ALT on the 1 km² measurement grids at the GTN-P ALT sites, the spread in wMAE in grid cells with multiple GTN-P ALT sites, as well as from 35 boreholes measured within a 1200 km² region as part of the Slave Province Surficial Materials and Permafrost Study. Given the size of the model grid cells (ca. 2.8°), sub-grid heterogeneity makes it likely difficult to appreciably reduce the wMAE of ALT or borehole temperatures much further.



Copyright statement. The works published in this journal are distributed under the Creative Commons Attribution 3.0 License. This licence does not affect the Crown copyright work, which is re-usable under the Open Government Licence (OGL). The Creative Commons Attribution 3.0 License and the OGL are interoperable and do not conflict with, reduce or limit each other.

©Crown copyright 2019

5 1 Introduction

Permafrost underlies between 9 and 14 % of the exposed land surface north of 60°S ($13 - 18 \times 10^6$ km²; Gruber, 2012). The presence of perennially frozen soil at depth has strong impacts on local hydrology, energy fluxes, plant communities, and carbon dynamics. Several factors influence ground temperature and therefore the presence of permafrost, including snow cover, vegetation structure and function, hydrology, and topography (Lorantý et al., 2018). Permafrost has been warming and active layers have thickened over the last three decades (Vaughan et al., 2013). This trend is expected to continue due to climate change (Chadburn et al., 2017) making the carbon presently contained in frozen soils vulnerable to release to the atmosphere either as carbon dioxide or methane, depending on local conditions. Since the carbon stored in frozen soils is only accessible to microbial respiration once soils thaw, accurately simulating the physics of the permafrost response to a changing climate is vital for reliable predictions of the permafrost carbon feedback to climate change.

The Canadian Land Surface Scheme (CLASS) is the land surface component of the Canadian Earth System Model (CanESM). CLASS has been tested for its cold regions performance in several studies previously. Tilley et al. (1997) evaluated CLASS (v. 2.5) at a site on the North Slope of Alaska. The principal conclusions of the study were that CLASS was most sensitive to ground column depth and soil composition with lesser sensitivity to variations in the radiative fluxes, specification of the overlying vegetation and the initial soil moisture. Bellisario et al. (2000) tested CLASS at a fen wetland and a willow-birch forest in the northern Hudson Bay lowlands. They found the upper soil layer temperatures to be consistently overestimated using the model's default mineral soil parameterization, whereas using the organic soil parameterization of Letts et al. (2000) improved the simulated temperatures significantly. Lafleur et al. (2000) did some tests with a subarctic open woodland site in Churchill, Manitoba using CLASS with the Letts et al. (2000) parameterization. Recommendations from their work included introducing a non-vascular plant functional type (PFT) and a sparse canopy representation, varying the minimum stomatal conductance according to PFT, and re-examination of the snow melt algorithm. The snow melt recommendations were subsequently investigated by Bartlett et al. (2006) and Brown et al. (2006). More recently, Paquin and Sushama (2014) used CLASS (v. 3.5) in the Canadian Regional Climate Model version 5 (CRCM5) to look at the impact of snow and soil parameterizations on simulated permafrost and climate. Their simulations included offline tests using the ERA-Interim meteorological forcing over the pan-Arctic region. Paquin and Sushama tested several options that have previously been made available in CLASS, but not yet implemented operationally, including, 1) increasing the number and depth of soil layers (47 levels extending to 65 m), 2) using the Letts et al. (2000) parameterization for peatlands and assuming an organic surface soil layer for most other regions, and 3) changing the snow thermal conductivity parameterization from Mellor (1977) to Sturm et al. (1997). The Sturm et al. formulation was subsequently adopted in CLASS v. 3.6 (Verseghy, 2017). Ganji et al. (2015) also used CLASS in



CRCM5 to investigate cold region hydrological performance. They reported improvements by incorporating supercooled soil water, fractional permeable area, and a changed hydraulic conductivity formulation for frozen soil. MacDonald (2015) coupled CLASS v. 3.6 to the Prairie Blowing Snow Model (PBSM) to simulate the influence of chinooks (Föhn winds) over the South Saskatchewan River Basin. He investigated 15 alternative parameterizations relating to the model physics and concluded by recommending that four be considered for adoption in CLASS to improve the simulated snow water equivalent (SWE) and soil water. Three of the suggested parameterizations dealt with snow properties and the fourth related to soil thermal conductivity (MacDonald, 2015).

Our study evaluates the individual and combined effects of suggested enhancements to the Canadian Land Surface Scheme coupled to the Canadian Terrestrial Ecosystem Model (CLASS-CTEM) for simulating processes relevant to soils with permafrost or pronounced seasonal freezing. The model enhancements suggested above have previously been recommended in research studies but not been previously implemented into the CLASS-CTEM framework (unless otherwise noted). Here we investigate the impact of these previously proposed model enhancements as well as several model configuration changes suggested in the literature. Based on this evaluation, a revised version of CLASS-CTEM, containing several enhancements is described and also evaluated. To evaluate model behaviour we draw upon measurements of the thickness of annual thaw in perennally frozen soils (active layer thickness) and borehole temperature sites from the Global Terrestrial Network for Permafrost (GTN-P, 2016) along with other observation-based datasets for snow, surface albedo and runoff.

Numerous studies have investigated the permafrost physics performance of models (e.g. see review in Riseborough et al., 2008) including other large scale models used in ESM applications, such as JULES (Chadburn et al., 2015a, b), JS-BACH (Ekici et al., 2014), and the Community Land Model (CLM, e.g., Alexeev et al., 2007; Lawrence et al., 2008; Lee et al., 2014) allowing us to design our proposed experiments based on their conclusions. The performance of CLASS-CTEM permafrost physics will be evaluated through offline simulations where the model is forced with reanalysis meteorology to avoid biases found in the simulated climate of the coupled model as well as biases in the associated feedbacks. This study is focused on model performance at the large spatial scale of the CanESM as our principle aim is to improve the simulated permafrost physics so that the carbon cycle processes in these regions is well bounded. It is therefore not aimed at shedding light on physical processes in permafrost zones or investigating model performance at individual point locations as the model performance at a single site does not directly translate to model performance over large regions.

The remainder of the paper consists of three sections. Section 2 describes the CLASS-CTEM model, the study design as well as parameterizations tested, and the GTN-P sites used in model evaluation. Section 3 evaluates the model performance over the 18 experiments as well as discussing the influence of sub-grid heterogeneity while Section 4 gives overall conclusions and discusses limitations of our study and future directions for CLASS-CTEM development.



2 Experimental setup

2.1 CLASS-CTEM

CLASS (v. 3.6.2; Verseghy, 2017) coupled with CTEM (v.2.1; Melton and Arora, 2016) forms the land surface component of the CanESM. CLASS performs the land surface energy and water balance calculations on a, typically, half-hour timestep.

5 The model uses leaf area index (LAI), rooting depth, canopy mass, and vegetation height to evaluate the energy and water balance terms of the vegetation canopy and its interactions with the atmosphere. The number of soil layers can vary depending on the application but the standard model setup uses three soil layers of 0.1, 0.25, and 3.75 m thickness. The soil texture (sand, clay, organic matter) dataset used by CLASS-CTEM is the Global Soil Dataset for use in Earth System Models (GSDE; Shangguan et al., 2014). The soil permeable depth is from Zobler (1986) (hereafter Zobler86). The GSDE uses a standardized

10 data structure and processing procedures to harmonize and integrate the Soil Map of the World along with various national and regional soil databases (Shangguan et al., 2014). CLASS v.3.6.2 adopts the soil albedo approach of Lawrence and Chase (2007) with the incorporation of a soil colour index geophysical field. The twenty soil colour indices were derived by minimizing the difference between modelled soil albedo and MODIS satellite observed surface albedo (Lawrence and Chase, 2007).

CLASS prognostically determines the water content (liquid and frozen) and temperature of all soil layers at each timestep.

15 Also calculated at each timestep, depending on ambient conditions, are the temperature, mass, albedo, and density of a single layer snow pack, interception of rain and snow on the vegetation canopy, and amount of ponded water on the soil surface. Mineral soils are parameterized using the pedotransfer functions of Cosby et al. (1984) and Clapp and Hornberger (1978). Organic soils (organic matter >30% by weight) are modelled as peat following Letts et al. (2000). In the standard CLASS-CTEM framework, lateral transfers of heat or moisture between grid cells are neglected; the treatment of processes such as

20 streamflow and blowing snow require the inclusion of separate, specialized routines (e.g., Soulis et al., 2000; Arora et al., 2001; MacDonald, 2015). All simulations presented here have no geothermal heat flux at the bottom of the soil column.

CTEM calculates the carbon and vegetation dynamics on a daily timestep receiving from CLASS daily mean soil moisture, soil temperature, and net radiation. Photosynthesis and canopy conductance occur on the CLASS timestep. CTEM simulates the respiratory costs and carbon uptake for nine plant functional types (PFTs) which are subsets of the four CLASS PFTs.

25 The CLASS PFTs (with corresponding CTEM PFTs in parentheses) are needleleaf tree (needleleaf deciduous and needleleaf evergreen), broadleaf tree (broadleaf cold deciduous, broadleaf drought/dry deciduous, and broadleaf evergreen), crop (photosynthetic pathway C3 and C4), and grass (C3 and C4). CTEM carries five carbon pools representing plant leaves, roots, and stems along with two detrital pools for litter and soil C.

For global simulations, CLASS-CTEM is typically run at the CanESM atmosphere resolution which is approximately 2.8°

30 by 2.8° corresponding to a grid cell size of approximately 49 000 km² at 45° latitude and about 33 500 km² at 70°. Various studies have used observation-based datasets to evaluate CLASS-CTEM at scales from site-level to global (e.g., Peng et al., 2014; Melton and Arora, 2014, 2016). While CLASS-CTEM is capable of running in a mosaic (multiple tiles per grid cell) configuration, (e.g. Melton and Arora, 2014; Melton et al., 2017), the simulations presented here are run with a single tile per grid cell.



2.2 Study design

Eighteen experiments were run to assess the impact of model geophysical fields (soil texture, soil permeable depth, and meteorological forcing), model setup (number of soil layers, addition of a moss layer), and model parameterizations. The experiments are listed in Table 1. The physical quantities used for model evaluation are presented in the next section. The initial model version (Exp. 'Base model') uses 3 ground layers of thicknesses 0.1, 0.25, and 3.75 m for a total depth of 4.1 m. The first seven experiments address model configuration and input geophysical fields. To test the sensitivity of simulated permafrost to meteorological forcing, CLASS-CTEM was forced with two different meteorological datasets, the Climate Research Unit - National Centres for Environmental Prediction (CRUNCEP v. 8; Viovy, 2016) and the Climate Research Unit - Japanese 55 year Reanalysis (CRUJRA55 v. 1.0.5; Harris et al., 2014; Kobayashi et al., 2015). CRUNCEP was used as the base forcing dataset with additional runs performed for some experiments with CRUJRA55 (see Table 1). While both of these meteorological datasets use the CRU TS dataset (Harris et al., 2014) as the underlying monthly climatology, they differ in their meteorological models (NCEP or JRA55). Additionally the spatial resolution of JRA55 is 0.5° while that of NCEP is 2.5° . Thus, the two datasets differ in their spatial and high frequency (sub-monthly) temporal variability. However these differences will be somewhat lessened by their regriding to the CLASS-CTEM model resolution. The meteorological inputs (surface air temperature, surface pressure, specific humidity, wind speed, precipitation, and longwave and shortwave radiation) are disaggregated from 6 hourly to half-hourly time steps while the simulation runs following the methodology in Melton and Arora (2016). Both datasets are available over the extended periods necessary for permafrost simulation (CRUNCEP v. 8: 1901 - 2016, CRUJRA55 v. 1.0.5: 1901 - 2017).

Exp. '20 ground layers' changes the number of ground layers from 3 to 20. The 20 layers have higher resolution near the surface with thicker layers at depth (see Table A1). If the permeable soil depth is shallower than the modelled ground column, layers below the soil permeable depth are treated like hydrologically inactive bedrock and are assigned thermal conductivity ($2.5 \text{ W m}^{-1} \text{ K}^{-1}$) and heat capacity ($2.13 \times 10^6 \text{ J m}^{-3} \text{ K}^{-1}$) values characteristic of sand particles (Verseghy, 2017). If the transition from permeable soil to impermeable bedrock occurs within a soil layer, CLASS calculates the water fluxes only in the depth of permeable soil but simulates one soil temperature for the layer.

The influence of the soil permeable depth dataset is examined by replacing the soil permeable depths of Zobler86 with either the SoilGrids dataset (Exp. 'SoilGrids depth', Shangguan et al., 2017) or that of Pelletier et al. (2016) (hereafter referred to as Pel16; Exp. 'Pel16 depth'). Both SoilGrids and Pel16 have significantly deeper soil permeable depths than Zobler86 (Figure A1). The influence of a moss layer is examined in Exp. 'SoilGrids+Moss' and 'Pel16+Moss'. In these experiments the top soil layer is characterized as photosynthetically-inactive moss with a higher porosity, hydraulic conductivity and heat capacity than mineral soil following Wu et al. (2016). The moss layer is applied to all locations as we are not aware of any global dataset quantifying the spatial distribution of moss.

The second series of experiments used the 'SoilGrids+Moss' experiment as a starting point - thus all geophysical fields and model configurations were the same as in SoilGrids+Moss. As described in the Introduction, several recent studies have proposed recommendations for new parameterizations in CLASS-CTEM to enhance cold-regions performance. The second series



Table 1. List of experiments and the associated model theme they relate to. Experiments denoted with an asterisk were run with both the CRUNCEP and the CRUJRA55 meteorological forcing datasets.

Experiment name	Theme	Description	Starting model configuration
Base model		Original model setup	
20 ground layers	Configuration	Twenty ground layers to a maximum depth of 61.5 m (see Table A1)	Base model
SoilGrids depth	Configuration	Soil permeable depth geophysical field (SoilGrids; Shangguan et al., 2017)	20 ground layers
Pel16 depth	Configuration	Soil permeable depth geophysical field (Pel16; Pelletier et al., 2016)	20 ground layers
SoilGrids+Moss*	Configuration	SoilGrids depth setup with first soil layer treated as non-photosynthetic moss layer following Wu et al. (2016)	SoilGrids depth
Pel16+Moss*	Configuration	Setup as above but with Pel16 depths	Pel16 depth
deVries thermal cond.*	Heat transfer	Soil thermal conductivity following de Vries (1963)	SoilGrids+Moss
Tian16 thermal cond.	Heat transfer	Soil thermal conductivity following Tian et al. (2016)	SoilGrids+Moss
Snow cover:Yang97*	Snow	Snow depth to fractional snow cover relation following Yang et al. (1997)	SoilGrids+Moss
Snow cover:Brown03	Snow	Snow depth to fractional snow cover relation following Brown et al. (2003)	SoilGrids+Moss
Fresh snow density	Snow	Fresh snow density based on air temperature and wind speed following CROCUS as detailed in Essery et al. (1999) with a minimum density of 50 kg m^{-3} following MacDonald (2015)	SoilGrids+Moss
Snow albedo decay	Snow	Efficient spectral snow albedo decay (Dickinson et al., 1993)	SoilGrids+Moss
Super-cooled water	Hydrology	Unfrozen water in frozen soils (super-cooled soil water) following Niu and Yang (2006)	SoilGrids+Moss
Modif. hydrology	Hydrology	Soil matric potential and effective saturated conductivity are modified for the influence of frozen water as described in Ganji et al. (2015)	SoilGrids+Moss

of experiments examines these recommendations, which are described in detail in Appendix sections A1 to A6. Briefly, these experiments fall into three main areas related to: 1) heat transfer, 2) snow, and 3) hydrology. The heat transfer experiments replace CLASS-CTEM's default soil thermal conductivity parameterization (Côté and Konrad, 2005) with that of de Vries (1963) following the recommendations of MacDonald (2015)(Exp. 'deVries thermal cond.'). As de Vries (1963) does not account for frozen water in soil, whereas (Côté and Konrad, 2005) does, a further experiment uses a recently published parameterization that simplifies and extends de Vries (1963) to include both frozen and unfrozen water (Exp. 'Tian16 thermal cond.'). See Section A1; Tian et al., 2016). Four experiments were devoted to aspects of how snow is simulated in CLASS-CTEM. Experiments 'Snow cover:Yang97' and 'Snow cover: Brown03' replace CLASS-CTEM's default function to relate snow depth to grid cell fractional snow cover from a linear relationship (Verseghy, 2017) to a hyperbolic tangent (following Yang et al.,



1997) or an exponential function (following Brown et al., 2003), respectively (Figure A2). Another experiment ('Fresh snow density') changed the calculation for the density of freshly-fallen snow from one based solely on air temperature (Verseghy, 2017) to also considering wind speed following the CROCUS model (Essery et al., 1999). The final experiment concerned with aspects of the snow parameterization is 'Snow albedo decay'. CLASS-CTEM uses an empirical exponential decay function to simulate the decrease in snow albedo as snow ages. In 'Snow albedo decay', the default parameterization is replaced by an efficient spectral method (Wiscombe and Warren, 1980; Dickinson, 1983). The last series of experiments looked at hydrology. Water in soils can be, partially or completely, unfrozen at temperatures below 0°C due to the effects of interfacial curvature, adsorption forces and solutes (Watanabe and Mizoguchi, 2002; Dall'Amico et al., 2011). Experiment 'Super-cooled water' incorporated the unfrozen water in frozen soils parameterization of Niu and Yang (2006) and Exp. 'Modif. hydrology' modifies the soil matric potential and saturated hydraulic conductivity to account for the influence of frozen water following Ganji et al. (2015).

For model spinup, the meteorological forcing years of 1901 – 1925 were cycled over repeatedly until the model reached active layer thickness (ALT) equilibrium (less than 0.05 m difference between average ALT between spinup cycles across all cells with permafrost within them). To run from 1851 to 2016, the climate was cycled over twice from 1901 to 1925 for the years 1851–1900, then the model was allowed to run freely from 1901 to 2016. For the simulations presented here, CLASS-CTEM was run with a prescribed, rather than prognostically determined distribution of PFTs.

Active layer thickness in CLASS-CTEM is determined by the temperature and water content of the ground layers. If a layer's temperature is 0°C, the frozen water fraction is used to estimate the thickness of freezing within the layer, i.e., if half of the water content in the layer is frozen, the ALT is assumed to be halfway through the layer. Permafrost area in the model domain was calculated by selecting grid cells with active layer thicknesses less than the model total ground column and multiplying by the grid cell area.

2.3 Datasets used for model evaluation

We evaluate the CLASS-CTEM simulations against measurements of the thickness of annual thaw in perennially frozen soils and borehole temperature sites from the GTN-P along with other observation-based datasets for snow, surface albedo and runoff. We also compare to published estimates of permafrost spatial coverage.

2.3.1 Active layer thickness sites from the Global Terrestrial Network for Permafrost (GTN-P)

To evaluate CLASS-CTEM, data from 97 open access ALT sites were downloaded from the GTN-P (2016) (accessed May 11th, 2017; Table A2 and Figure 1). These sites were chosen due to their locations in regions of continuous or discontinuous permafrost. No sites in areas of sporadic or isolated permafrost were used due to the difficulty in representing this type of permafrost within a large model grid. While we attempted to have as broad a spatial coverage of the GTN-P sites as possible, no open access sites were available for Eastern Canada and Fennoscandia. For comparison with CLASS-CTEM, at each observation time, the average of the sampling grid was determined at each GTN-P ALT site. Then for each site, the sampling grid averages were converted to monthly mean values. The closest CLASS-CTEM grid cell to the ALT site's location was



selected and the modelled monthly average ALTs were compared to the observed values. This resulted in the 97 GTN-P sites, with 1570 ALT observations, being placed into 37 CLASS-CTEM grid cells. As multiple GTN-P sites can be co-located in one CLASS-CTEM grid cell, the weighted mean absolute error (wMAE) for a grid cell was found by averaging the MAE calculated at each site situated within one CLASS-CTEM grid cell.

5 2.3.2 Borehole temperatures from the GTN-P

Borehole data from the GTN-P were downloaded for 132 open-access sites found in the permafrost (including continuous, discontinuous, sporadic, and isolated) or permafrost-free domains (accessed May 11th, 2017). Most of the boreholes are in Eurasia with few in North America. Each site has its own unique time period of observations and number and depth of observations. At each site, the depths of borehole temperatures were selected to be within 0.05 and 3.0 m of the ground surface, missing values
10 were filtered out, and the observations were averaged to monthly values. For each borehole and each observation depth, the CLASS-CTEM output was selected for the nearest grid cell and the same month as the observations. Linear interpolation was then used to determine the simulated soil temperature for the same soil depth as the observation. The boreholes and number of observations at each are listed in Table A3. As with the ALT sites, several steps were needed to avoid biasing the comparison with CLASS-CTEM. First, borehole sites co-located in the same CLASS-CTEM grid cell were flagged. The 132 borehole
15 sites are located in 73 unique CLASS-CTEM grid cells. Secondly, the number of observations varied by borehole site so when calculating the kernel density estimates (KDE; presented later) within a model grid cell each observation was weighted by the total number of observations per grid cell. Thus grid cells with many GTN-P borehole sites will have each observation weighted less than sites with fewer observations so each grid cell contributes equally to the KDE estimation and the calculation of wMAE.

20 2.3.3 Snow, albedo and runoff

Snow water equivalent (SWE) from CLASS-CTEM is compared to the Blended-5 dataset for the period from January 1981 to December 2010. Blended-5 is a multi-dataset SWE product developed by Mudryk et al. (2015) that combines five observation-based SWE datasets. Our analysis is limited to regions northward of 45°N with climatological SWE > 4 mm to avoid regions of ephemeral snow. Simulated land surface albedo is compared to the MODIS MCD43C3 white-sky albedo (MODIS Adaptive
25 Processing System, NASA, 2016) for the period spanning February 2000 to December 2013. Similar to SWE, we limit our analysis to regions northward of 45°N. We compared our simulated seasonal runoff to measured discharge rates for seven major river basins that drain permafrost regions for the period from 1965 to 1984 (Ob, Volga, Lena, Yenisei, Yukon, Mackenzie, and Amur rivers; UNESCO Press, 1993). This comparison is limited to seasonal discharges since the CLASS-CTEM runoff is not routed, thus the timing of transport of the water from each grid cell to the river mouth is neglected. On a seasonal timescale
30 this should not cause serious errors but the results must be interpreted with caution.



2.3.4 Permafrost distributions from the literature

Because permafrost cannot easily be observed spatially and reliable data are sparse, global or continental-scale simulation results are often compared to estimates of permafrost distributions. Most prominently, this is the “Circum-Arctic map of permafrost and ground-ice conditions” (Brown et al., 1997) that distinguishes zones of permafrost extent at a scale of 1:10 000 000. These zones are based on expert assessment and manual delineation, often following isotherms of mean annual air temperature. Here, we use *permafrost extent* to refer to the fraction (0 - 1) of the surface that is underlain by permafrost within a pixel or a polygon, *permafrost area* to the actual area (km²) underlain by permafrost and *permafrost region* is used to denote the area (km²) where some proportion of the ground can be expected to contain permafrost. The permafrost region is commonly taken to include areas with a permafrost extent exceeding some threshold (Zhang et al., 2000; Gruber, 2012). These definitions are relevant because CLASS-CTEM produces a binary result, i.e., permafrost is present or absent in a cell, and the classes (Zhang et al., 2000; Brown et al., 1997) and the continuous index (Gruber, 2012) of permafrost extent that are used for comparison need to be interpreted appropriately. Neglecting aggregation effects (Giorgi and Avissar, 1997), which arise when the average fine-scale behaviour of a simulated environmental variable is not equal to the simulated coarse-scale behaviour, a threshold of permafrost extent at 50% provides a first estimate of the region that should be compared with a model producing a binary result. For example, environmental conditions that give rise to a permafrost extent of 60% would likely be considered to have permafrost in the binary model and their area would be counted as having permafrost entirely (rather than only 60% of it). Similarly, conditions that produce a permafrost extent of 40% would likely result in not having permafrost in a binary model. As a consequence, we use the total area of all polygons or pixels with an expected permafrost extent larger than 50% as the appropriate area to compare with the results from CLASS-CTEM, termed ‘region_50’. This includes continuous and extensive discontinuous permafrost in the Brown et al. map totalling to 15 Mkm² (Zhang et al. 1999) and a similar number can be interpreted from a plot of permafrost zonation index and permafrost region (Gruber, 2012).

3 Results and Discussion

3.1 Comparison against GTN-P ALT sites: sites with no simulated permafrost

A first simple test of permafrost performance for CLASS-CTEM is to check whether the GTN-P ALT sites are in fact simulated as containing permafrost. Given that CLASS-CTEM is being run on the CanESM grid (ca. 2.8°), it is possible that site conditions such as meteorology, orography, or vegetation at the GTN-P ALT measurement sites could be quite dissimilar to those of the nearest grid cell, which covers many thousands of km². In such cases, CLASS-CTEM could simulate no permafrost where some permafrost indeed exists. Per experiment, the number of sites with no permafrost simulated are listed in Table 2. These ALT sites were removed from further analysis as the ALT in sites without permafrost is not defined. Most experiments had between six and eight observation sites (corresponding to 4 to 6 grid cells) incorrectly simulated as permafrost-free (ISPF). The ‘Base model’ experiment has significantly more sites ISPF at 15, corresponding to 2 or 3 more grid cells. In general, for the same experiment, the CRUJRA55 meteorological forcing results in fewer grid cells ISPF than CRUNCEP. Small differences

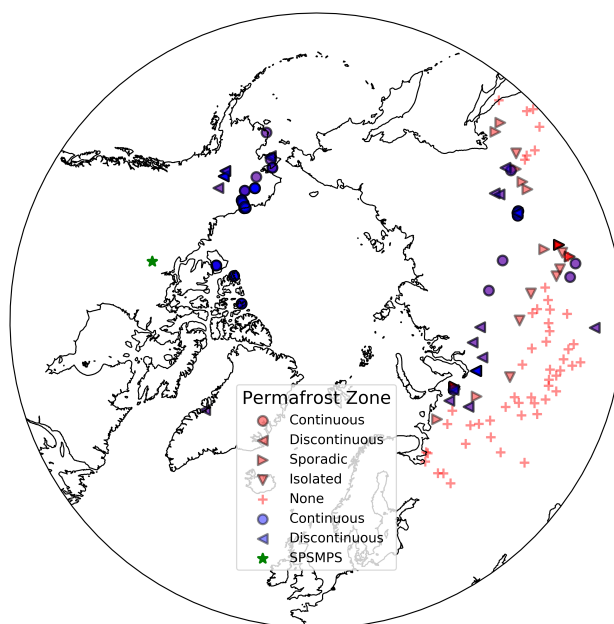


Figure 1. Locations of the 97 GTN-P ALT sites (blue; Table A2), 132 GTN-P borehole observation sites (red; Table A3) and the Slave Province Surficial Materials and Permafrost Study (green; SPSMPS; Lac de Gras, Northwest Territories, Canada) used for model evaluation. Each site is classified according to its permafrost zone listed in the GTN-P. The site markers are semi-transparent hence regions with many closely located GTN-P sites will cause overlap, and darkening, of the markers.

in the simulated presence of permafrost (or the number of sites ISPF) are to be expected given the possibility of errors in the meteorological forcing and local variations in site-level characteristics, but large differences can indicate problems with the model setup and parameterizations.

3.2 Initial model performance

- 5 The 'Base model' experiment simulates a permafrost area (PA) of 8.6 Mkm² (north of 60° S; Table 2) with permafrost confined to northern Siberia, Alaska and the northern edge of Canada (Figure 2). This low PA is in line with that simulated by CLASS-CTEM when coupled within the CanESM, although the spatial distribution is different due to the different atmospheric forcing (Koven et al., 2013). Also plotted in Figure 2 is the PE estimate of Brown et al. (1997). The Brown et al. (1997) dataset gives permafrost spatial distribution in four classifications which are not directly comparable to ALTs but may be used to give
- 10 a general indication of PA from an independent estimate. Owing to the coarseness of the model grid CLASS-CTEM is not able to simulate isolated or sporadic permafrost, but comparing the estimated distribution of discontinuous and continuous permafrost to the modelled ALT indicates poor agreement.

With such a small permafrost area many of the GTN-P ALT sites were ISPF as mentioned above. Of the GTN-P ALT sites where CLASS-CTEM simulated permafrost, the 'Base model' simulations show overly shallow ALTs with an average mean



Table 2. Permafrost area as simulated by CLASS-CTEM (average of 1996 - 2015) along with literature estimates for terrestrial permafrost north of 60°S. The number of GTN-P sites which CLASS-CTEM incorrectly simulated as permafrost free (ISPF) is also listed along with the number of corresponding grid cells in square brackets. These GTN-P sites were removed from further analysis since ALT is not defined in locations with no permafrost. The numbers in parentheses indicate the values when CRUJRA55 was used as the meteorological forcing instead of CRUNCEP. See Section 2.3.4 for distinction between permafrost area and permafrost region.

Experiment	Permafrost Area (10^6 km ²)	Number of sites [grid cells] ISPF
Base model	8.6	15 [8]
20 ground layers	16.7	7 [5]
SoilGrids depth	15.7	8 [6]
Pel16 depth	15.7	8 [6]
SoilGrids+Moss	17.9 (19.8)	7 (6) [5 (4)]
Pel16+Moss	18.5 (19.8)	7 (6) [5 (4)]
deVries thermal cond.	16.2 (17.8)	8 (6)[6 (4)]
Tian16 thermal cond.	21.2	6 [4]
Snow cover: Yang97	19.3 (20.8)	6 (6) [4 (4)]
Snow cover: Brown03	19.0	6 [4]
Fresh snow density	18.9	6 [4]
Snow albedo decay	15.6	6 [4]
Super-cooled water	20.1	6 [4]
Modif. hydrology	19.5	6 [4]
Literature estimates	Permafrost Area (10^6 km ²)	
Zhang et al. (2000)	12.2 - 17.0	
Gruber (2012)	12.9 - 17.7	
Literature estimates	Permafrost Region (10^6 km ²)	
Zhang et al. (1999)	22.8	
Gruber (2012)	21.7 with a range of 18.7 to 24.3	

absolute error (MAE; described in Section 2.3) of 0.410 m. Thus it appears the modelled soil temperatures are too warm in the more southerly permafrost domain (PD), leading to no permafrost simulated, and too cool at the higher latitudes. The 'Base model' experiment also has increasing bias with depth for the 29 sites with permafrost (Figure 3). However, it should be noted that the model configuration of 3 ground layers in this experiment makes an accurate estimation of the ALT difficult since the lowest model layer is quite thick (3.75 m).

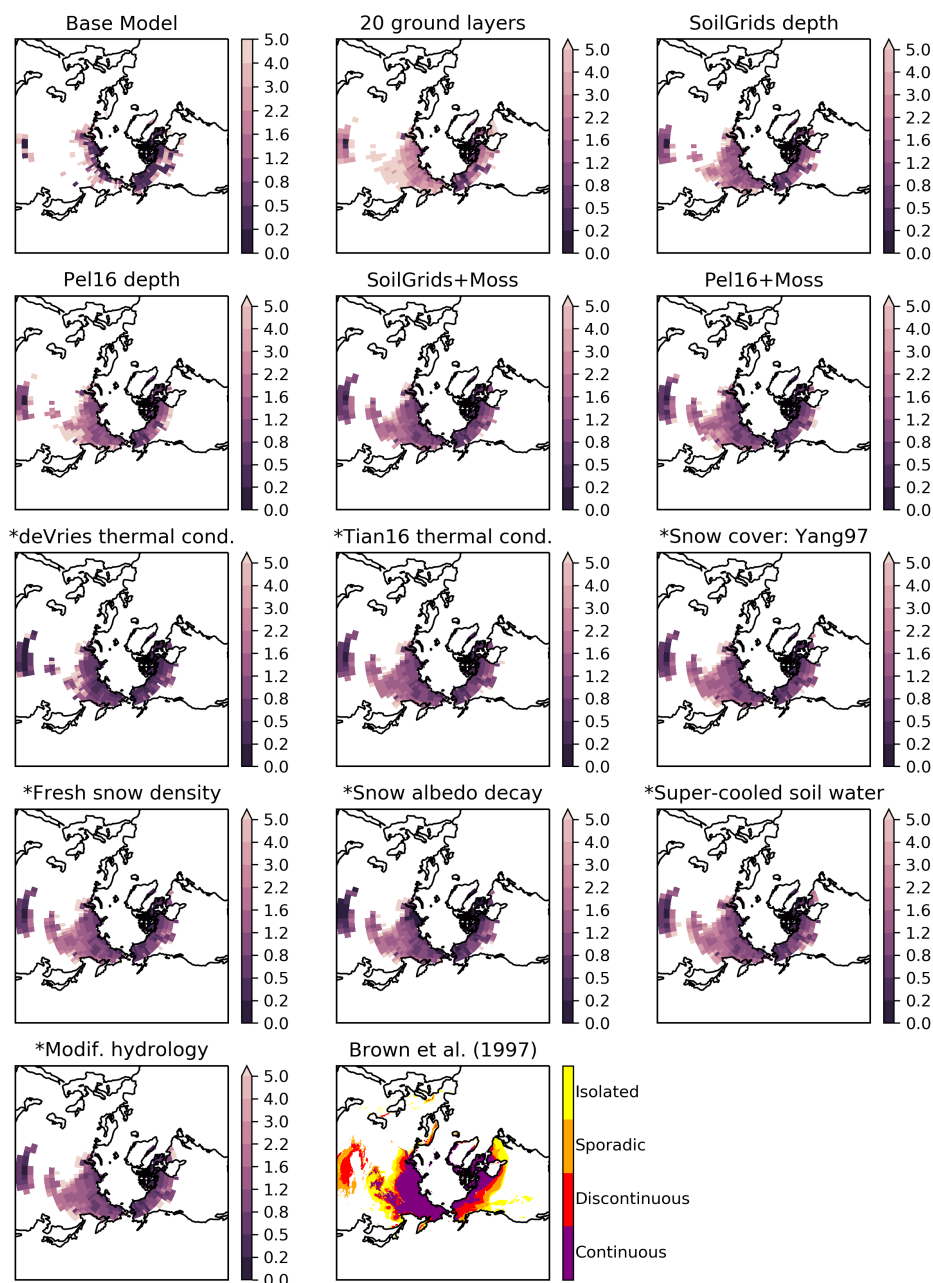


Figure 2. ALTs in meters for experiments listed in Table 1 alongside the permafrost map of Brown et al. (1997) (bottom right). Experiments with an asterisk prefixing their name use a model configuration based on the 'SoilGrids+Moss' setup. All experiments shown here use CRUNCEP for the meteorological forcing.



3.3 Increasing the number of ground layers

Increasing the number of ground layers from 3 to 20 decreases the number of GTN-P ALT sites ISPF from 15 to 7 (Table 2). Figure 4 shows the difference between the simulated and observed ALT at each grid cell with GTN-P ALT sites for selected experiments. The average MAE computed against the GTN-P ALT observations for 'Exp 20 ground layers' is over 2.5 m with simulated ALTs strongly overestimated (Figure 4). When the number and depth of ground layers is increased, but the soil permeable depth is left unchanged, CLASS-CTEM simulates the ground layers below the permeable soil depth as impermeable bedrock. The absence of water and therefore of heat consumption by melting ice in these lower ground layers causes the model soil column to be generally too warm. However, the total global PA increases from 8.6 Mkm² simulated by the 'Base model' to 16.8 Mkm² (Table 2) with an increase in permafrost area primarily in the southern fringes of eastern Siberia and Canada along with a general deepening of ALT across the high latitudes (Figure 2). This seeming incongruity of warmer soils with a larger permafrost area likely relates to moving the boundary of zero heat flux from 4.1 m, a depth where seasonal temperature variations can penetrate, to 61.4 m. The shallower modelled soil column in the 'Base model' inhibits the formation of permafrost because of the concentration of the annual heat flux oscillation in the upper few meters of the soil. In the PD for the '20 layers' simulation, there is a slight general increase in sensible heat flux compared to the 'Base model' simulation (Figure A3). Changes in latent heat flux, leaf area index (LAI) and annual runoff are significant but spatially heterogeneous across the permafrost zone. Increasing the number of soil layers and depth of the zero flux boundary reverses the bias trend in ALT with higher bias at shallower ground depths (Figure 3), although these differences should be interpreted with caution due to the difference in number of ALT sites included in this analysis between the 'Base model' and '20 ground layers' simulations.

The wMAE calculated for each season from CLASS-CTEM's simulated ground temperatures compared to GTN-P borehole temperatures for three depth zones shows an improvement at all depths and seasons for '20 layers' over 'Base model' (Figure 5). Generally, across all experiments, CLASS-CTEM performs better with increasing depth. Seasonally, winter is generally simulated best with summer showing the highest wMAE values. These patterns indicate that the largest challenges to accurate ground temperature simulation are coming from the high variability in forcing at the land surface and from the difficulty in accurately the summertime heat pulse into the ground column.

To look in closer detail at the model performance for the GTN-P borehole sites, Figure 6 shows the Gaussian kernel density estimate (KDE) derived from differences between the simulated and observed borehole temperatures. For shallow soils, as the seasons progress from winter to fall, the proportion of instances with a strong cold bias decreases with a warm soil bias taking over in summer, especially in the shallowest depth band. This would indicate the modelled soil heat fluxes are somewhat exaggerated. The fall period generally has the least bias, potentially due to the loss of the warm summer bias but prior to the establishment of the cold winter bias.

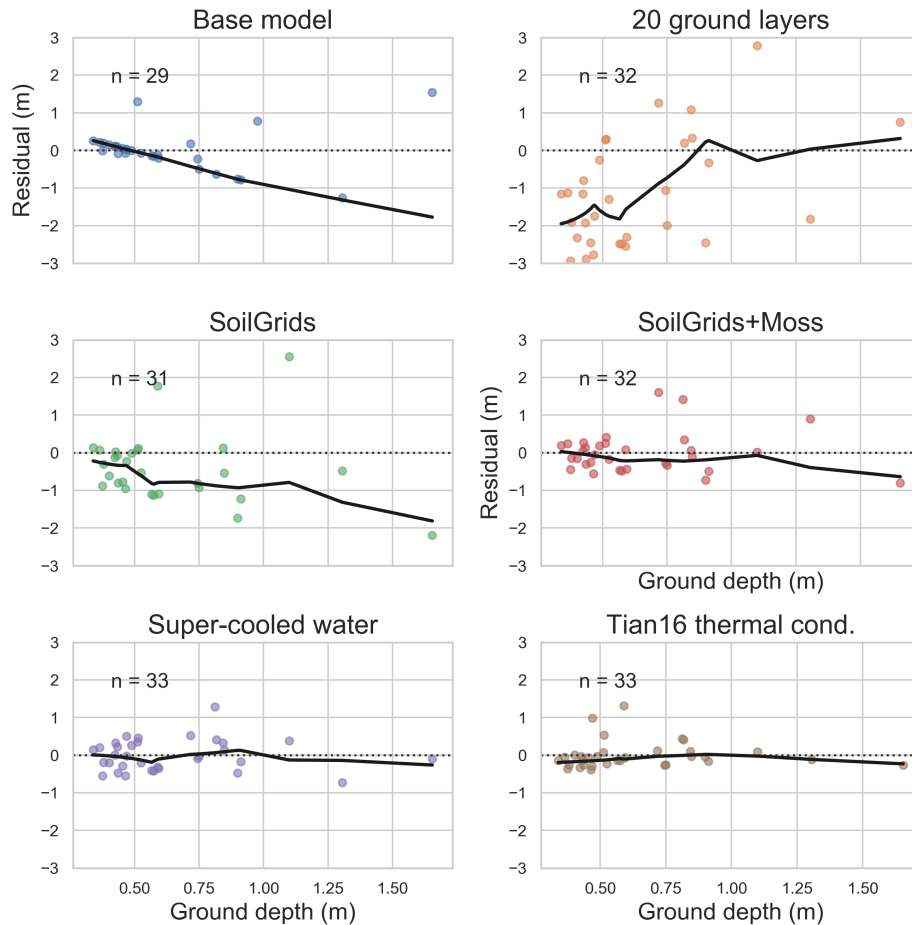


Figure 3. The residuals of a linear regression of the CLASS-CTEM ALTs on the GTN-P ALTs for selected experiments. Each dot is the mean residual for all GTN-P site(s) that fall within a CLASS-CTEM grid cell. The number of grid cells differs between experiments due to sites being ISPF. Black curves are a LOWESS smoother applied to the residuals. For clarity all experiments are plotted with the same axis limits.

3.4 Increasing the soil permeable depths

Changing the soil permeable depth dataset to SoilGrids (Exp. 'SoilGrids depth') from Zobler86 gives a general improvement over the '20 ground layers' simulations with a drop in average MAE to 1.162 m at the GTN-P ALT sites (Figure 4). The residuals calculated against the GTN-P ALT sites (Figure 3) now show a general trend of increasing bias with increasing soil depth, similar to the 'Base model' simulation. There is also a shift to shallower ALTs (Figure 2) with a slight decrease in PA to 15.7 Mkm², which is within the range literature estimates (Table 2 and discussed further in Section 2.3.4). Compared to the '20 ground layers' simulation for the permafrost region, there is a decrease in latent heat flux for much of eastern Siberia and LAI shows strong decreases while runoff increases (Figure A4). The greater permeable depths associated with SoilGrids



lead to deeper penetration of water into the soil, resulting in more water being allocated to runoff than made available for plant transpiration or soil evaporation. Simulations with the alternative soil permeable depth dataset ('Pel16 depth') generally show similar patterns of latent heat flux, runoff and LAI (not shown) to the 'SoilGrids depth' experiment. The 'Pel16 depth' simulations have better agreement with the GTN-P ALT observations reducing the wMAE to 0.757 m (Figure 4). 'SoilGrids' also further improves the model's performance at all depths and seasons compared to the GTN-P borehole sites (Figure 5).

Numerous studies have pointed to the importance of increasing the simulated ground column depth and number of ground layers to better capture the decay with depth of the influence of multi-decadal variability (e.g. Smerdon and Stieglitz, 2006; Alexeev et al., 2007; Nicolsky et al., 2007; Paquin and Sushama, 2014). Of particular relevance to our study, Paquin and Sushama (2014) used CLASS in CRCM5 and found shallow soil configurations (permeable depth < 1 m throughout much of the model domain) to lead to overly strong seasonal cycles with resulting overly deep ALTs, similar to the work of Smerdon and Stieglitz (2006), and in line with our 'Base model' simulation with its small estimated PA.

The availability of comprehensive global soil permeable depth datasets is relatively recent. Previous studies would often assume a constant permeable soil depth, either shallow (Dankers et al., 2011) or deep (Lawrence et al., 2008) with the deeper layers hydrologically inactive. Comparing the three permeable depth datasets (Zobler86, SoilGrids, and Pel16; Figure A1) shows Zobler86 to be by far the shallowest while SoilGrids and Pel16 disagree on the spatial distribution of the permeable depths for the high latitude regions. Pel16 shows deep soils in the Canadian boreal forest, Finland and central southern Russia with shallower soils in the Siberian plateau. SoilGrids has more very deep soils (>50 m) especially in the West Siberian region and the Urals. These differences in permeable depth have an impact on the simulated ALT as the SoilGrids and Pel16 experiments perform quite differently at the GTN-P ALT sites (Figure 4) due to the strong impact of freezing and thawing of water in the soil column.

3.5 Adding an upper layer of organic matter/moss to the soil column

CLASS-CTEM ALTs with both Pel16 and SoilGrids are generally biased deeper than observed at the GTN-P sites (Figure 4) indicating that the ground surface is either overly insulated from the cold atmosphere during the winter or is absorbing too much heat during the summer months. The principal modulating influences on ground heat fluxes in cold regions are hydrology, snow cover (both of which we deal with later), vegetation structure and function, and topography (Loranty et al., 2018). Vegetation canopies shade the soil surface, attenuating radiation and reducing warming in the summer season. As well dense forests capture snow in the canopy which prevents it from reaching the ground and insulating the soil surface further cooling soils. Another aspect of vegetation influence is the insulating effect of a surface layer of moss or organic matter. Mosses are generally more abundant at high latitudes and have been shown to decrease growing season surface soil temperatures (Turetsky et al., 2012). The effect of mosses on the ground heat flux has also been demonstrated through field experiments (Gornall et al., 2007; Van Der Wal and Brooker, 2004) and modelling studies have incorporated organic layers (e.g. Lawrence et al., 2008; Paquin and Sushama, 2014) or bryophytes (Porada et al., 2016) to improve permafrost dynamics. Exps. 'SoilGrids+Moss' and 'Pel16+Moss' both incorporate a non-photosynthetic moss layer in place of the first layer of soil (see Section 2.2) and both simulate generally shallower ALTs than their parent simulations ('SoilGrids depth' and 'Pel16 depth', respectively; Figure 2).

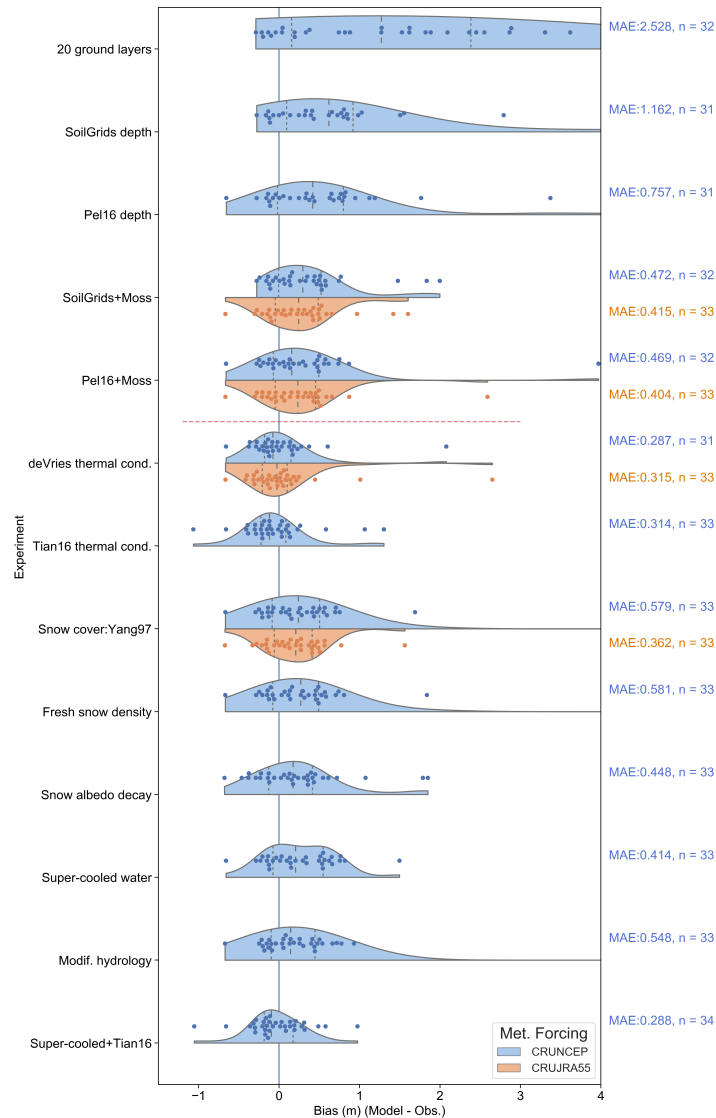


Figure 4. Differences between the ALTs from the experimental model runs and those of the Global Terrestrial Network for Permafrost ALT sites (Table A2). Each dot represents a grid cell with one or more GTN-P sites (see Section 2.3). In this representation (a 'bee swarm'), displacement in the y-direction is only to allow each data point to be visible. The background shading is a Gaussian kernel-density estimate (KDE) with the quartiles of the distribution indicated by dashed vertical lines within the KDE plot. The mean absolute error (MAE) is produced by calculating the MAE at each grid cell and taking the average across all cells. As the number of sites ISPF differs between experiments (Table 2) the number of grid cells where CLASS-CTEM simulated permafrost is also listed. The total number of grid cells with GTN-P sites is 37. The two meteorological forcings are shown for the experiments where the CRUJRA55 forcing was also used. Experiments below the dashed red line use the model setup from Exp. 'SoilGrids + Moss' as their starting point (Table 1).



The effect of moss introduction for the 'SoilGrids+Moss' experiment is to reduce average MAE from 1.162 to 0.472 m for the GTN-P sites (Figure 4) with a reduced increase in bias with soil depth (Figure 3). The general cooling influence is evident by comparing to the GTN-P ALT sites (Figure 4) and also through the increase in simulated PA from 15.7 to 17.9 Mkm². A similar improvement is seen for Exp 'Pel16+Moss' where the average MAE drops from 0.757 to 0.404 m (Figure 4). Adding moss causes decreases in the mean annual latent and sensible heat fluxes from the PD with general decreases also in LAI and a large increase in annual total runoff (Figure A5). The high porosity of the moss layer causes less water to be available at the surface for evaporation, reducing the latent heat flux and making more water available for runoff, and its insulating effect keeps the soil surface cooler, which reduces plant growth and also the sensible heat flux. The reduction in plant growth due to cooler soils also reduces water uptake for transpiration further increasing runoff.

Comparing simulated ground temperatures to observations at the GTN-P borehole sites shows a slight increase in wMAE at all depth ranges and seasons compared to the 'SoilGrids' simulation (Figure 5). Comparing the KDE plots of the bias distribution between modelled and observed borehole temperatures for the 'SoilGrids+Moss' and the 'SoilGrids' simulations shows an increased cool bias in the shallow soil which is especially evident in summer (Figure 6). This bias extends deeper into the soil column, albeit weakening with depth. The cooling of soils due to the incorporation of a moss layer was also found by Porada et al. (2016), however their simulations included a dynamic extent for moss cover. The creation of a cold bias due to the introduction of a moss layer is reasonable considering that the moss layer was applied to all areas uniformly. While this experiment was intended to understand the impact of moss on simulated ground temperatures, future work should attempt to place moss with a more realistic distribution, similar to Porada et al. (2016).

When the meteorological forcing dataset is CRUJRA55 instead of CRUNCEP, the MAE of both 'SoilGrids+Moss' and 'Pel16+Moss' improves further to 0.415 m and 0.404 m, respectively, with two fewer cells ISPF (The spatial differences between the 'Pel16+Moss' and 'SoilGrids+Moss' simulations with CRUNCEP and CRUJRA55 are shown in Figure A6). The CRUNCEP meteorological forcing dataset generally produces deeper ALTs for much of Eurasia than simulations forced with CRUJRA55 with some shallower ALTs in Alaska and the Yukon. While CRUNCEP and CRUJRA55 share a common climatology (CRU), it is likely their differences in sub-monthly variability leads to significant differences in simulated PA and ALTs. This result is in line with Beer et al. (2018) who used artificially manipulated climate datasets to show that soil temperature can be 0.1 to 0.8 °C higher when climate variability is reduced in the model forcing data.

Comparing the model experiment outputs to the GTN-P sites in Figure 4 it is evident that increasing the number of ground layers and the soil permeable depth and incorporating a top layer of moss/organic matter improves the simulated ALTs. These changes have been suggested by other studies as mentioned above and our results are in line with them. The next experiments use the model configuration from 'SoilGrids+Moss' as a starting point. While Pel16 generally gave better average MAE values than SoilGrids for ALT compared to the GTN-P sites (Figure 4), SoilGrids appears to be better validated (c.f. Shangguan et al., 2017, Figures 9 - 11). Both datasets, however, suffer from sparse data in high latitudes (e.g., Shangguan et al., 2017, Figure 2). Additionally, while it appears that the addition of moss can introduce a summer cool bias in ground temperatures (as discussed above), given the extensive distribution of bryophytes (c.f. the simulated distribution in Figure 4b in Porada et al., 2016), we chose to include moss in our further simulations.



3.6 Testing alternate soil thermal conductivity formulations

The Exp. 'deVries thermal cond.' has an smaller average MAE of 0.287 m than 'SoilGrids+Moss' (0.472 m, Figure 4). Comparing the spatial patterns of ALT for 'deVries thermal cond.' with 'SoilGrids+Moss' shows generally deeper ALTs with a large loss of permafrost in the southern zones of the PD in eastern Russia (Figures 2 and 7). Global simulated PA drops from 17.9 to 16.2 Mkm². In winter simulations at seven sites in the South Saskatchewan River Basin (SSRB), MacDonald (2015) found the de Vries (1963) soil thermal conductivity formulation to outperform the Côté and Konrad (2005) soil thermal conductivity parameterization in CLASS-CTEM through improvements in both simulated soil moisture and snow. However, the de Vries (1963) formulation neglects the effect of ice on soil thermal conductivity (see equations A7 - A10). As the thermal conductivity of liquid water (0.57 W m⁻¹ K⁻¹ at 5 °C) is much lower than that of ice (2.24 W m⁻¹ K⁻¹ at -4 °C), it is surprising that this formulation performs as well as it did both in our simulations against the GTN-P ALT observations, and for the SSRB runs conducted by MacDonald (2015). This neglecting of the thermal conductivity difference between liquid water and ice could be the cause of a dampened soil temperature annual cycle as deeper soil layers are slower to cool in the 'deVries thermal cond.' simulations compared to 'SoilGrids+Moss' (Figure A8). We do see an increase in wMAE at the GTN-P borehole sites (Figure 5) demonstrating that this parameterization does indeed degrade model performance as would be anticipated.

An alternate soil thermal conductivity parameterization that explicitly accounts for the influence of ice has recently been published. Exp. 'Tian16 thermal cond.' tests the Tian et al. (2016) formulation, which is based on de Vries (1963) (see Section A1). The new formulation simulates a much larger PE than both 'SoilGrids+Moss' and 'deVries thermal cond.' at 21.2 Mkm² with generally shallower ALTs compared to 'SoilGrids+Moss' in most regions except for the western edge of simulated Siberian permafrost (Figure 7). The 'Tian16 thermal cond.' simulation has smaller sensible and latent heat fluxes with an increase in LAI compared to 'SoilGrids+Moss' (Figure A7). The colder soils in the 'Tian16 thermal cond.' simulations retain more moisture into the summer months as less is lost to evaporation and runoff so higher LAI can be supported. The average MAE at the GTN-P ALT sites is reduced to 0.314 m (Figure 4) with no trend in bias for ALTs with depth (Figure 3). However, at the GTN-P borehole sites there is a general increase in wMAE for primarily in summer and fall and worsening with depth (Figure 5). The borehole KDE plots show strong distinctions between the 'SoilGrids+Moss' and 'Tian16 thermal cond.' simulations with a large cold bias developing in summer that then extends into fall (Figure 6).

3.7 Changing the relationship between snow depth and snow cover

Two experiments investigated different relationships between snow depth and the grid cell snow cover in CLASS-CTEM ('Snow cover: Yang97' and 'Snow cover: Brown03'). These modifications led to increases in global PA of around 1.2 Mkm² with a slightly higher PA estimated for 'Snow cover: Yang97' (Table 2). The spatial pattern of ALT for both experiments is similar with a few more grid cells simulated by 'Snow cover: Yang97' to be permafrost at the southern edge of North American and east Siberian permafrost (Figures 2 and 7). For the GTN-P ALT sites, both snow cover experiments show an increase in average MAE from 0.472 m for 'SoilGrids+Moss' to 0.579 m and 0.622 m for 'Snow cover: Yang97' and 'Snow cover: Brown03', respectively. The two parameterization changes result in a slight increase in spring albedo (< 5%)

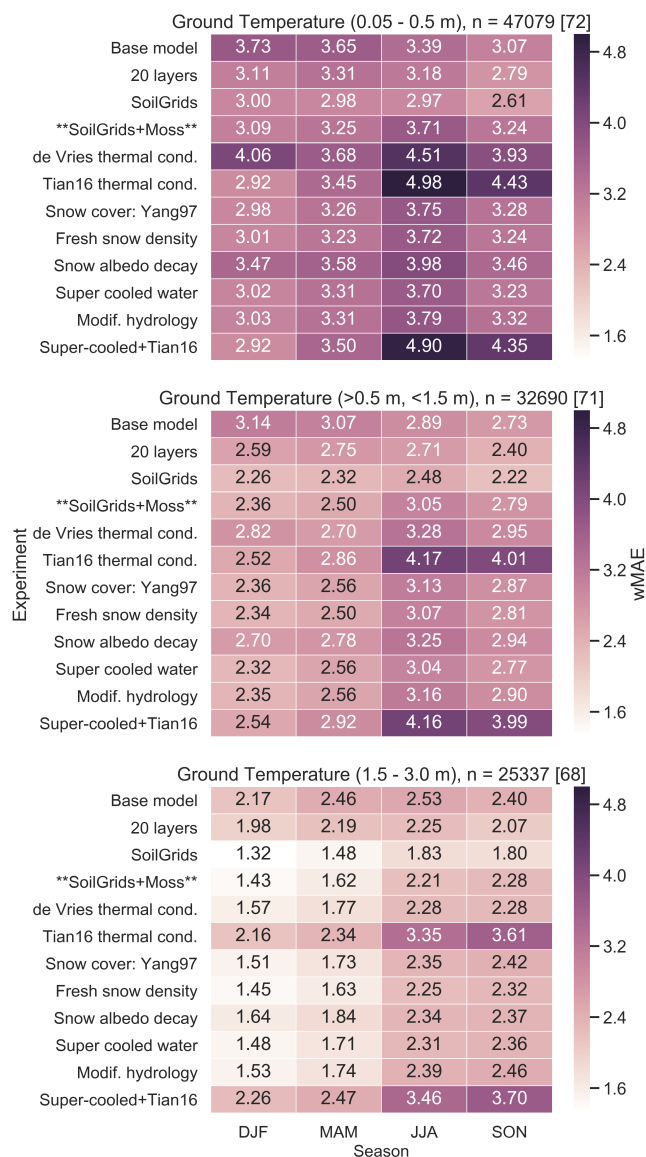


Figure 5. Weighted mean absolute error (wMAE, °C) between the simulated ground temperatures and those of the GTN-P borehole temperature sites (Table A3) for three depths: 0.05 - 0.5 m, 0.5 m - 1.5 m, and 1.5 - 3.0 m. The weighted mean absolute error (wMAE) is produced by calculating the wMAE for each depth range and season at each site within a grid cell and taking the average across all grid cells (see Section 2.3). The number of observations differs between depths and is listed along with the number of CLASS-CTEM grid cells with GTN-P borehole sites in square brackets. The colour of the text annotations is purely for clarity. The wMAE of CRUNCEP surface air temperatures compared to air temperatures measured at the GTN-P sites is 2.17 °C, 2.46 °C, 2.53 °C, and 2.40 °C for DJF, MAM, JJA, and SON, respectively over 25 337 monthly observations

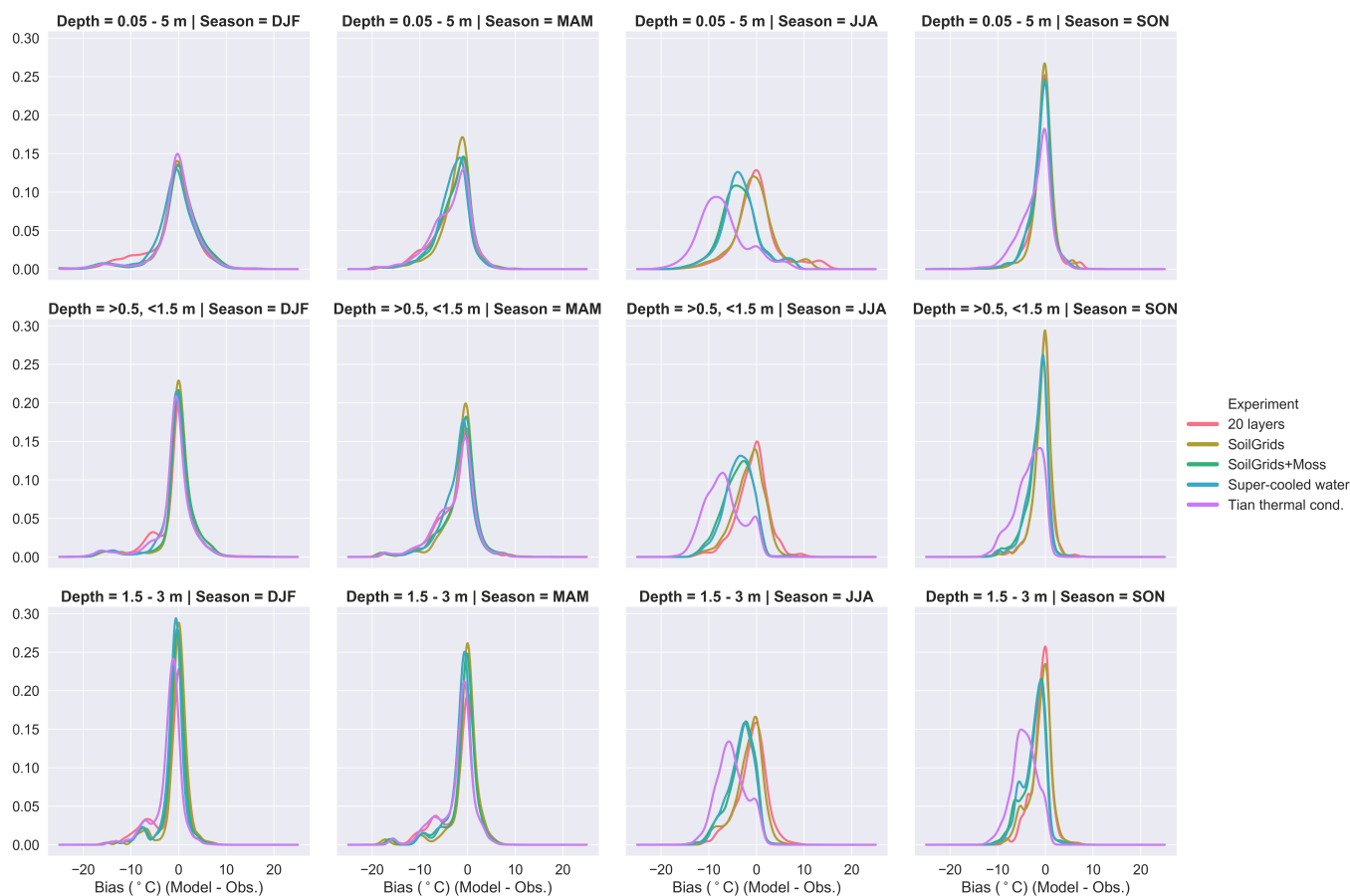


Figure 6. Gaussian kernel density estimates for the difference between the simulated ground temperatures and those of the GTN-P borehole temperature sites (Table A3) for three depths: 0.05 - 0.5 m, 0.5 m - 1.5 m, and 1.5 - 3.0 m, for each season and for selected experiments. The bandwidth was chosen using Scott's rule of thumb (Scott, 1992).

and a small decrease in winter SWE, both not statistically significant, while annual sensible heat fluxes decrease compared to 'SoilGrids+Moss' (Figure A9). The 'Snow cover: Brown03' experiment shows similar spring albedo, and latent and sensible heat fluxes changes to 'Snow cover: Yang97' but also has a general reduction in winter SWE and a reduction in runoff for the south central Siberian region compared to 'Snow cover: Yang97' (not shown). Comparing the simulated SWE from both

5 'Snow cover: Yang97' and 'Snow cover: Brown03' to Blended-5 (see Section 2.3; Mudryk et al., 2015; Kushner et al., 2018) shows a slight improvement in model performance compared to both 'Base model' and 'SoilGrids+Moss' throughout the snow year, which tends to be more pronounced during fall and winter (Fig. A10) although there is little difference between the two snow cover experiments.

Changes in snow cover can lead to large changes in albedo due to the significant brightness difference between snow and

10 vegetation/bare ground. To investigate the impact of these experiments on albedo we evaluated seasonal averages of simulated

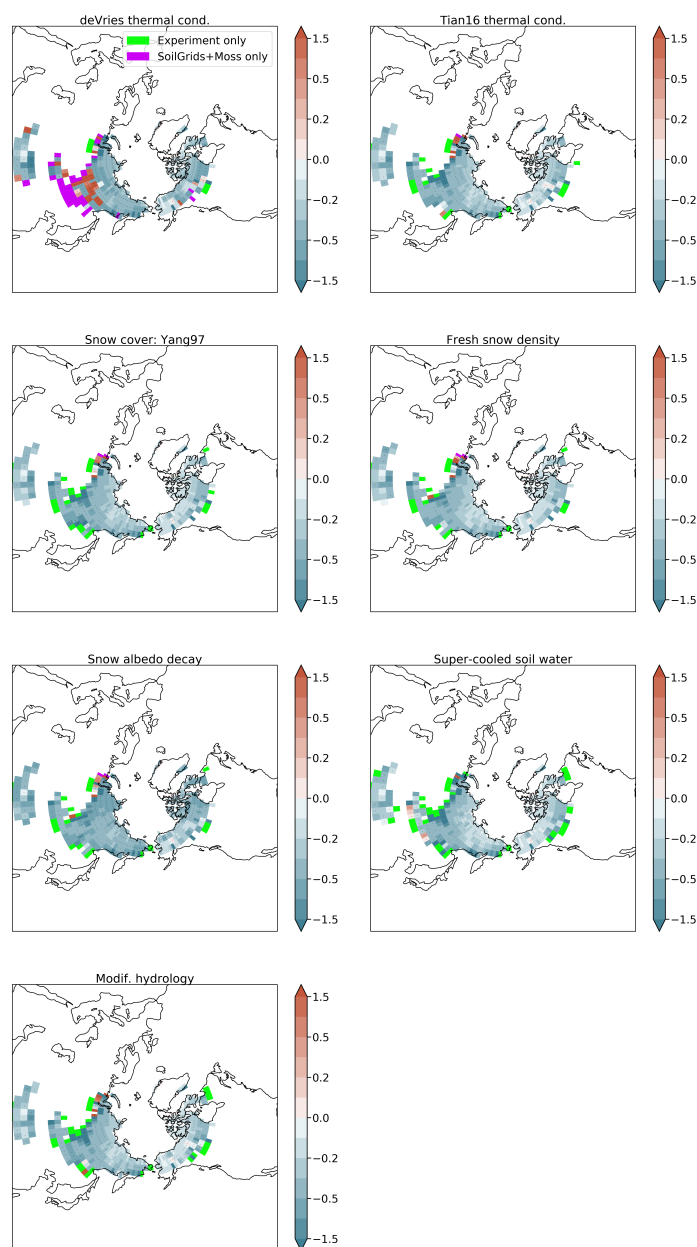


Figure 7. ALT differences (meters) for experiments that are based on the model setup of 'SoilGrids+Moss' (see Table 1) compared to the 'SoilGrids+Moss' simulation. Negative values indicate that ALTs of the experiment are deeper than in 'SoilGrids+Moss' while positive values indicate shallower ALTs. Since permafrost free soils have an undefined ALT, model grid cells that have permafrost in only the experiment are green while cells that have permafrost only in the 'SoilGrids+Moss' simulation are purple. Dots indicate grid cells that are statistically significant (independent two-sample t-test p level < 0.05).



albedo against MODIS observations over latitudes northward of 45°N for the period 2000 to 2013 (Figure A11). We find the spring (AMJ) albedo from the various simulations is about the same (Fig. A11), with anomaly correlation coefficient (ACC) of about 0.5 and standard deviation and root mean square error of approximately 130% and 120%, respectively, relative to the standard deviation from observations.

5 3.8 Considering wind speed in the calculation of fresh snow density

In CLASS-CTEM, the density of freshly fallen snow depends on the ambient air temperature (Eqn. A19). Exp. 'Fresh snow density' tested a parameterization from the CROCUS model that also includes wind speed in this calculation (Eqn. A20). This experiment shows an increase in PA from 17.9 ('SoilGrids+Moss') to 18.9 Mkm² and while ALTs are generally comparable, there are more grid cells with permafrost at the southern edges of the PD similar to the experiments described above (Figures 2 and 7). Compared to the GTN-P ALT sites, the 'Fresh snow density' results are similar to those of the snow cover experiments with no improvement in average MAE (0.581 m; Figure 4). Compared to 'SoilGrids+Moss', the experiment 'Fresh snow density' has lower (0 - 10%) mean annual latent heat flux and generally slightly higher sensible heat flux, spring albedo, and winter SWE (Figure A12) although all are not statistically significant. There is a no discernible impact upon modelled DJF SWE compared to Blended-5 or upon spring (AMJ) albedo compared to MODIS (Figure A10 and A11).

The typical wind speed in the CRUNCEP meteorological forcing dataset when snow is falling is in the range of 1 - 5 m s⁻¹ (Figure 8). With Eqn A20, the density of freshly fallen snow tends to be lower at very low wind speeds then higher as wind speed increases for the same air temperature. The generally higher density of fresh snow with the CROCUS parameterization results in a snow pack with higher thermal conductivity (Sturm et al., 1997) and thus cooler soils as evident from the expansion in PA for the 'Fresh snow density' experiment (Figure 2). Both the original CLASS-CTEM parameterization and that of the CROCUS model produce fresh snow densities within the range of observations. Roebber et al. (2003) evaluated 1650 snowfall events from 28 continental US sites and found the density of freshly-fallen snow to vary from 21.4 to 526.3 kg m⁻³ with a median value of 70.9 kg m⁻³. It should be noted that these data only represent snowfall events where the wind speed was less than or equal to 9 m s⁻¹.

3.9 Adopting an efficient spectral method for snow albedo decay

Changing the snow albedo decay parameterization from an exponential form (Verseghy, 2017) to an efficient spectral parameterization (Dickinson, 1983)(Exp 'Snow albedo decay') results in a small improvement in average MAE for the GTN-P ALT sites (Figure 4). There is a drop in PA (15.6 Mkm²) compared to 'SoilGrids+Moss' (17.9 Mkm²), reflecting a near uniform deepening of ALT with the exception of small areas on the western edge of the Siberian PD (Figures 2 and 7; Table 2). The 'Snow albedo decay' experiment has higher mean annual latent and sensible heat fluxes for much of the PD with the exception of the Canadian Arctic Archipelago, the North Slope of Alaska, and the northern Urals in Russia (Figure A13). There is also reduced annual runoff with higher LAI through much of the high latitudes compared to 'SoilGrids+Moss'. The efficient spectral method for albedo decay generally produces lower albedos than CLASS-CTEM's original exponential parameterization. The impact upon spring albedo and SWE leads to a notable decline in model performance compared to observation-based datasets

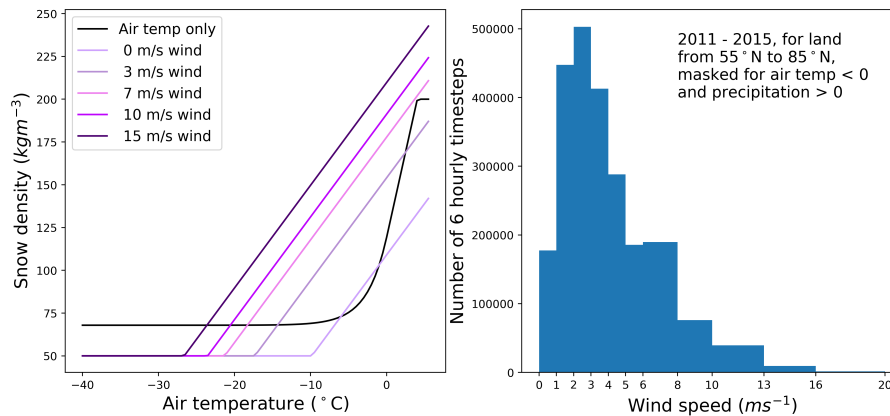


Figure 8. Left: Snow density as a function of air temperature for the original CLASS-CTEM formulation (Eqn A19) and for Exp. 'Fresh snow density' which includes consideration of wind speed (Eqn A20 -purple lines indicate different wind speeds). Right: Histogram of wind speeds for the period 2011 to 2015 for the CRUNCEP meteorological dataset.

(Figure A10 and A11). While the MODIS timeseries is limited, Exp. 'Snow albedo decay' is shown to under-perform having a relatively low ACC (<0.35), and slightly larger normalized standard deviation and root mean square error. The CRUJRA55-forced experiments, on the other hand, give slightly better spring albedo for all experiments forced with that meteorological dataset. This could be due to the sub-monthly variability difference of CRUJRA55 compared to CRUNCEP as Beer et al. (2018) found one of the largest impacts of changing climate variability in model forcing to be snow depth, which will impact upon snow melt and surface albedo. The lower albedo in the 'Snow albedo decay' experiment leads to a smaller snowpack which melts earlier resulting in reduced spring runoff, a longer growing season, and a higher LAI. The warmer land surface results in larger ALTs. At the GTN-P borehole sites, the 'Snow albedo decay' experiment shows a noticeable increase in wMAE values across all seasons and most depth bands.

10 3.10 Allowing unfrozen water in frozen soils

The inclusion of unfrozen water in frozen soils (Exp. 'Super cooled water') leads to an increased PA of 20.1 Mkm² with no significant bias with depth compared to the GTN-P ALT sites (Figure 3). The average MAE at the GTN-P ALT sites is slightly improved over 'SoilGrids+Moss' at 0.414 m (Figure 4). At the GTN-P borehole sites, there is little impact evident in the wMAE values (Figure 5). The larger PA for this experiment could be reflecting the thermal conductivity differences between completely frozen soil and frozen soil with some residual liquid water. The differences in bulk thermal conductivity would slow heat transfer into the deeper ground layers for the 'Super cooled water' simulation during periods where the soil layer temperature is below 0°C. As a result spring warming would be slower to reach deeper layers. The 'Super cooled water' experiment generally has smaller latent heat fluxes, increased runoff and decreased LAI compared to 'SoilGrids+Moss' (Figure A14). The inclusion of unfrozen water in frozen soils leads to drier soils through downward movement of the liquid water while



the soil temperature is below zero. The drier soils and the cooler soil temperatures lead to increased annual runoff and to lower latent heat fluxes and LAI.

Ganji et al. (2015) investigated streamflow for 21 watersheds in eastern Canada using CLASS and the WATROUTE routing scheme. They report their modifications (super-cooled soil water, fractional permeable area and modified hydrology due to ice; discussed in Section A6) improved streamflows particularly during the spring melt. The changes were attributed to reduced hydraulic conductivity of frozen soils causing more snow melt runoff and less infiltration. We compared our simulated seasonal runoff for seven major river basins that drain permafrost regions (Figure 9). As mentioned previously (Section 2.3), this comparison is rudimentary and limited to seasonal discharges since the CLASS-CTEM runoff is not routed. An additional caveat is that the CLASS-CTEM simulations did not include excess ground ice (e.g. slab ice such as ice wedges or lenses commonly found in regions affected by thermokarst processes), groundwater or interflow, all of which could increase runoff (baseflow) in the summer and fall seasons. As a result we limit our discussion to the spring and winter seasons. The 'Super cooled water' experiment has lower spring runoff than both 'Base model' and 'SoilGrids+Moss' but higher winter runoff, making it more in line with observed river discharges (Figure 9).

Given the 'Super cooled water' and 'Tian16 thermal cond.' simulations had the lowest average MAE at the GTN-P ALT sites (Figure 4) a simulation was run with both of these parameterizations included (Exp. 'Super-cooled+Tian16'). This experiment further reduced the average ALT MAE to 0.288 m but considerably worsened simulated ground temperatures at the GTN-P borehole sites (Figure 5). This incongruity between model performance at the ALT and borehole sites could be reflecting biases due to the spatial distribution of the sites (see Figure 1), the differing number of observations of ALT vs. borehole temperatures, or to biases in the observations themselves, which is discussed in Section 3.13.

3.11 Modifying hydrology due to ice

The 'Modif. hydrology' experiment modified soil matric potential and saturated hydraulic conductivity to account for the impact of frozen water following the work of Farouki (1981) and Koren et al. (1999). These changes to the soil hydrology led CLASS-CTEM to simulate a PA of 19.5 Mkm² (Table 2) with generally slightly deeper ALTs in much of the high latitude PD compared to 'SoilGrids+Moss' (Figures 2 and 7). This experiment has poorer average MAE for the GTN-P ALT sites (0.548 m) with a similar distribution of bias by grid cell (Figure 4) to the snow experiments above. Performance at the GTN-P borehole sites is similar to Exp. 'SoilGrids+Moss' (Figure 5). The 'Modif. hydrology' experiment annual latent heat flux generally increases slightly in the Canadian PD along with a strong increase in LAI but a decrease in annual runoff compared to 'SoilGrids+Moss' (Figure A15). Since the modifications to soil matric potential and saturated hydraulic conductivity (Equations A35 and A36) generally decrease water mobility in soils with ice present, the 'Modif. hydrology' soils are generally wetter, allowing higher annual latent heat flux and supporting higher LAI. The 'Modif. hydrology' experiment has similar runoff to the 'Base model' experiment with higher spring runoff than observed river discharges while the winter runoff is reduced compared to 'SoilGrids+Moss' and is also smaller than the observed river discharges (Figure 9). To investigate synergistic effects between the two modifications ('Modif. hydrology' and 'Super cooled water'), a simulation was run with both modifications applied (similar to Ganji et al.'s Exp. 3). This simulation gave slightly higher spring runoff but similar winter runoff compared

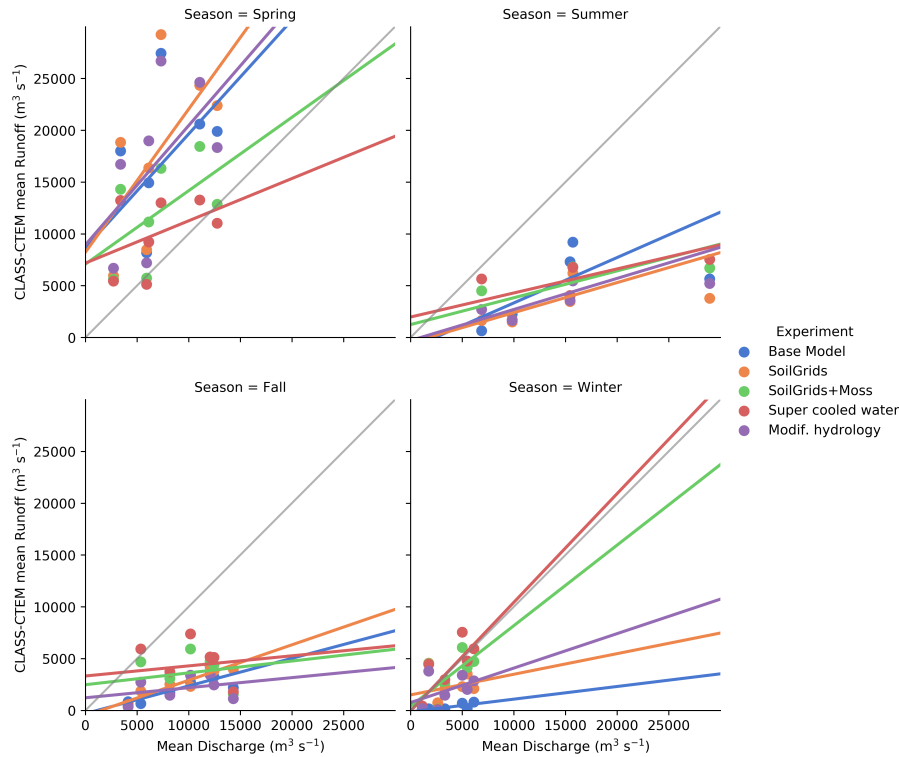


Figure 9. Mean 1965 - 1984 seasonal discharges of major rivers draining permafrost regions (Ob, Volga, Lena, Yenisei, Yukon, Mackenzie and Amur; UNESCO Press, 1993) compared to total runoff from selected model runs for the same period. Each dot represents one river basin.

to 'Modif. hydrology' (not shown). Thus it appears, with respect to runoff, the modifications to hydrology have a stronger influence than super cooled soil water, in line with the conclusion of Ganji et al. (2015) that the primary effect is to reduce hydraulic conductivity which decreases infiltration and increases snow melt runoff.

3.12 Influence of sub-grid heterogeneity

5 The CLASS-CTEM model grid used in our study is the same as that used in the CanESM. Based on the experiments in the previous section, with respect to the ALT sites of the GTN-P, the lowest average MAE we are able to achieve is about 0.4 m. With the size of our model grid cells, what is the best MAE we can reasonably expect given the sub-grid heterogeneity at the observation sites? Many of the GTN-P ALT measurements are performed on an 11 x 11 sampling grid covering 1 km² giving 121 data points at one point in time per site; the mean standard deviation of measured ALT over these sampling grids varies
 10 from 0.02 m to 0.49 m (Table A2). However, one square kilometre is still small compared to model grids ranging in size from hundreds to thousands of km². One measure of the influence of sub-grid heterogeneity can be obtained by considering the MAE per site in the grid cells where we have more than one GTN-P ALT site (Figure 10). For these grid cells, the spread in

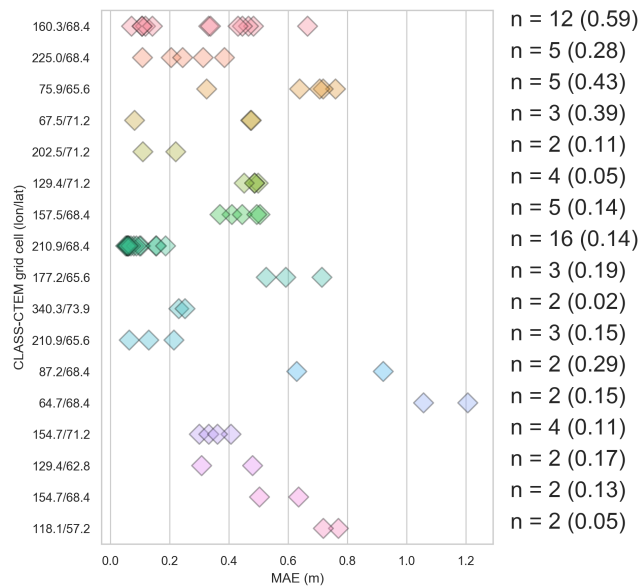


Figure 10. Mean absolute error (MAE) for CLASS-CTEM grid cells with multiple GTN-P ALT sites for the 'SoilGrids+Moss' simulation. The number of ALT sites is listed along with the range in MAE in each grid cell in parentheses.

MAE at each site ranges from 0.01 m (grid cell with 2 sites) to 0.59 m (12 sites) for the 'SoilGrids+Moss' simulation. While it is not reasonable to directly compare the sub-grid range of MAE to the model average MAE shown in Figure 4, Figure 10 demonstrates that sub-grid heterogeneity is a significant source of variability in ALT within model grid cells and that variability will impose constraints on the lower limit of MAE that is attainable by the model.

- 5 For the GTN-P borehole sites, the wMAE in temperature bias for the model varies between ca. 1.5 and 3.7 °C (Figure 5), depending on depth and season. As with ALT, what is a reasonable wMAE for ground temperatures given the size of the model grid cells and the discrete nature of a borehole? To better understand the role of sub-grid heterogeneity in borehole temperatures, we make use of the Slave Province Surficial Materials and Permafrost Study (SPSMPS; Gruber et al., 2018). The SPSMPS
- 10 collected air and ground temperature measurements for 15 m x 15 m plots with hourly borehole temperatures at thirty-five boreholes all located within a ca. 1200 km² area. The observed screen-level temperatures are generally reasonably close to those of CRUNCEP but CRUNCEP has slightly cooler summer temperatures (Figure A16). What is most striking about the borehole temperatures at Lac de Gras is the large spread in ground temperatures at all depths and in most seasons (Figure 11). The temperature range is smallest in fall and spring when the soils are thawing or freezing and largest in winter with differences
- 15 varying from 12 to over 20 °C depending on the soil depth. This remarkable spread in temperature is due to variations in slope, aspect, soil moisture, soil texture, soil organic matter content, and vegetation type and distribution. The simulated ground temperatures from two experiments are plotted alongside the boreholes ('SoilGrids' and 'SoilGrids+Moss'). As the model is driven by CRUNCEP and we have no precipitation information for the SPSMPS sites, it is difficult to determine the cause of any biases. Also, although the SPSMPS sampling area is considerably larger than the GTN-P sites, the same arguments



apply concerning the mismatch of scales between the observational area and the model grid, and the variability introduced by sub-grid heterogeneity.

An additional measure of how reasonable the model wMAE is at the borehole sites can be obtained by comparing the CRUNCEP screen-level temperature, which is used to force the model, and the observed screen-level temperature at each GTN-P site. The MAE for screen-level temperature is between 2.17 and 2.53 °C across all seasons. Therefore the model's wMAE range for shallow soil of ca. 3 to 3.7 °C varies from ca. 0.8 to 1.2 °C above that of the MAE for CRUNCEP's screen-level temperature (for the 'SoilGrids+Moss' simulation). Given the large spread in borehole temperatures in a relatively small area at the SPSMPS sites, and the MAE of the model's forcing air temperature, it appears the model's wMAE can be considered reasonable.

10 3.13 Influence of bias due to ALT or borehole sampling locations

Temperature in individual boreholes and ALT at individual sites often differ from the grid cell they are compared with because of sub-grid variability as discussed above. The underlying spatial variation of ground temperature, even at distances smaller than 1km is well documented (Smith, 1975; Morse et al., 2012; Gubler et al., 2011). If the locations of GTN-P sites were randomly sampled, sub-grid effects would be expected to cancel out and, consequentially, a mean bias (cf. Figure 4) close to zero would be indicative of good model performance. In reality, however, the choice of GTN-P measurement locations are likely biased and the nature and consequences of this bias are difficult to assess. For example, ALT sites are likely to be biased toward fine-grained and organic-rich soils and locations with small ALT where probing can be carried out. The choice of ALT and borehole sites in areas of sporadic permafrost is likely to be biased towards cold areas in the landscape. This is because ALT requires permafrost and because permafrost researchers are unlikely to drill, instrument and operate boreholes in seasonally frozen ground. Finer-scale local studies have noted that observations are strongly biased towards permafrost existence (Boeckli et al., 2012). The melt of excess ice from the top of permafrost presents an additional source of bias that may result in ALT data showing values of seasonal thaw depth that underestimate the amount of ground ice that was melted. This is because ALT obtained from frost-table probing without recording surface subsidence (Shiklomanov et al., 2013) omits an important part of the changes in the natural environment. In summary, it is likely that a slightly positive model bias, i.e. higher temperatures and greater ALT simulated than observed, would correspond to a model that best represents reality. Quantifying that effect however is beyond the present study.

4 Conclusions

The performance of CLASS-CTEM in cold regions has been investigated in the past by numerous researchers (Tilley et al., 1997; Bellisario et al., 2000; Letts et al., 2000; Lafleur et al., 2000; Paquin and Sushama, 2014; MacDonald, 2015; Ganji et al., 2015). As a result, several modifications have been suggested to improve the model's performance in these regions. Drawing from these recommendations and other studies, 18 experiments were carried out to investigate the influence of: 1) the number of ground layers, 2) soil permeable depth datasets, 3) the addition of a moss layer, 4) changing the soil thermal conductivity

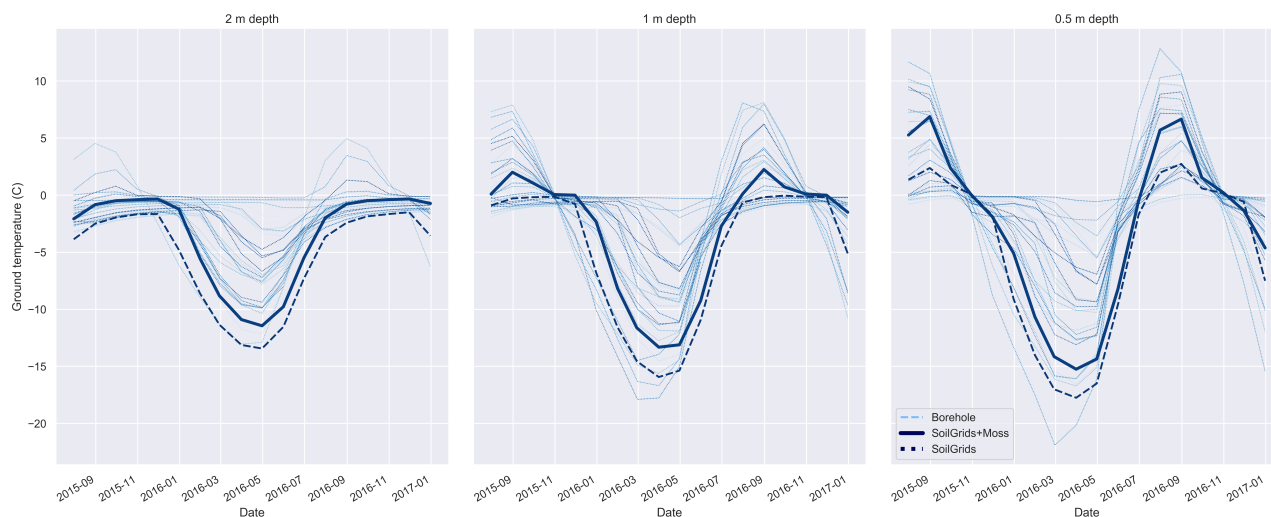


Figure 11. Borehole temperatures for 0.5, 1, and 2 m depths from the Slave Province surficial materials and permafrost study (SPSMPS, Lac de Gras region, NWT, Canada; (Gruber et al., 2018)) along with CLASS-CTEM simulated ground temperatures for Exp. 'SoilGrids' and 'SoilGrids+Moss'. The thirty-five boreholes are each represented by a single line and are all located within a ca. 1200 km² area. The model output is from the grid cell corresponding to the SPSMPS study area.

formulation, 5) altering the derivation of snow cover based on snow depth, 6) adding the effect of wind speed to the calculation of fresh snow density, 7) changing the model's snow albedo decay calculation to an efficient spectral parameterization, and 8) modifications to frozen soil hydrology including allowing unfrozen water in frozen soils and an alteration to hydraulic conductivity and soil matric potential for the presence of ice. Two soil permeable depth datasets were tested (Pelletier et al. (2016) and SoilGrids; Shangguan et al. (2017)) along with two meteorological datasets (CRUNCEP v.8; Viovy (2016) and CRUJRA55 v.1.0.5; Kobayashi et al. (2015); Harris et al. (2014)). The simulated active layer thicknesses (ALTs) were compared to 1570 observations from 97 sites from the Global Terrestrial Network for Permafrost (GTN-P; Table A2, Figure 1), the simulated soil temperatures to 105 106 monthly observations at 132 GTN-P borehole temperature sites (Table A3), 35 borehole sites from the Slave Province Surficial Materials and Permafrost Study (SPSMPS; Gruber et al., 2018), surface albedo to a remotely-sensed dataset (MODIS MCD43C3), snow water equivalent (SWE) to a blend of five observation-based datasets (Blended5; Mudryk et al., 2015), and seasonal runoff to river discharges for major rivers draining the Arctic (UNESCO Press, 1993) as well as literature estimates of permafrost area (Table 2).

The original model version had an overly small simulated permafrost area of 8.6 Mkm² which was almost doubled to 16.7 Mkm² by increasing the number and depth of ground layers. Of the two soil permeable depth datasets, Pelletier et al. (2016) gave consistently lower average mean absolute errors (MAE) at the GTN-P ALT sites compared to SoilGrids. However, SoilsGrids was chosen for further simulations as this dataset appears to be better validated (Shangguan et al., 2017). For the two meteorological datasets used, the permafrost specific results depended on the model configuration and parameterizations tested. More consistently, spring albedo appeared to be better simulated using CRUJRA55 while winter SWE was slightly



better with CRUNCEP. Changes to the model configuration by increasing soil permeable depths using the SoilGrids dataset, and adding a layer of moss reduced the average MAE at the GTN-P ALT sites from over 2.5 m (Exp. '20 ground layers') to 0.472 m (Exp. 'SoilGrids+Moss'). While most alternate parameterizations either degraded model performance at the GTN-P ALT and borehole sites, or degraded the performance of another model output such as albedo or SWE, incorporating unfrozen water in frozen soils following Niu and Yang (2006) is being considered for inclusion in future versions of CLASS-CTEM. A simulation with the Niu and Yang (2006) parameterization resulted in an average MAE of 0.414 m at the GTN-P ALT sites, relatively small impacts on wMAE at the GTN-P borehole sites, and a possible improvement in seasonal runoff. Further assessment of the improvements in runoff using a river routing scheme are needed before this parameterization will be fully adopted. Based on the tests performed here, the optimal model configuration will include more ground layers to a greater depth, soil permeable depths from the SoilGrids dataset, and moss in locations where it is appropriate. These changes give a simulated permafrost area of between 15.7 to 17.9 Mkm² (Table 2) which reasonably close to the expected 15 Mkm² for the 'region_50' based on published estimates derived from mean annual air temperature (see discussion in Section 2.3.4).

There are six main limitations of our study. First, thermokarst processes due to melt of excess ground ice (ice wedges or lenses) are not simulated. As maps of ground ice extent improve (e.g. O'Neill et al., 2018) and become more suitable for use as a model geophysical field, parameterizations such as Lee et al. (2014) could be incorporated. Second, our treatment of mosses and their impact is simplistic. A more comprehensive approach such as the LiBry model (Porada et al., 2016) would allow for dynamic moss extents and more bryophyte subtypes including lichens. Third, the plant functional types used here are not specific to the Arctic and do not include shrubs. Shrubs, in particular, are presently expanding and have complex impacts upon Arctic regions (e.g. Figure 3 in Myers-Smith et al., 2011). Fourth, orographic influences on permafrost such as slope and aspect were not resolved. Fifth, inland water bodies and their impact upon ground thermal regimes were not considered. Finally, the influence of sub-grid heterogeneity was ignored as permafrost in the model grids is binary thus excluding the simulation of taliks. With regard to the influence of sub-grid heterogeneity, the standard deviation of ALT on the 1 km² measurement grids at the GTN-P ALT sites, the spread in MAE in grid cells with multiple GTN-P ALT sites, and the SPSMPS collection of 35 boreholes over a 1200 km² study area indicate that it is likely difficult to reduce the wMAE of ALT or borehole temperature much further, given the size of the model grid cells (ca. 2.8°). Based on the model physics performance presented here, it appears that with the modifications described above, the land surface scheme in CLASS-CTEM is well-suited to provide the physical conditions for simulating carbon fluxes in the permafrost domain.

Code and data availability. CLASS-CTEM model code for the 'Base model' version is available from <https://gitlab.com/jormelton/classctem>. For other experiments, from that same repository, clone the 'develop' branch. Within the develop branch the following tags correspond to experiments in this manuscript (see Table 1) with the most strongly impacted subroutines in parentheses: 1) deVries thermal cond.: 'archive/soilthermalcond' (TPREP), 2) Tian16 thermal cond.: 'archive/Tian16SoilThermalCond (TPREP), 3) Snow cover: Yang97/Brown03: 'archive/snowcov_changes' (CLASSA), 4) Fresh snow density: 'archive/snowdens' (CLASSI), 5) Snow albedo decay: 'archive/snowalbedofresh'



(CLASSA,SNOALBA), 6) Super-cooled water: 'archive/supercooledH2O' (CLASSB,TMCALC,TWCALC), and 6) Modif. hydrology: 'archive/arman' (GRDRAN,GRDINFL).

Appendix A: Description of alternate parameterizations

A1 Soil thermal conductivity

- 5 CLASS-CTEM calculates the thermal conductivities of organic and mineral soils following Côté and Konrad (2005). The soil thermal conductivity, λ ($\text{W m}^{-1} \text{K}^{-1}$), is modelled via a relative thermal conductivity, λ_r , which varies between a value of 1 at saturation and 0 for dry soils:

$$\lambda = [\lambda_{sat} - \lambda_{dry}] \lambda_r + \lambda_{dry} \quad (\text{A1})$$

- Using the following generalized relationship, the relative thermal conductivity is obtained from the degree of saturation (the water content divided by the pore volume), S_r (unitless):

$$\lambda_r = \frac{\kappa S_r}{[1 + (\kappa - 1) S_r]} \quad (\text{A2})$$

Based on the soil characteristics and state, the empirical coefficient, κ ($\text{W m}^{-1} \text{K}^{-1}$), takes the following values:

1. Unfrozen coarse mineral soils: $\kappa = 4.0$
2. Frozen coarse mineral soils: $\kappa = 1.2$
- 15 3. Unfrozen fine mineral soils: $\kappa = 1.9$
4. Frozen fine mineral soils: $\kappa = 0.85$
5. Unfrozen organic soils: $\kappa = 0.6$
6. Frozen organic soils: $\kappa = 0.25$

- The dry thermal conductivity, λ_{dry} , is calculated via an empirical relationship using the pore volume, θ_p ($\text{m}^3 \text{m}^{-3}$), with different coefficients for organic and mineral soils:

$$\lambda_{dry,mineral} = 0.75e^{(-2.76\theta_p)} \quad (\text{A3})$$

$$\lambda_{dry,organic} = 0.30e^{(-2.0\theta_p)} \quad (\text{A4})$$



While the saturated thermal conductivity, λ_{sat} , is calculated by Côté and Konrad (2005) as a geometric mean of the conductivities of the soil components, other studies (e.g. Zhang et al., 2008) have found the linear averaging used by de Vries (1963) to be generally more accurate and this approach has been adopted by CLASS-CTEM,

$$\lambda_{sat,unfrozen} = \lambda_{liq}\theta_p + \lambda_s(1 - \theta_p) \quad (A5)$$

$$5 \quad \lambda_{sat,frozen} = \lambda_{ice}\theta_p + \lambda_s(1 - \theta_p) \quad (A6)$$

where λ_{ice} is the thermal conductivity of ice, λ_{liq} is that of liquid water and λ_s is that of the soil solid particles.

Exp. 'deVries thermal cond.' replaces the CLASS-CTEM default soil thermal conductivity parameterization with that of de Vries (1963):

$$\lambda = \frac{\lambda_{liq}\theta_{liq} + f_a\lambda_a\theta_a + f_s\lambda_s\theta_s}{\theta_{liq} + f_a\theta_a + f_s\theta_s} \quad (A7)$$

10 where the a subscript denotes the air component, θ is the volumetric fraction, and f is the 'weighting' factor (unitless) which is given by:

$$f_s = \frac{1}{3} \left[\frac{2}{1 + 0.125\left(\frac{\lambda_s}{\lambda_{liq}} - 1\right)} + \frac{1}{1 + 0.75\left(\frac{\lambda_s}{\lambda_{liq}} - 1\right)} \right] \quad (A8)$$

$$f_a = \frac{1}{3} \left[\frac{2}{1 + g_a\left(\frac{\lambda_a}{\lambda_{liq}} - 1\right)} + \frac{1}{1 + (1 - 2g_a)\left(\frac{\lambda_a}{\lambda_{liq}} - 1\right)} \right] \quad (A9)$$

where g_a represents a unit-less empirical air pore-shape factor,

$$15 \quad g_a = \begin{cases} 0.333 - (0.333 - 0.035)\frac{\theta_a}{\theta_p}, & \theta_{liq} > 0.09 \\ 0.013 + 0.944\theta_{liq}, & \theta_{liq} \leq 0.09 \end{cases} \quad (A10)$$

An alternate approach is tested in Exp. 'Tian16 thermal cond.'. The Tian et al. (2016) thermal conductivity parameterization is based upon the de Vries (1963) formulation, but simplifies and extends it to both frozen and unfrozen soils. In their formulation, Tian et al. adapt equation A7 to include ice and organic matter as,

$$\lambda = \frac{\lambda_{liq}\theta_{liq} + f_{ice}\lambda_{ice}\theta_{ice} + f_a\lambda_a\theta_a + f_s\lambda_s\theta_s + f_{organic}\lambda_{organic}\theta_{organic}}{\theta_{liq} + f_{ice}\theta_{ice} + f_a\theta_a + f_s\theta_s + f_{organic}\theta_{organic}} \quad (A11)$$



for wet soil whereas the thermal conductivity of completely dry soils is calculated by,

$$\lambda = 1.25 \frac{f_a \lambda_a \theta_a + f_s \lambda_s \theta_s + f_{organic} \lambda_{organic} \theta_{organic}}{f_a \theta_a + f_s \theta_s + f_{organic} \theta_{organic}} \quad (\text{A12})$$

The Tian et al. formulation also modifies the pore-shape factor (equation A10) to be,

$$g_a = 0.333 - \left(1 - \frac{\theta_a}{\theta_p}\right) \quad (\text{A13})$$

5 for air and

$$g_{ice} = 0.333 - \left(1 - \frac{\theta_{ice}}{\theta_p}\right) \quad (\text{A14})$$

for ice. Tian et al. (2016) introduce a shape factor for ellipsoidal soil particles, g_m as,

$$g_m = g_{sand} \theta_{sand} + g_{silt} \theta_{silt} + g_{clay} \theta_{clay} \quad (\text{A15})$$

where g_{sand} is 0.182, g_{silt} is 0.00775, and g_{clay} is 0.0534. The shape factor for organic soils, $g_{organic}$, is set to 0.5. The
 10 same 'weighting' factor is used for ice, air, organic and mineral soil components and left unchanged from equation A9.

A2 Snow cover fraction

CLASS-CTEM relates snow depth, (d_{snow} ; m), to snow cover, (f_{snow} ; fraction), via a linear function (Figure A2) (Verseghy, 2017),

$$f_{snow} = \min \left[1, \left(\frac{d_{snow}}{d_0} \right) \right] \quad (\text{A16})$$

15 where d_0 is a limiting snow depth assigned a value of 0.1 m. Exp. 'Snow cover:Yang97' changes the CLASS-CTEM linear function to a hyperbolic tangent function (Yang et al., 1997),

$$f_{snow} = \tanh \left(\frac{d_{snow}}{d_0} \right) \quad (\text{A17})$$

Another alternative parameterization for snow cover from snow depth was proposed by Brown et al. (2003), which was not evaluated in MacDonald (2015). This relation was developed based on analysis of a global gridded snow water equivalent
 20 product designed to evaluate GCMs. Exp 'Snow cover:Brown03' tests the impact of that parameterization by changing the snow cover function to the proposed exponential form (Brown et al., 2003),

$$f_{snow} = 1 - 0.01(15 - 100d_{snow})^{1.7}. \quad (\text{A18})$$



A3 Fresh snow density

The density of freshly fallen snow is related to its ice-crystal structure and the volume of the ice crystal that is occupied by air. Generally, snow density is the result of 1) processes occurring in the cloud that affect the size and shape of the growing ice crystals, 2) processes that modify the crystal as it falls, and 3) compaction on the ground due to prevailing weather conditions and metamorphism in the snowpack (Roebber et al., 2003).

Fresh snow density (ρ ; kg m^{-3}) in CLASS-CTEM is calculated based on air temperature (T_a ; K). For air temperatures below freezing, (T_f), a relation from Hedstrom and Pomeroy (1998) is used, while for temperatures at or above freezing CLASS-CTEM uses an equation from Pomeroy and Gray (1995),

$$\rho = \begin{cases} 67.92 + 51.25e^{\left[\frac{(T_a - T_f)}{2.59}\right]} & T_a < T_f \\ 119.17 + 20(T_a - T_f) & T_a \geq T_f \end{cases} \quad (\text{A19})$$

In Exp. 'Fresh snow density', the effect of wind speed (u , m s^{-1}) is included following the approach used in the CROCUS model as detailed in Essery et al. (1999) with a minimum density of 50 kg m^{-3} following MacDonald (2015):

$$\rho = \max[50, 109 + 6(T_a - T_f) + 26u^{1/2}] \quad (\text{A20})$$

Wind speed may be considered important in determining fresh snow density as wind speeds greater than approximately 9 m s^{-1} can move ice crystals on the surface leading to crystal fractionation during saltation and surface compaction increasing the snow density (e.g., Gray and Male, 1981, p. 345–350).

A4 Snow albedo decay

Snow albedo (α_s ; unitless) decreases as snow ages due to snow grain growth and deposition of soot and dirt (Wiscombe and Warren, 1980). In CLASS-CTEM this process is treated via empirical exponential decay functions (Verseghy, 2017). Freshly fallen snow is given a total albedo ($\alpha_{fs,total}$) value of 0.84, a visible ($\alpha_{fs,visible}$) value of 0.95 and a near-infrared (NIR; $\alpha_{fs,nir}$) value of 0.73. It is assumed that the same decay function, calculated each timestep (Δt ; 1800 s) applies to all three albedo ranges,

$$\alpha_{s,total}(t + \Delta t) = \alpha_{s,total,old} + [\alpha_{s,total}(t) - \alpha_{s,total,old}]e^{\left(-\frac{0.01\Delta t}{3600}\right)} \quad (\text{A21})$$

If the snowpack temperature is greater than $-0.01 \text{ }^\circ\text{C}$ or the melt rate at the top of the snowpack is not negligible, $\alpha_{s,total,old}$ is set to a value characteristic of melting snow (0.50) otherwise it is set a value representing old, dry snow (0.70). The total albedo at a given time step is converted to those of the visible and NIR ranges for dry snow via,

$$\alpha_{s,visible} = 0.7857\alpha_{s,total} + 0.29 \quad (\text{A22})$$



$$\alpha_{s,nir} = 1.2142\alpha_{s,total} - 0.29 \quad (\text{A23})$$

and for melting snow,

$$\alpha_{s,visible} = 0.9706\alpha_{s,total} + 0.1347 \quad (\text{A24})$$

$$\alpha_{s,nir} = 1.0294\alpha_{s,total} - 0.1347 \quad (\text{A25})$$

- 5 Exp. 'Snow albedo decay' replaces the CLASS-CTEM exponential decay function with a spectral method based on Wiscombe and Warren (1980) and adapted for efficiency by Dickinson (1983). This efficient spectral method first calculates the diffuse radiation albedo based on the albedo of fresh snow and the transformed snow age factor (F_{age})

$$\alpha_{dif,visible} = (1 - 0.2F_{age})\alpha_{fs,visible} \quad (\text{A26})$$

$$\alpha_{dif,nir} = (1 - 0.5F_{age})\alpha_{fs,nir} \quad (\text{A27})$$

$$10 \quad F_{age} = \frac{\tau_s}{1 + \tau_s} \quad (\text{A28})$$

where τ_s is a non-dimensional snow age at each timestep found via

$$\tau_s(t + \Delta t) = \left[\tau_s(t) + \frac{(r_1 + r_2 + r_3)\Delta t}{\tau_0} \right] \left(1 - \frac{S_f \Delta t}{\Delta P} \right) \quad (\text{A29})$$

where r_1 represents the effects of grain growth due to vapor diffusion as

$$r_1 = e^{\left[5000 \left(\frac{1}{T_f} - \frac{1}{T_{g,1}} \right) \right]} \quad (\text{A30})$$

- 15 and $r_2 = r_1^{10}$, representing the additional effects at or near the freezing of meltwater on grain growth. r_3 represents the effects of soot and dirt and is set to 0.3. $T_{g,1}$ is the temperature of the top soil layer (K), τ_0 is 10^6 s, S_f is the snowfall rate for that timestep ($\text{kg m}^{-2} \text{s}^{-1}$), and ΔP is the snow fall amount threshold (10 kg m^{-2}). If, within a timestep, the fresh snowfall amount exceeds ΔP , the snow age is set to that of new snow ($\tau_s = F_{age} = 0$).



The direct radiation albedos are found by

$$\alpha_{dir,visible} = \alpha_{dif,visible} + 0.4f(\mu)(1 - \alpha_{dif,visible}) \quad (\text{A31})$$

$$\alpha_{dir,nir} = \alpha_{dif,nir} + 0.4f(\mu)(1 - \alpha_{dif,nir}) \quad (\text{A32})$$

where $f(\mu)$ is a factor that scales between 0 and 1 to give increased snow albedo due to solar zenith angles exceeding 60 °,
 5 calculated as

$$f(\mu) = \max \left[0, \frac{1 - 2\cos Z}{1 + b_\mu} \right] \quad (\text{A33})$$

where Z is the solar zenith angle and b_μ is an adjustable parameter set to 2 following the BATS model (Yang et al., 1997).

A5 Super-cooled soil water

In experiment 'Super-cooled water', unfrozen soil water in frozen soils is introduced into CLASS-CTEM following Niu and
 10 Yang (2006). Unfrozen water can exist in frozen soils through the capillary and absorptive forces exerted by soil particles on
 water in close proximity. The upper limit on the residual amount of water that can remain liquid under given soil temperature
 and texture conditions is parameterized by Niu and Yang (2006) as,

$$\theta_{liq,max} = \theta_p \left(\frac{-L_f(T_{soil,i} - T_f)}{g\psi_{sat}T_{soil,i}} \right)^{-1/b} \quad (\text{A34})$$

where g is gravitational acceleration (m s^{-2}), L_f is the latent heat of fusion (J kg^{-1}), and $T_{soil,i}$ is the soil layer temperature
 15 (K). According to Romanovsky and Osterkamp (2000) unfrozen water content in moss is negligible so $\theta_{liq,max}$ is set to zero
 for moss layers.

A6 Modified hydrology

In Ganji et al. (2015) several changes were implemented in CLASS to address how the model deals with frozen soil water.
 First, super-cooled soil water was added following Niu and Yang (2006) as described above. Secondly, fractional impermeable
 20 area was introduced, also following Niu and Yang (2006), but this has little impact upon our model simulations (discussed in
 Appendix B). Their final modification was to account for the impact of frozen water on the soil matric potential (ψ ; m) after
 Farouki (1981) and Koren et al. (1999) by adding a new term $[(1 + C_k\theta_{ice})^2]$ to the existing CLASS functional relationship,

$$\psi = \psi_{sat} \left(\frac{\theta_{liq}}{\theta_p} \right)^{-b} (1 + C_k\theta_{ice})^2 \quad (\text{A35})$$



where C_k is a constant, set to 8, that accounts for the effect of an increase in specific surface area of soil minerals and liquid water as water freezes and ice forms (Kulik, 1978). ψ_{sat} is the soil matric potential at saturation (m) and b is the Clapp and Hornberger empirical 'b' parameter (unitless) (Clapp and Hornberger, 1978). The calculation of hydraulic conductivity $k; m s^{-1}$ is also modified by multiplication with a similar term $[(1 + C_k \theta_{ice})^{-4}]$,

$$5 \quad k = k_{sat} \left(\frac{\theta_{liq}}{\theta_p} \right)^{2b+3} (1 + C_k \theta_{ice})^{-4} \quad (A36)$$

where k_{sat} is saturated hydraulic conductivity. The effect of these changes is to generally increase soil matric potential and decrease hydraulic conductivity when ice is present in the soil. These modifications are tested in Exp. 'Modif. hydrology'.

Appendix B: Fractional permeable areas in frozen soils

CLASS-CTEM accounts for the impact of frozen soil water through an empirical correction factor (f_{ice} ; unitless), according
 10 to Zhao and Gray (1997).

$$f_{ice} = \left[1 - \min \left(1, \frac{\theta_{ice}}{\theta_p} \right) \right]^2 \quad (B1)$$

This factor is used to correct the calculated soil hydraulic conductivity, k ($m s^{-1}$) which is found via the Clapp and Hornberger (1978) equation:

$$15 \quad k = f_{ice} k_{sat} \left(\frac{\theta_{liq}}{\theta_p} \right)^{2b+3} \quad (B2)$$

where k_{sat} is the hydraulic conductivity at saturation and b is an empirical parameter. Soil moisture is related to soil matric potential (ψ ; m) in CLASS-CTEM following Clapp and Hornberger (1978),

$$\psi = \psi_{sat} \left(\frac{\theta_{liq}}{\theta_p} \right)^{-b} \quad (B3)$$

where ψ_{sat} is the saturated soil matric potential (m).

Niu and Yang (2006) parameterize fractional permeable areas in frozen soils. Following their formulation, within a grid cell
 20 the permeable ($perm$) and impermeable (imp) patches affect the flux of water (q ; $m s^{-1}$) as

$$q = F_{imp} q_{imp} + (1 - F_{imp}) q_{perm} \quad (B4)$$

where the impermeable grid cell fraction, F_{imp} can be estimated as



$$F_{imp} = e^{-\alpha \left(1 - \frac{\theta_{ice}}{\theta_p}\right)} - e^{-\alpha} \quad (\text{B5})$$

and α is set to 3 following Niu and Yang (2006). Assuming q_{imp} is set to zero, Niu and Yang parameterize the influence of the permeable areas on hydraulic conductivity can be parameterized as

$$k = (1 - F_{imp})k_{sat} \left(\frac{\theta_{liq} + \theta_{ice}}{\theta_p}\right)^{2b+3} \quad (\text{B6})$$

5 while the soil matric potential is calculated as,

$$\psi = \psi_{sat} \left(\frac{\theta_{liq} + \theta_{ice}}{\theta_p}\right)^{-b} \quad (\text{B7})$$

This formulation results in a soil matric potential that is insensitive to ice content within the soil (Figure A17) which seems unreasonable (see for example Wen et al., 2012). This fact is indeed noted by Ganji et al. (2015) who state that the soil matric potential as defined by Niu and Yang (2006) is not appropriate for the case of frozen soil. The inclusion of θ_{ice} in the numerator could be a typographical error. If it is removed the hydraulic conductivity and soil matric potential behave quite similarly to the original CLASS relations which make use of the factor f_{ice} in place of $1 - F_{imp}$ (Figure A18). Testing shows the model is relatively insensitive to the small changes visible in the plots (not shown).

10



Table A1. Ground layer depths and thicknesses for the 20 ground layer configuration.

Layer number	Thickness (m)	Depth (m)
1	0.1	0.1
2	0.1	0.2
3	0.1	0.3
4	0.1	0.4
5	0.1	0.5
6	0.1	0.6
7	0.1	0.7
8	0.1	0.8
9	0.1	0.9
10	0.1	1.0
11	0.2	1.2
12	0.3	1.5
13	0.4	1.9
14	0.5	2.4
15	1.0	3.4
16	3.0	6.4
17	5.0	11.4
18	15.0	26.4
19	30.0	56.4
20	5.0	61.4



Table A2. GTN-P ALT sites used in the CLASS-CTEM evaluation. The mean ALT is calculated by first taking the mean of the sampling grid for each observation in time and then taking the mean across all observation times at each site. The standard deviation (SD) at each site is calculated across the sampling grid. The mean SD is then the average SD of the sampling grid across all observation times.

Name	Latitude (°N)	Longitude (°W)	Obs. period	Mean obs./yr	Mean ALT (m)	Mean SD over ALT grid (m)
1 Cape Chukochii R13a	70.08	159.92	2000 - 2015	0.94	0.41	0.09
2 Taglu Grid	69.37	-134.95	1998 - 2008	1.27	0.99	0.22
3 Mt Rodinka PLOT	68.75	161.50	2003 - 2015	1.00	0.99	0.14
4 Mt Rodinka Control Site	68.73	161.40	2003 - 2015	1.00	1.35	0.11
5 Urengoy GAS FIELD GP5	66.32	76.91	2008 - 2014	1.14	0.77	0.41
6 Vaskiny Dachi 2	70.30	68.88	2007 - 2015	1.00	0.70	0.12
7 Mt Rodinka Burn Site	68.72	161.53	2003 - 2015	0.77	1.53	0.09
8 Barrow	71.32	-156.60	1995 - 2015	1.52	0.36	0.08
9 Panteleekha River	68.42	161.22	1996 - 1996	1.00	0.45	0.12
10 Tiksi	71.58	128.78	1997 - 2000	1.25	0.42	0.11
11 Chukochya River	69.49	156.99	1996 - 2015	0.65	0.44	0.06
12 Betty Pingo	70.28	-148.87	1995 - 2015	1.43	0.52	0.17
13 Cape Rogozny	64.78	176.97	1994 - 2015	1.05	0.50	0.05
14 Zackenber ZEROCALM 2	74.47	-20.50	1996 - 2010	9.27	0.63	0.13
15 Chandalar Shelf	68.07	-149.58	1996 - 2015	0.90	0.36	0.09
16 Old Man	66.45	-150.62	1996 - 2015	0.85	0.40	0.04
17 Franklin Bluff	69.68	-148.72	1996 - 2015	1.00	0.62	0.15
18 Alexandria Fiord	78.88	-75.92	1996 - 2001	0.67	0.57	0.07
19 North Head Grid	69.72	-134.46	1998 - 2008	1.00	0.47	0.08
20 Lousy Point Grid	69.22	-134.29	1998 - 2008	1.00	0.56	0.13
21 Wickersham	65.27	-148.05	1972 - 2015	0.93	0.47	0.08
22 Allaiha	70.56	147.43	2004 - 2015	1.00	0.47	0.08
23 Talmakh	69.43	88.47	2008 - 2015	1.25	0.95	0.21
24 Igarka	67.48	86.44	2008 - 2017	1.10	0.76	0.32
25 Happy Valley 1km	69.10	-148.50	1995 - 2015	1.52	0.44	0.09



Table A2. continued

26	West Dock Iha	70.37	-148.55	1996 - 2015	1.00	0.31	0.07
27	Marre Sale	69.72	66.75	1995 - 2015	1.00	1.10	0.33
28	Segodnya Pingo	69.09	158.90	1996 - 2015	0.70	0.51	0.12
29	Tahnik	67.33	63.73	1998 - 2015	2.50	1.29	0.27
30	Zackenber ZEROCALM 1	74.47	-20.50	1996 - 2010	7.87	0.71	0.07
31	Malchikovskaya Channel	68.52	161.43	1996 - 2015	1.45	0.54	0.10
32	Ivotuk	68.48	-155.74	2000 - 2014	0.87	0.52	0.11
33	Konkovaya River R15a	69.41	158.45	1996 - 2015	0.70	0.35	0.07
34	Kuropatochya River R12a	70.92	156.63	1996 - 1996	1.00	0.37	0.09
35	Bykovsky Cape Plakor	71.79	129.42	2001 - 2014	0.86	0.33	0.06
36	Ayach	67.58	64.18	1996 - 2015	1.55	0.80	0.11
37	Vaskiny Dachi 1	70.28	68.89	2007 - 2015	1.00	0.70	0.09
38	Khomus2	69.98	153.58	2005 - 2005	1.00	0.54	0.09
39	Plosky Tolbachik 1	55.75	160.29	2003 - 2012	1.10	0.69	0.27
40	Bety Pingo WET	70.28	-148.92	1995 - 2015	1.48	0.41	0.05
41	Kougarok	65.46	-164.63	1999 - 2015	0.71	0.57	0.11
42	Norman Wells Grid	65.19	-126.47	1998 - 2008	1.18	0.46	0.12
43	Bolvansky	68.29	54.51	1999 - 2015	1.65	1.09	0.17
44	Kruglaya	64.63	176.97	2010 - 2015	1.00	0.45	0.07
45	Happy Valley Iha	69.17	-148.83	1996 - 2015	0.80	0.40	0.08
46	Tuymada	62.01	129.66	2008 - 2015	1.12	2.02	0.08
47	Innavait Creek MAT	68.61	-149.31	1995 - 2015	1.52	0.45	0.09
48	Lavrentiya	65.60	171.05	2000 - 2012	3.46	0.65	0.10
49	Bykovsky Cape Alas	71.78	129.40	2004 - 2015	0.92	0.31	0.07
50	Sagwon Hills MNT	69.44	-148.67	1995 - 2015	1.62	0.58	0.12
51	Mt Rodinka Station	68.70	161.55	2003 - 2015	1.00	0.77	0.14
52	Pearl Creek	64.90	-147.80	1969 - 2015	1.00	0.64	0.08
53	Atqasuk	70.45	-157.40	1995 - 2015	1.33	0.48	0.19
54	Andryushkino	69.17	154.43	2005 - 2015	1.55	0.38	0.11
55	Toolik 1km	68.62	-149.60	1995 - 2015	1.43	0.48	0.12



Table A2. continued

56	Deadhorse	70.17	-148.47	1996 - 2015	0.95	0.65	0.08
57	Yubileynoe 3 DRY	65.95	75.87	2007 - 2007	1.00	0.23	0.04
58	Betty Pingo MNT	70.28	-148.89	1995 - 2014	1.55	0.38	0.08
59	Samoylov	72.37	126.48	2002 - 2015	7.50	0.48	0.06
60	Toolik MAT	68.62	-149.62	1995 - 2015	1.52	0.45	0.10
61	Yubileynoe 2 DRY	66.01	75.78	2007 - 2007	1.00	0.27	0.08
62	Most	56.91	118.28	2013 - 2014	1.00	0.49	0.08
63	Belenkiy	56.76	118.19	2013 - 2014	1.00	0.54	0.14
64	Fort Simpson Grid	61.89	-121.60	1999 - 2008	1.00	0.90	0.24
65	Lorino	65.54	-171.63	2010 - 2012	1.00	0.47	0.11
66	Bykovsky Cape	71.78	129.42	2015 - 2015	1.00	0.34	0.05
67	Plosky Tolbachik 2	55.76	160.32	2004 - 2012	1.00	0.56	0.04
68	Kuropatochya River R12b	70.92	156.63	1996 - 1996	1.00	0.27	0.08
69	Kashin Island	68.23	53.85	2010 - 2015	1.50	0.74	0.19
70	Rengleng River Grid	67.80	-134.13	1998 - 2008	1.18	0.78	0.13
71	Khomus1	69.98	153.58	2005 - 2005	1.00	0.51	0.09
72	Tahnik	67.33	63.73	1999 - 2015	2.24	0.58	0.14
73	Konkovaya River R15b	69.41	158.45	1999 - 2015	0.71	0.45	0.06
74	Akhmelo Channel	68.81	160.99	1996 - 2015	0.95	0.52	0.08
75	Cape Chukochii R13b	70.08	159.92	1999 - 2015	1.00	0.43	0.06
76	Willowlake River Grid	62.70	-123.06	2001 - 2008	1.00	0.81	0.19
77	Alazeya River	69.32	154.97	1998 - 2015	0.78	0.51	0.09
78	West Dock 1km	70.37	-148.56	1995 - 2015	1.43	0.50	0.12
79	Yubileynoe 2 WET	66.01	75.78	2007 - 2007	1.00	0.28	0.04
80	Mountain Dionisiya	64.57	177.20	1996 - 2015	0.95	0.55	0.10
81	Yubileynoe 3 WET	65.95	75.87	2007 - 2007	1.00	0.35	0.03
82	UNISCALM	78.20	15.75	2011 - 2015	1.00	1.03	0.06
83	Yakutskoe Lake	69.85	159.49	1999 - 2015	0.82	0.46	0.06



Table A2. continued

84	Neleger	62.32	129.50	2008 - 2015	1.00	1.24	0.10
85	Lake Glukhoe	68.80	160.96	1996 - 2015	0.95	0.85	0.16
86	Svyatoy Nos Cape	72.86	141.01	2001 - 2001	1.00	0.38	0.04
87	Parisento	70.12	75.58	1992 - 1995	0.75	0.91	0.31
88	Bonanza Creek	64.75	-148.00	1990 - 2015	0.96	0.71	0.11
89	Vaskiny Dachi 3	70.30	68.84	2007 - 2015	1.00	1.13	0.13
90	Imnavait 1km	68.50	-149.50	1995 - 2015	1.48	0.52	0.10
91	Nadym Grid	65.33	72.92	1997 - 2016	1.25	1.35	0.48
92	Urengoy GAS FIELD GP15	67.48	76.70	2008 - 2015	1.00	0.84	0.15
93	Reindeer Depot Grid	68.68	-134.15	2000 - 2008	1.11	1.10	0.10
94	Council	64.84	-163.71	1999 - 2015	0.71	0.57	0.33
95	Lake Akhmelo	68.83	161.03	1996 - 2015	0.95	0.97	0.16
96	Galbraith Lake	68.48	-149.50	1996 - 2015	0.90	0.53	0.09
97	Tolbachinsky Pass	55.89	160.54	2006 - 2015	0.90	0.47	0.02



Table A3. GTN-P permafrost temperature (borehole) sites used in the CLASS-CTEM evaluation.

Name	Latitude (°N)	Longitude (°W)	GTN-P site number	Permafrost zone	Number of observations
1 Chevak	61.54	-165.60	746	Continuous	45
2 Smith Lake 4	64.87	-147.86	619	Discontinuous	964
3 Circle	65.82	-144.07	752	Discontinuous	105
4 Tobolsk aerologicheskaya	58.15	68.18	1670	None	1079
5 Belenkiy	56.76	118.19	1835	Continuous	34
6 Kerak	57.98	125.50	686	Discontinuous	99
7 Bayandai	53.10	105.53	1674	Isolated	1536
8 Rubtsovsk	51.50	81.22	1666	None	1403
9 Ust	65.45	52.17	1699	None	954
10 Karam	55.33	107.50	1676	Sporadic	990
11 Olkhon	53.23	107.44	1135	Sporadic	82
12 Nadym Pingo	65.30	72.89	178	Discontinuous	169
13 Franklin Bluffs dry b	69.67	-148.72	103	Continuous	691
14 Mould Bay	76.23	-119.30	1108	Continuous	24
15 Ishim	56.13	69.52	1605	None	1550
16 ILU2007	69.22	-51.10	535	Discontinuous	213
17 Taiga	56.07	87.62	1663	None	565
18 Vologda Molochnoe	59.28	39.87	1648	None	579
19 Svobodnyi	51.45	128.12	1623	None	1546
20 Russkaya Polyana	53.83	73.83	1610	None	1089
21 Omega	63.90	38.12	1658	No	1225
22 Berezovo	63.93	65.05	1639	Sporadic	1090
23 Komsomolsk	51.08	137.03	1693	Sporadic	1248
24 Nozhovka	57.08	54.75	1637	None	808
25 Deadhorse 2 new instrumentation	70.16	-148.47	88	Continuous	699



Table A3. continued

26	Turukhansk	65.78	87.95	1652	Discontinuous	1369
27	Boguchany	58.42	97.40	1704	Isolated	1567
28	Saranpaul	64.28	60.88	1638	Discontinuous	1070
29	Smith Lake 3	64.87	-147.86	618	Discontinuous	1134
30	West Dock 1 surface	70.37	-148.55	118	Continuous	436
31	Sagwon MNT	69.43	-148.67	116	Continuous	1021
32	Kupino	54.37	77.28	1620	None	1253
33	Vyazemskaya	47.55	134.82	1689	None	1627
34	Rodino	52.50	80.20	1705	None	1396
35	West Dock 1 surface	70.37	-148.55	118	Continuous	1061
36	Irkutsk obs grass	52.28	104.30	1653	Sporadic	1589
37	Tyumen	57.15	65.50	1647	None	1642
38	Eniseisk	58.45	92.15	1657	None	1356
39	Smith Lake 2	64.87	-147.86	620	Discontinuous	991
40	Bikin	46.80	134.27	1694	None	1061
41	Ivotuk 3	68.48	-155.74	65	Continuous	39
42	Anderson	64.35	-149.20	845	Discontinuous	90
43	Makushino	55.25	67.30	1697	None	1350
44	Barnaul agricst	53.33	83.70	1673	None	1358
45	Tura	64.17	100.07	1641	Continuous	1092
46	Yartsevo	60.25	90.23	1642	Isolated	1500
47	Banks Island	73.22	-119.56	1107	Continuous	478
48	Salmon Lake	64.91	-165.05	1191	Discontinuous	185
49	Azarova	56.90	117.58	54	Continuous	52
50	Franklin Bluffs dry be	69.67	-148.72	104	Continuous	280



Table A3. continued

51	Bomnak	54.72	128.93	1696	Discontinuous	1064
52	Irkutsk obs bare soil	52.28	104.30	1695	Sporadic	244
53	Tolstovka Amurskaya agexpst	50.17	127.92	1687	None	1629
54	Kamen	53.80	81.33	1622	None	1391
55	Isil	54.90	71.27	1649	None	1627
56	Ivdel	60.68	60.43	1631	None	839
57	Eletsckaya	67.17	64.17	1645	Sporadic	619
58	Erbogachen	61.27	108.02	1654	Continuous	1331
59	Anaktuvuk Pass	68.15	-151.72	833	Continuous	44
60	Tashtyp	52.80	99.88	1671	Continuous	1521
61	Solyanka	56.17	95.27	1682	None	1340
62	Ivotuk 4	68.48	-155.74	74	Continuous	316
63	Howe Island 1 b	70.32	-147.99	93	Continuous	568
64	Tatarsk	55.20	75.97	1661	None	842
65	Khanovey	67.29	63.65	1184	Continuous	29
66	Slavgorod	53.97	78.65	1665	None	1476
67	Troitsko	62.70	56.20	1698	None	983
68	Begotol	56.23	89.58	1617	None	1176
69	Last Bridge	65.39	-164.66	1188	Continuous	60
70	Olkhon	53.23	107.44	1118	Sporadic	138
71	Sidorovsk	66.67	82.33	1678	Discontinuous	1380
72	Rhonda Basin	66.57	-164.48	1185	Continuous	49
73	Shimanovskaya	51.98	127.65	1624	None	857
74	Franklin Bluffs surface	69.66	-148.72	106	Continuous	1131
75	Ambler	67.08	-157.87	780	Continuous	57



Table A3. continued

76	Olkhon	53.23	107.44	1136	Sporadic	82
77	Nadym ND3 4	65.31	72.86	176	Discontinuous	116
78	Belenkiy	56.76	118.19	224	Discontinuous	192
79	Leushi	59.62	65.78	1643	None	1061
80	Sterlitamak	53.62	55.98	1616	None	1135
81	Mould Bay	76.23	-119.30	1108	Continuous	1304
82	Franklin Bluffs dry ib	69.67	-148.72	105	Continuous	1103
83	Krasnoyarsk expfield	56.00	92.88	1655	None	1447
84	Barabinsk	55.37	78.40	1662	None	1046
85	Minusinsk expfield	53.70	91.70	1656	None	1119
86	Tulun agro	54.60	100.63	1686	Isolated	1591
87	Kolpashev	58.30	82.90	1659	None	1187
88	Sykyvkar 1	61.67	50.85	1672	None	969
89	Rhonda Upland	66.56	-164.46	1186	Continuous	79
90	Howe Island 1 ib	70.32	-147.99	94	Continuous	104
91	Ust	65.97	56.92	1614	None	1387
92	Zima ratlst	53.93	102.05	1677	Isolated	1109
93	Kosh	50.02	88.68	1707	Discontinuous	938
94	Aldan D	57.53	124.53	692	Discontinuous	80
95	Khomutovo	52.50	104.33	1685	None	1052
96	Kotkino	67.02	51.20	1611	Sporadic	496
97	Happy Valley 1 b	69.15	-148.85	95	Continuous	380
98	Nadym ND3	65.31	72.86	175	Discontinuous	246
99	Franklin Bluffs dry b	69.67	-148.72	103	Continuous	447
100	Biisk zonalnaya	52.68	84.95	1621	None	1349



Table A3. continued

101	Ivotuk 4	68.48	-155.74	74	Continuous	51
102	Ivotuk 3	68.48	-155.74	65	Continuous	245
103	Happy Valley 1 ib	69.15	-148.85	110	Continuous	441
104	Ust	61.80	57.92	1675	None	603
105	Poliny Osipenko	52.42	136.50	1690	Sporadic	1535
106	Tunka	51.73	102.53	1668	Continuous	1588
107	Olkhon	53.23	107.44	1840	Sporadic	36
108	Ushelistiy	56.54	118.48	227	Continuous	94
109	Ivotuk 3	68.48	-155.74	65	Continuous	140
110	Skovorodino	54.00	123.97	1612	Sporadic	854
111	Tomsk	56.43	84.97	1660	None	697
112	Nadym PiCla	65.31	72.89	177	Discontinuous	49
113	Franklin Bluffs wet b	69.66	-148.72	107	Continuous	310
114	Mary s Igloo East	65.11	-164.70	1190	Discontinuous	160
115	Kazachinskoe expfield	57.75	93.18	1681	None	569
116	Kargopol	61.50	38.95	1627	None	1216
117	Deadhorse 1 surface	70.16	-148.47	87	Continuous	972
118	Shitikino	56.37	98.37	1669	None	1038
119	Tarko	64.92	77.82	1606	Discontinuous	1003
120	Howe Island 1 ib	70.32	-147.99	94	Continuous	512
121	Kalachinsk	55.03	74.58	1644	None	1163
122	Nadym ND2	65.31	72.89	174	Discontinuous	160
123	Banks Island	73.22	-119.56	1107	Continuous	385
124	Olkhon	53.22	107.45	1137	Sporadic	70
125	Belenkiy	56.76	118.19	1116	Continuous	231



Table A3. continued

126	Vikulovo	56.82	70.62	1646	None	1295
127	Mould Bay	76.23	-119.30	1108	Continuous	1092
128	Konosha	61.00	40.17	1700	None	659
129	Srednii Vasyugan Vasyuganskoe	59.22	78.23	1684	None	1169
130	Khosedá	67.08	59.38	1701	Discontinuous	933
131	Ivotuk 4	68.48	-155.74	74	Continuous	508
132	Erofei Pavlovich	53.97	121.93	1651	Sporadic	814

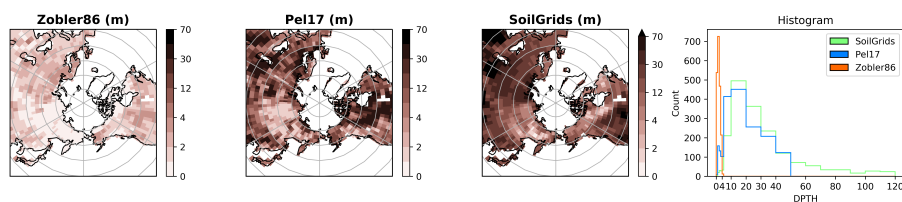


Figure A1. Comparison of soil permeable depth datasets from Zobler86 (Zobler, 1986), Pel16 (Pelletier et al., 2016), and SoilGrids (Shang-guan et al., 2017).

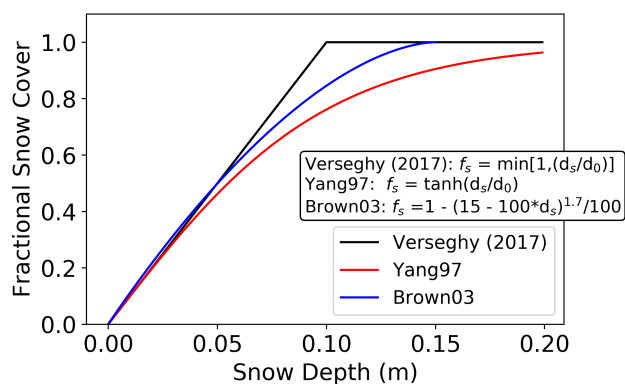


Figure A2. Snow cover as a function of snow depth for the CLASS-CTEM linear relation (Verseggy, 2017), the hyperbolic tangent form of Yang et al. (1997), and the exponential relationship proposed by Brown et al. (2003)

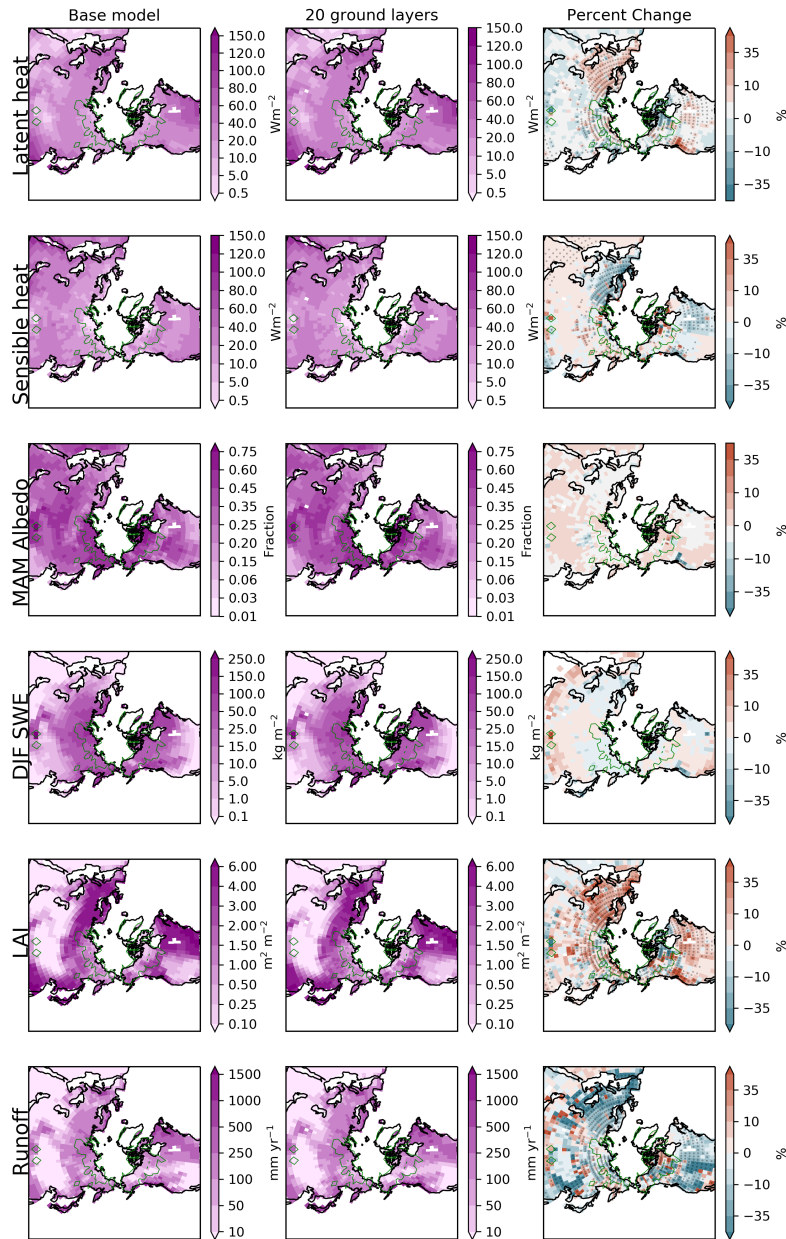


Figure A3. Comparison of mean annual latent and sensible heat fluxes, spring (March, April, May; MAM) total surface albedo, winter (December, January, February; DJF) snow water equivalent (SWE), mean annual leaf area index (LAI) and total runoff. Positive percent change values indicate that the '20 ground layer' experiment has higher values of a quantity than the 'Base model' while negative values indicate the opposite. The green polygon indicates regions of permafrost simulated by that experiment. The green polygon on the percent change plots is the permafrost region from the '20 ground layers' experiment. Dots indicate grid cells that are statistically significant (independent two-sample t-test p level < 0.05). The left column shows the results from the original model version ('Base model') while the middle column shows the '20 ground layer' experiment.

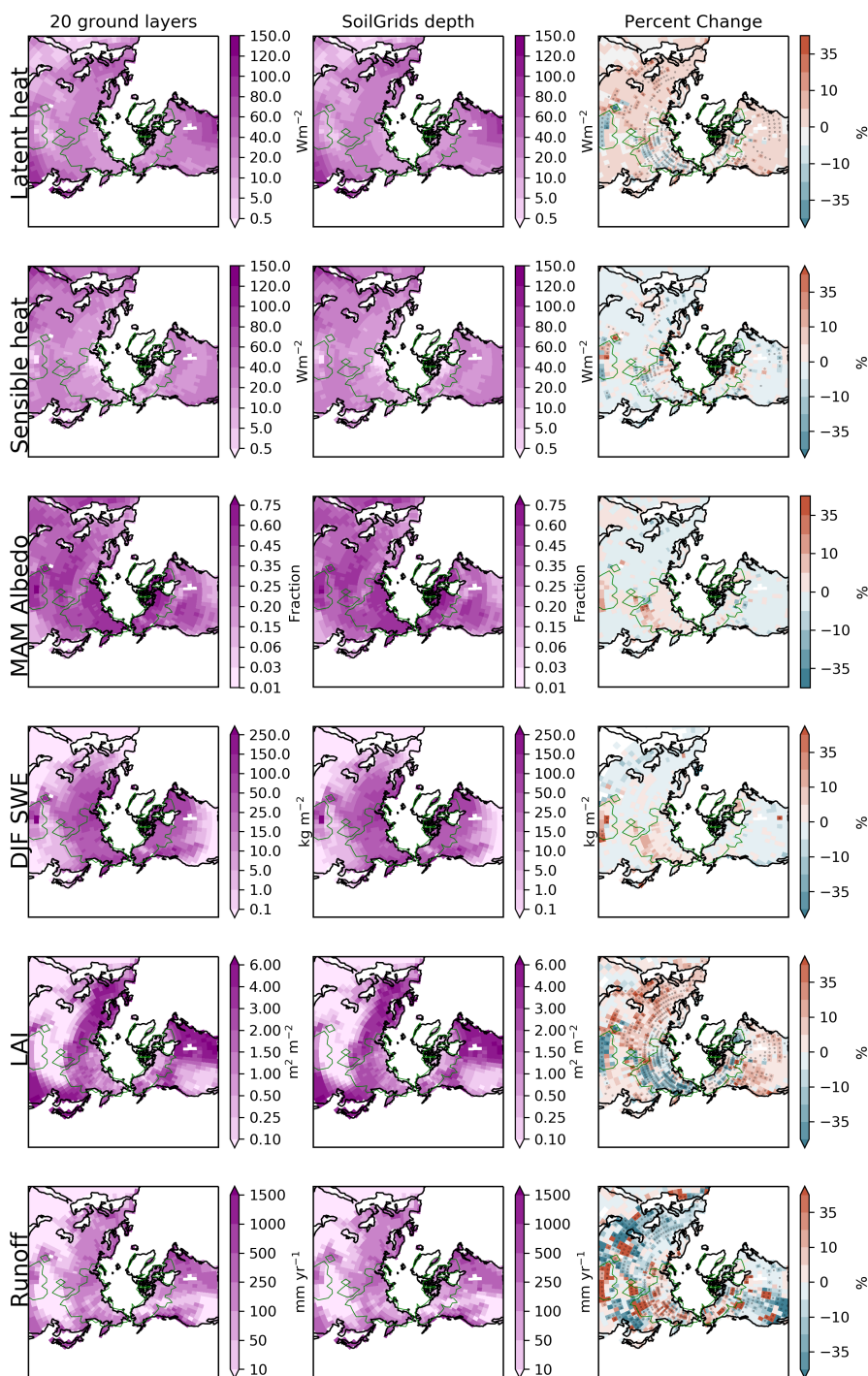


Figure A4. Same as Figure A3 but for experiments '20 ground layers' and 'SoilGrids depth'

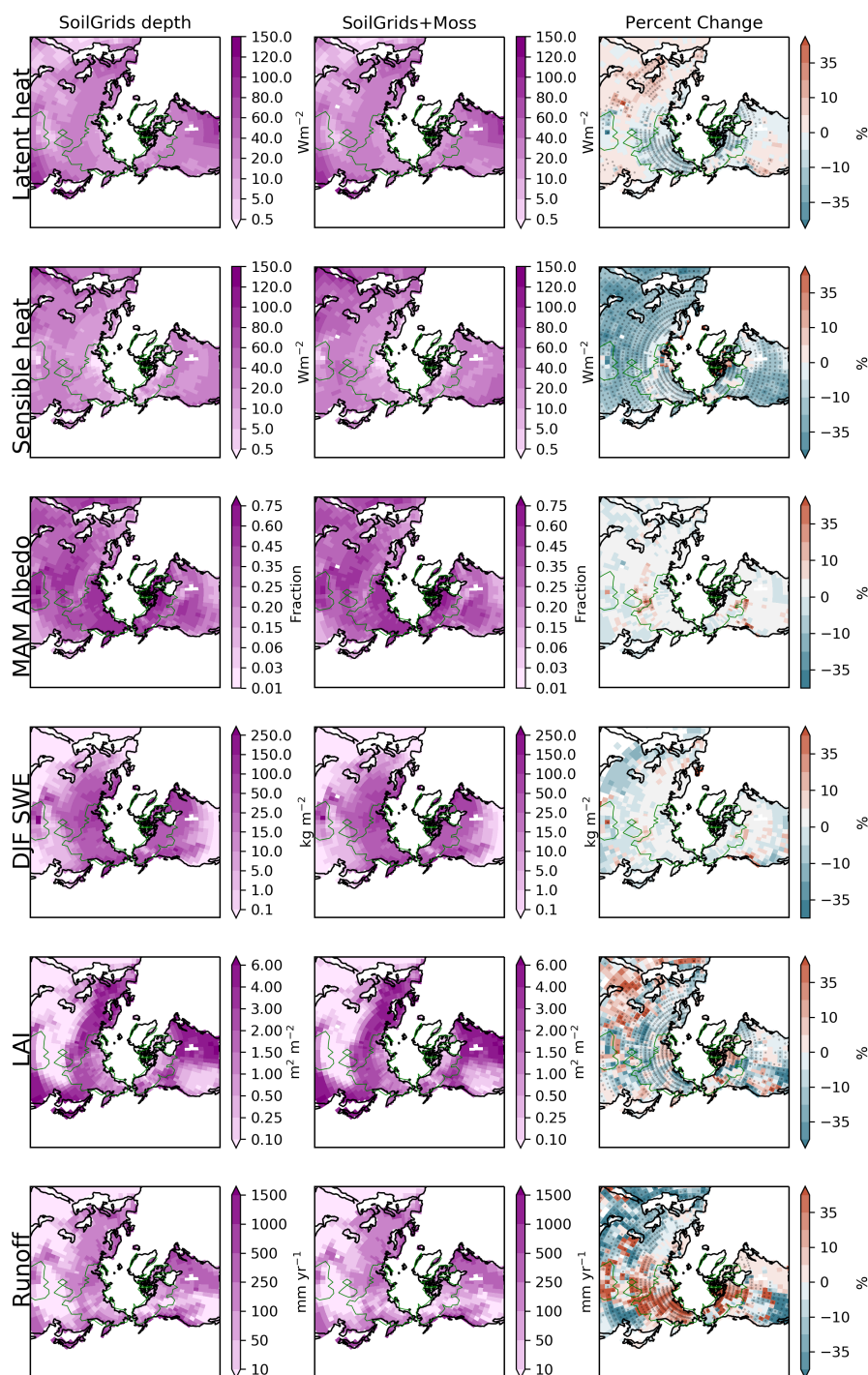


Figure A5. Same as Figure A3 but for experiments 'SoilGrids depth' and 'SoilGrids+Moss'

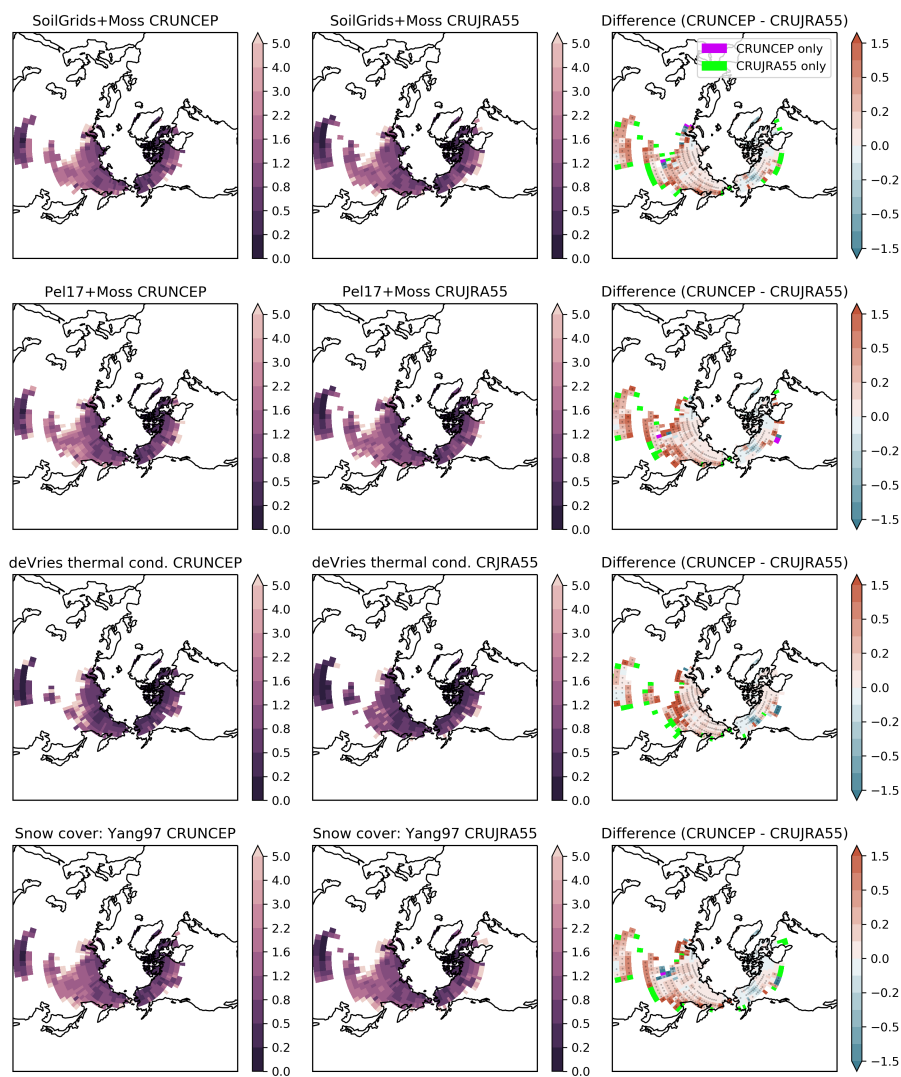


Figure A6. ALTs for experiments 'SoilGrids+Moss', 'Pel16+Moss', 'deVries thermal cond.', and 'Snow cover: Yang97' using the CRUNCEP meteorological forcing dataset (left column), CRUJRA55 meteorological forcing dataset (middle column), and their difference (right column). Dots indicate grid cells that are statistically significant (independent two-sample t-test p level < 0.05).

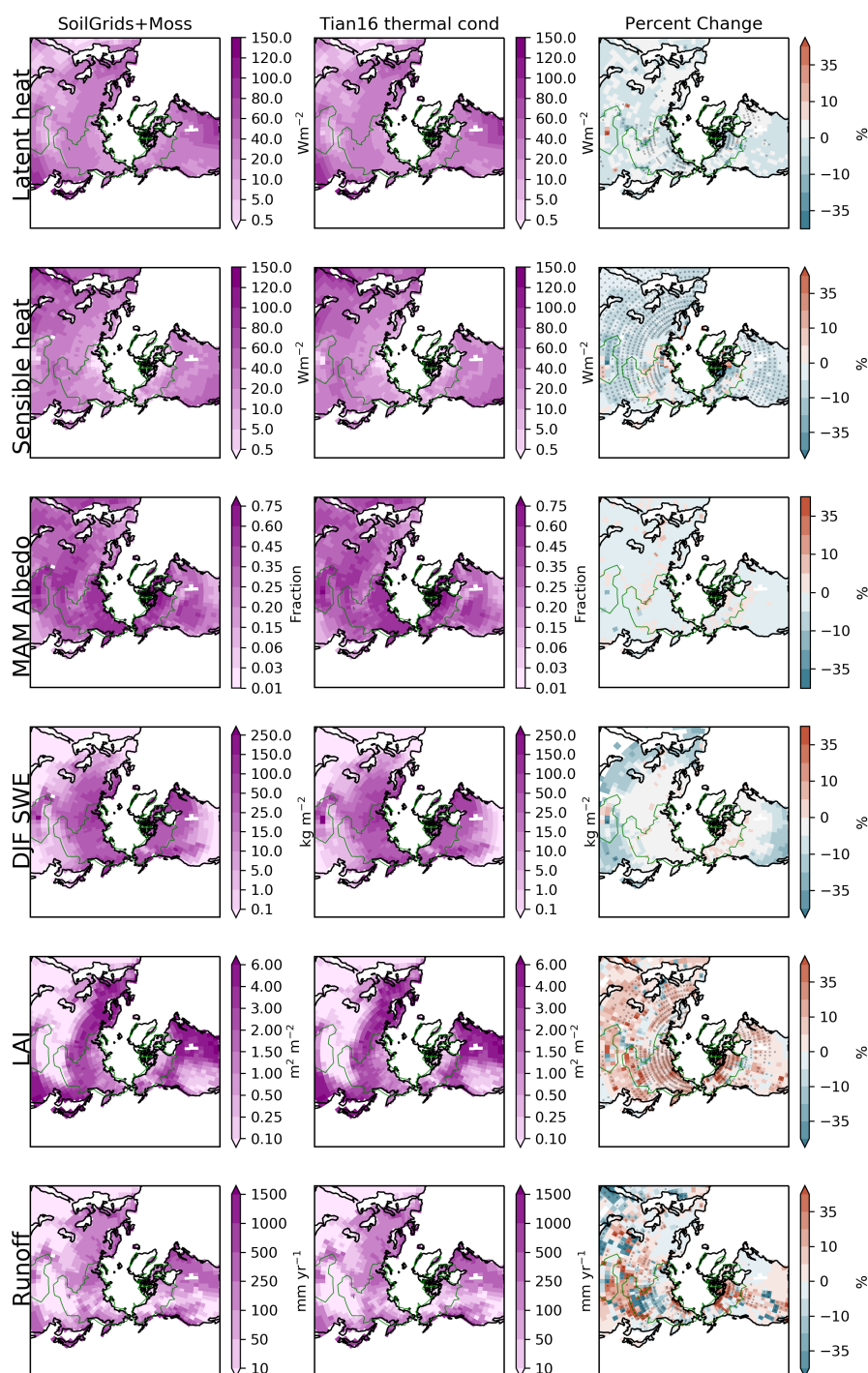


Figure A7. Same as Figure A3 but for experiments 'SoilGrids+Moss' and 'Tian16 thermal cond.'

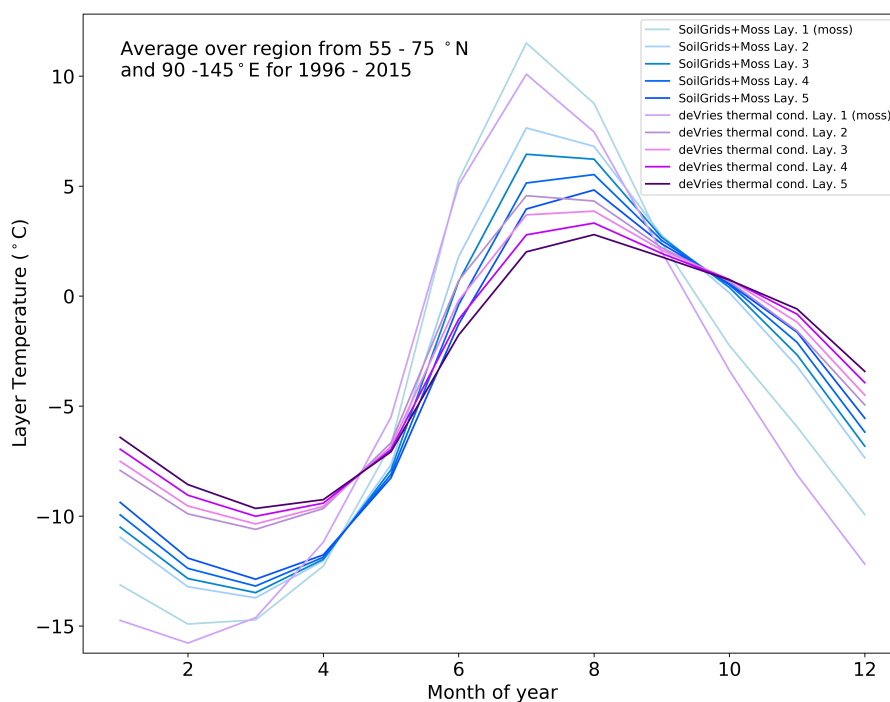


Figure A8. Mean monthly soil temperature over a permafrost region in eastern Siberia for the top 5 ground layers for the 'SoilGrids+Moss' and 'deVries thermal cond.' experiments. The first layer is moss in both simulations.

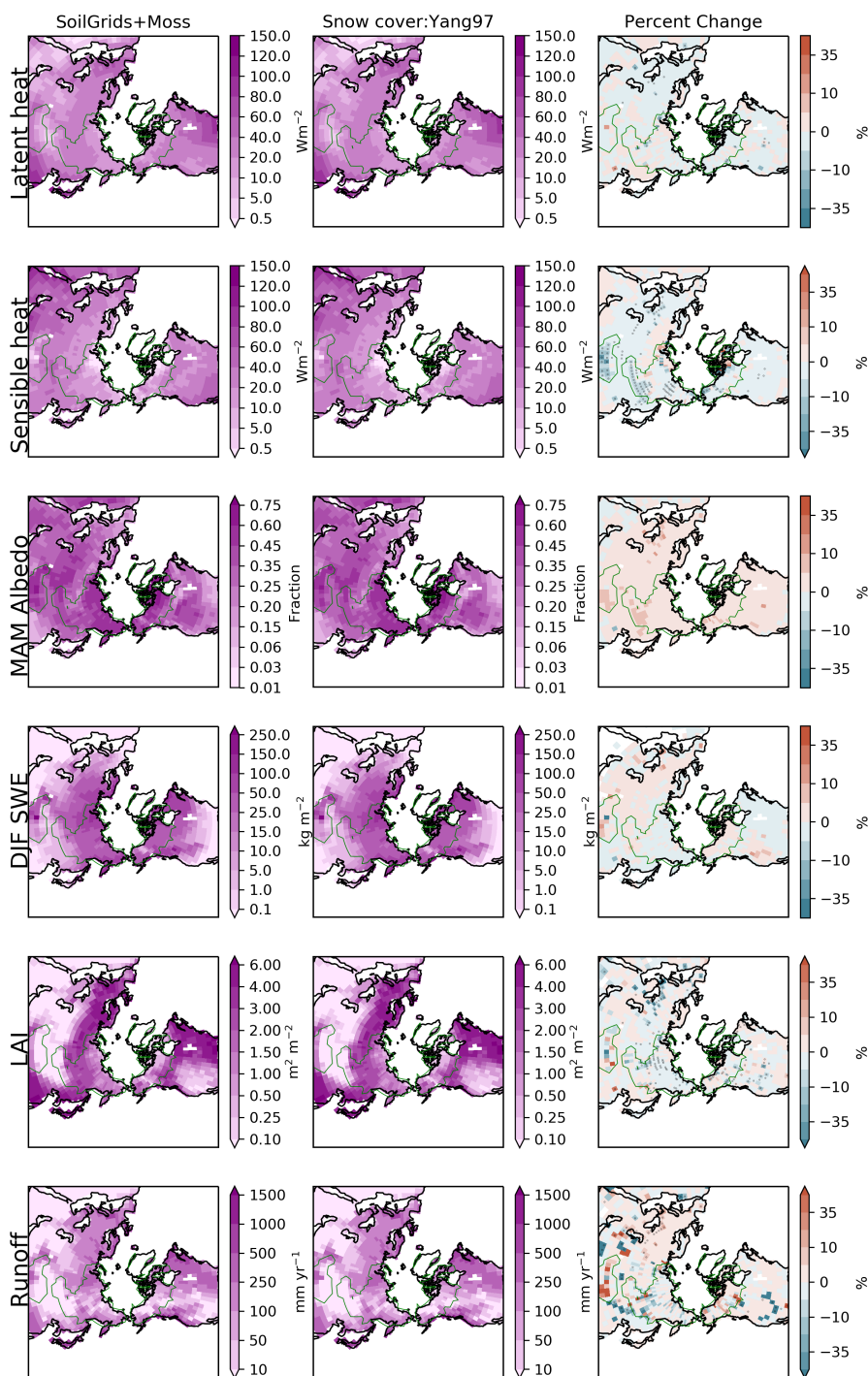


Figure A9. Same as Figure A3 but for experiments 'SoilGrids+Moss' and 'Snow cover: Yang97'

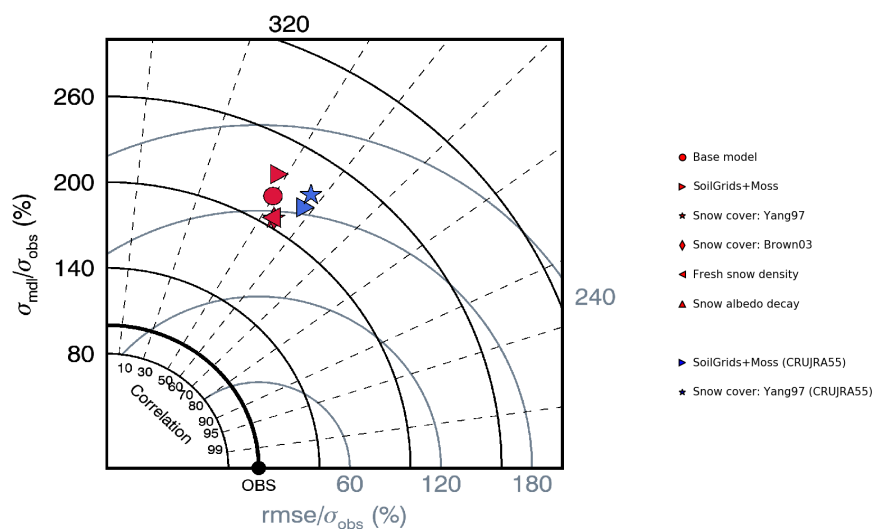


Figure A10. Taylor diagrams for winter (DJF) SWE compared to Blended-5 for the period spanning January 1981 to December 2010. Blended-5 is a multi-dataset SWE product developed by Mudryk et al. (2015) that combines five observation-based SWE datasets. Exp. ‘Snow albedo decay’ is outside the plot boundaries. This plot shows anomaly correlation coefficient as well as ratio of standard deviations and root mean square error normalized by the standard deviation from observations. Values shown correspond to the centroid over the values obtained for every grid cell northward of 45°N, with climatological SWE > 4 mm to avoid regions of ephemeral snow.

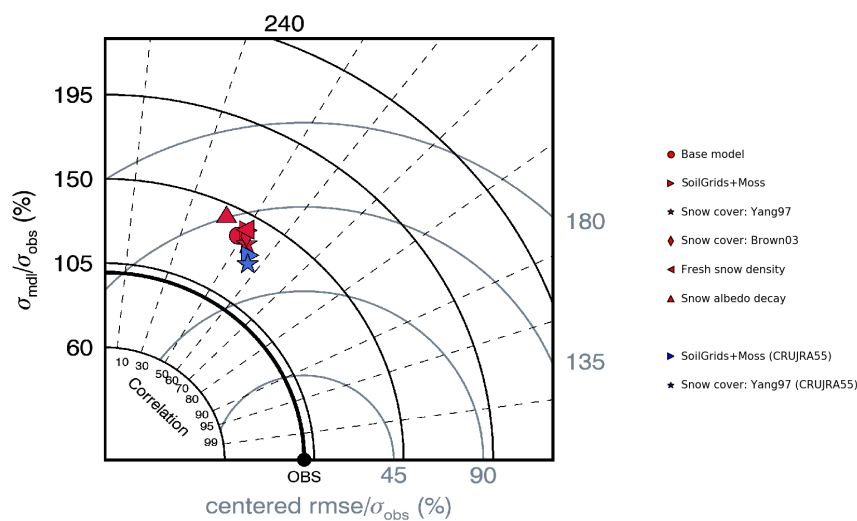


Figure A11. Taylor plot of total spring albedo (AMJ) compared to MODIS MCD43C3 white-sky albedo (MODIS Adaptive Processing System, NASA, 2016) for the period spanning February 2000 to December 2013. The Taylor plot shows the anomaly correlation coefficient (polar coordinates), ratio of standard deviations (y axis) and root mean square error (RMSE) normalized by the standard deviation from observations (x axis). Values shown correspond to the centroid over the values obtained for every grid cell northward of 45°N.

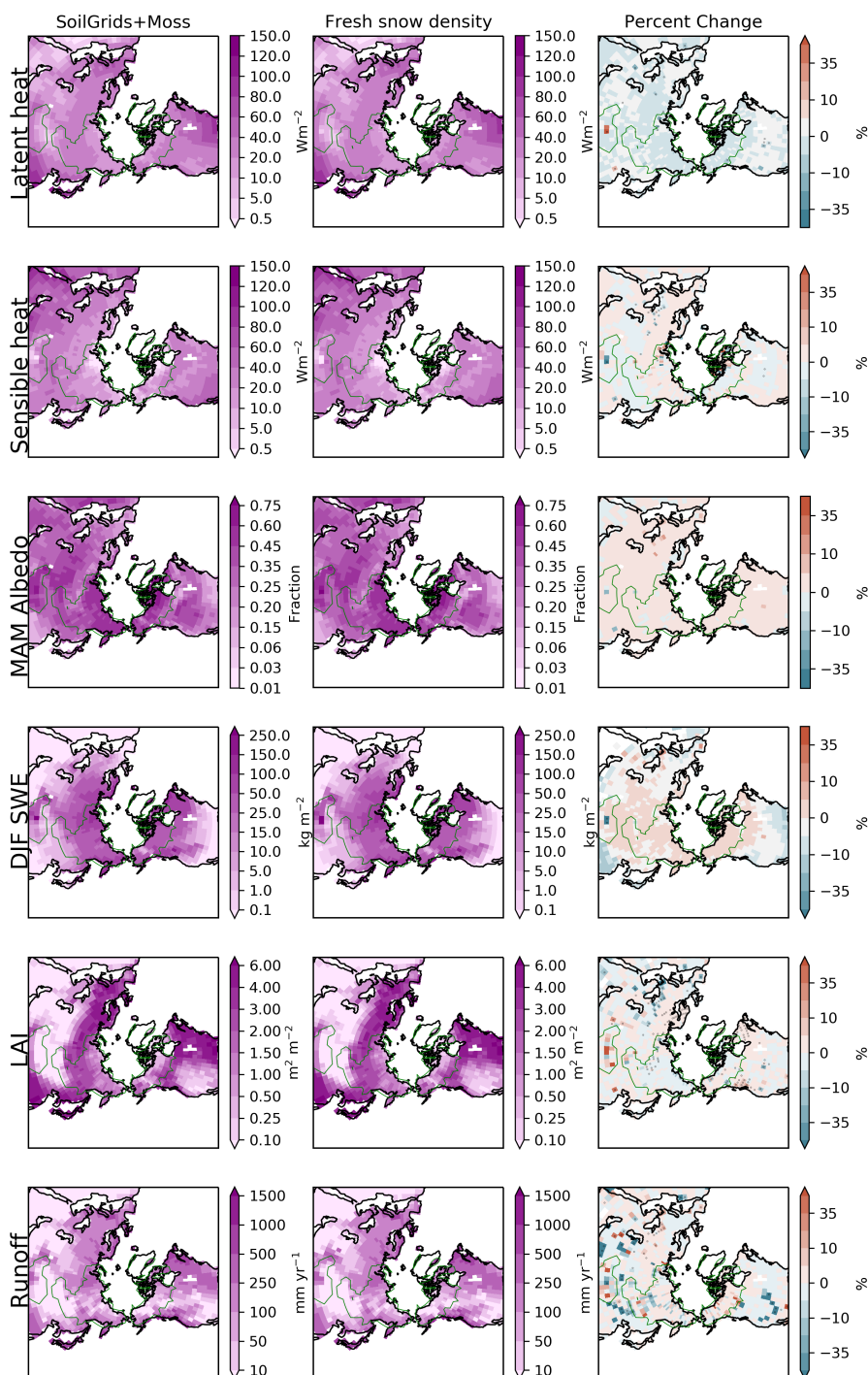


Figure A12. Same as Figure A3 but for experiments 'SoilGrids+Moss' and 'Fresh snow density'.

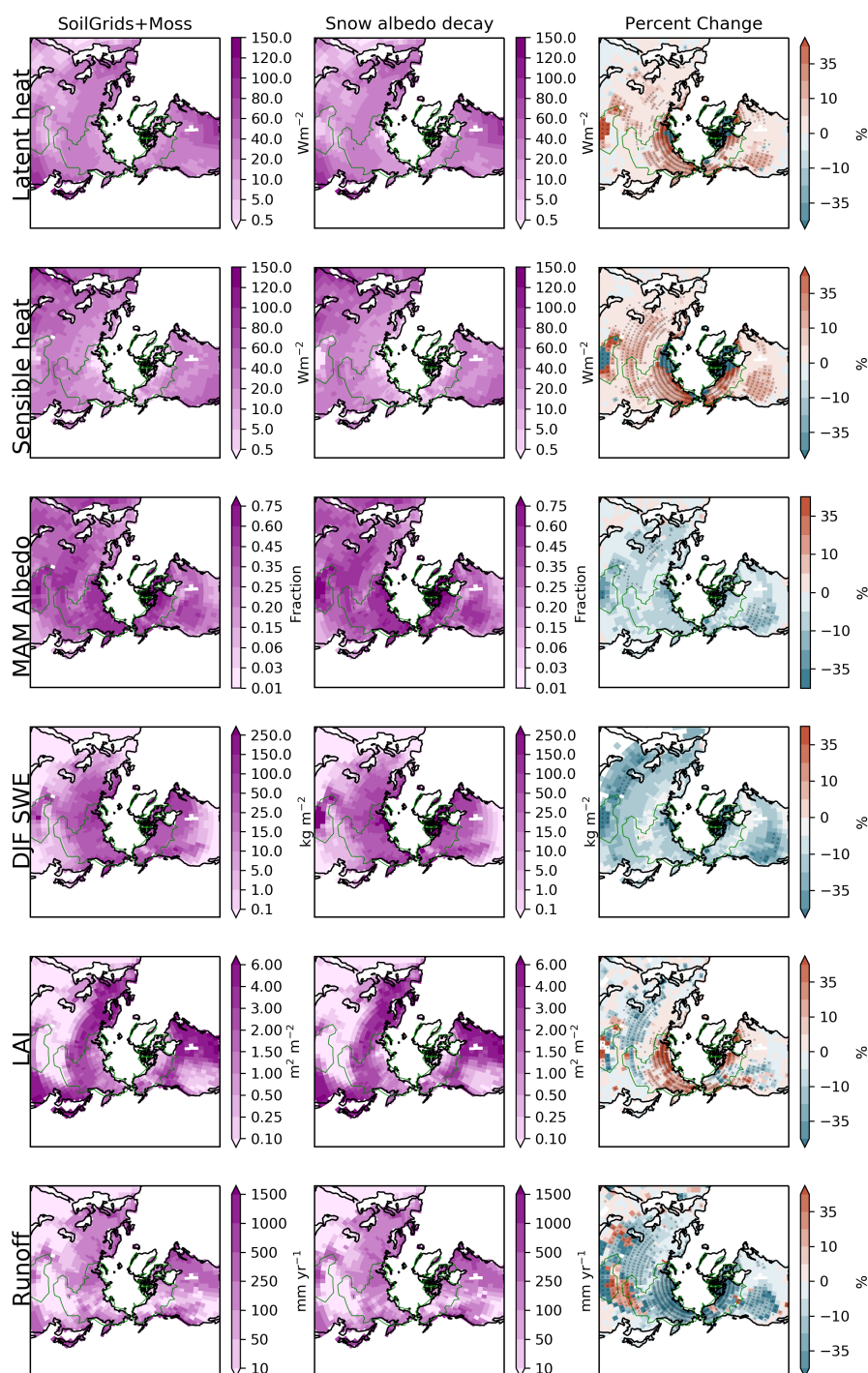


Figure A13. Same as Figure A3 but for experiments 'SoilGrids+Moss' and 'Soil albedo decay'.

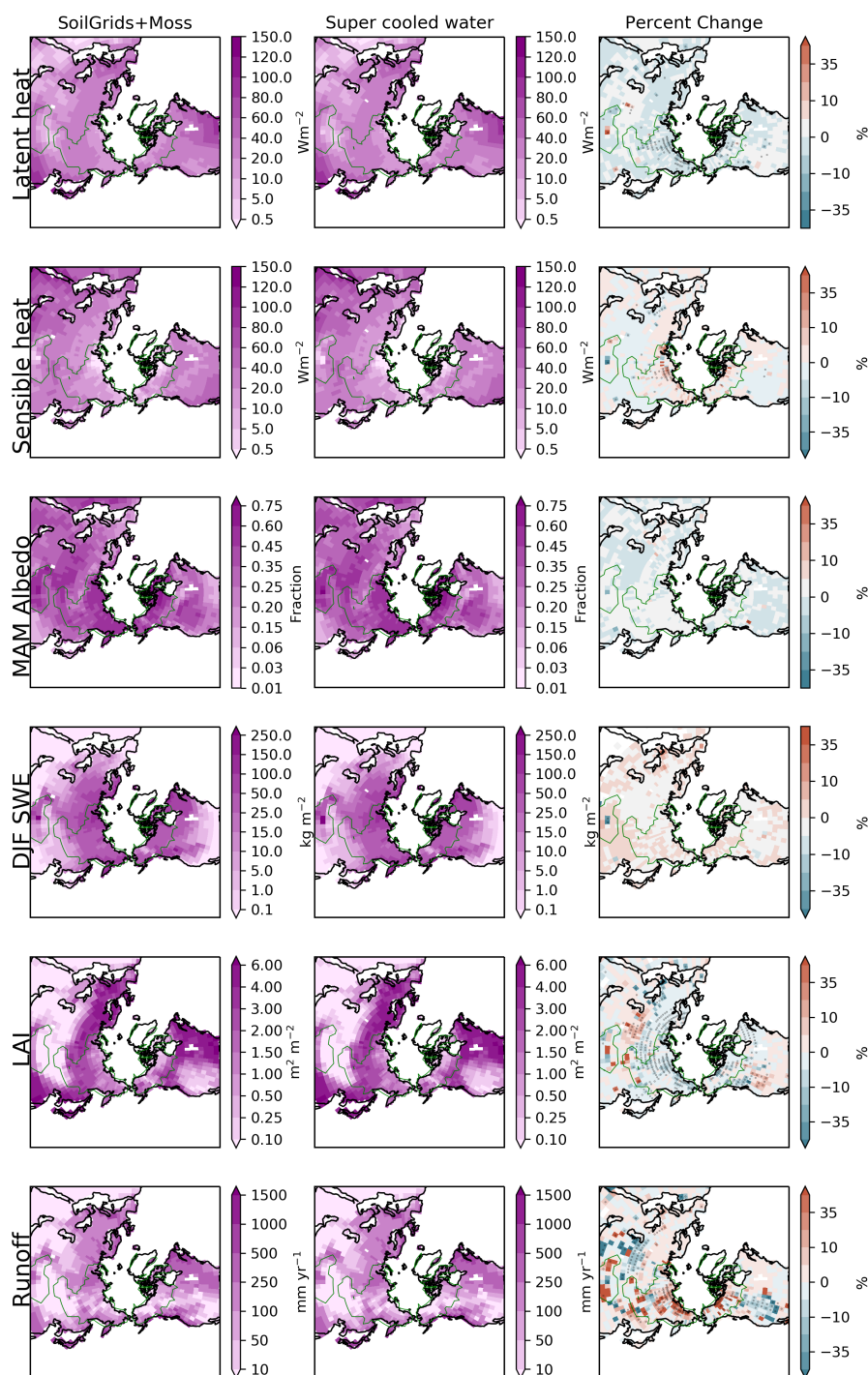


Figure A14. Same as Figure A3 but for experiments 'SoilGrids+Moss' and 'Super-cooled water'.

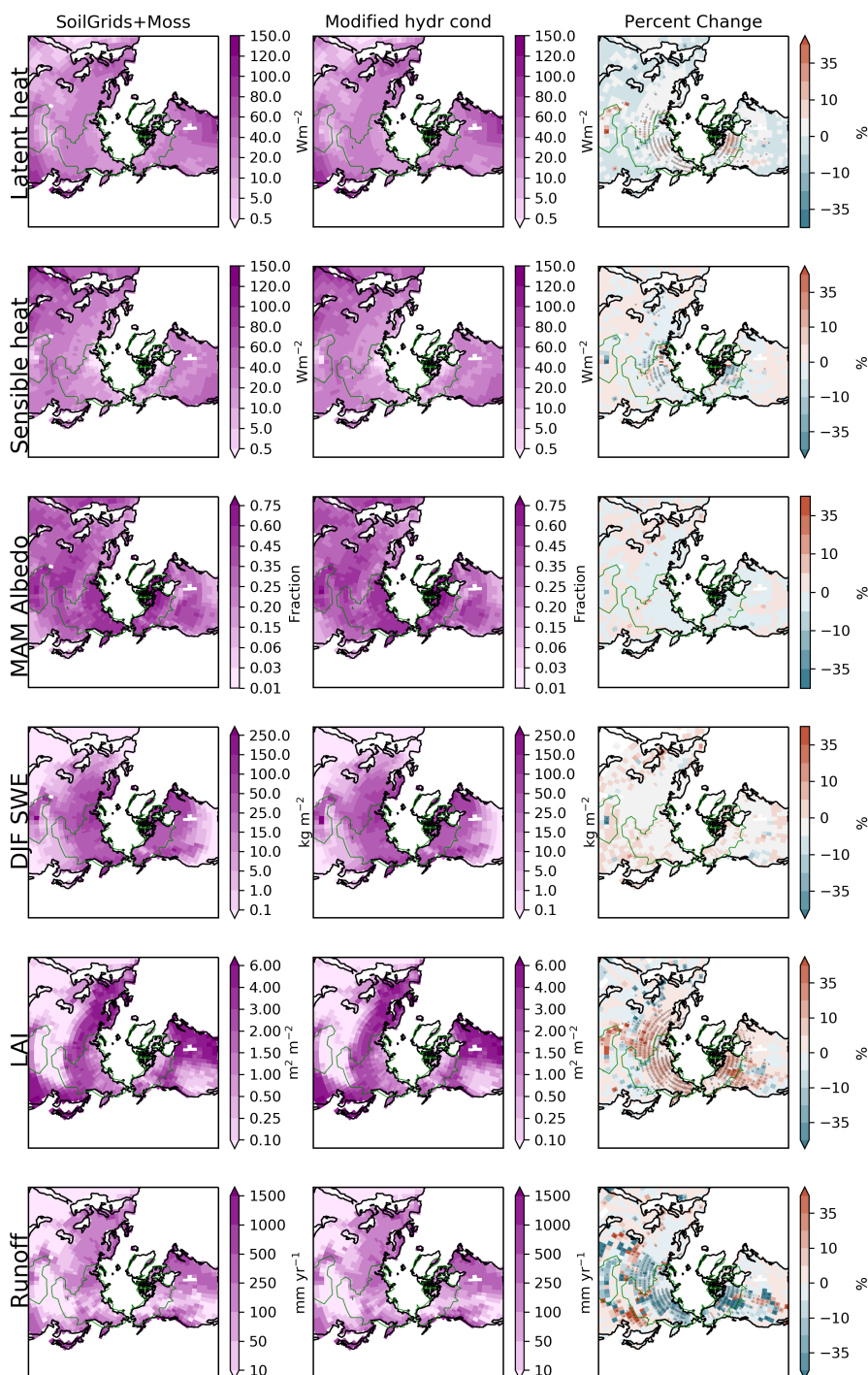


Figure A15. Same as Figure A3 but for experiments 'SoilGrids+Moss' and 'Modif. hydrology'.

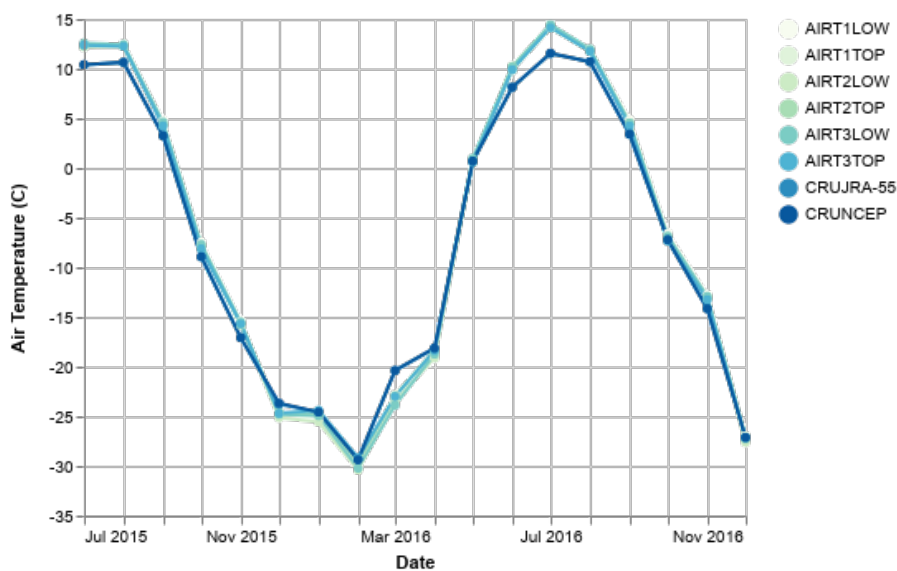


Figure A16. Mean monthly 2 m air temperature at Lac de Gras sites from meteorological stations as part of the Slave Province Surficial Materials and Permafrost Study (SPSMPS) (Gruber et al., 2018) and reanalysis meteorological datasets CRUNCEP (Viovy, 2016) and CRUJRA55 (Harris et al., 2014; Kobayashi et al., 2015)

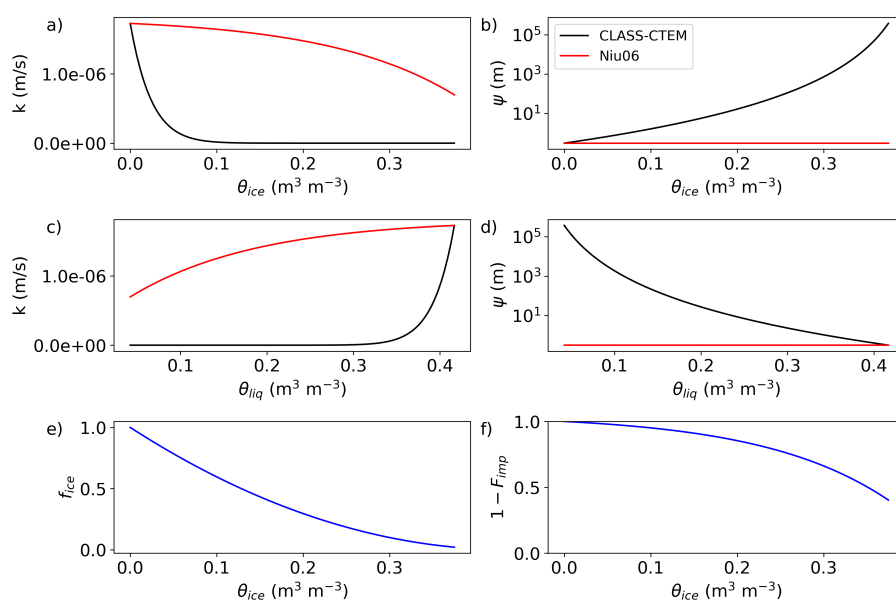


Figure A17. Soil hydraulic conductivity (a,c) and matric potential (b,d) for a soil with sand and clay content by weight of 40% and 20%, respectively, with a maximum saturation level of 95%. The Zhao and Gray (1997) f_{ice} and the Niu and Yang (2006) $(1 - F_{imp})$ parameters are shown in plots e and f, respectively.

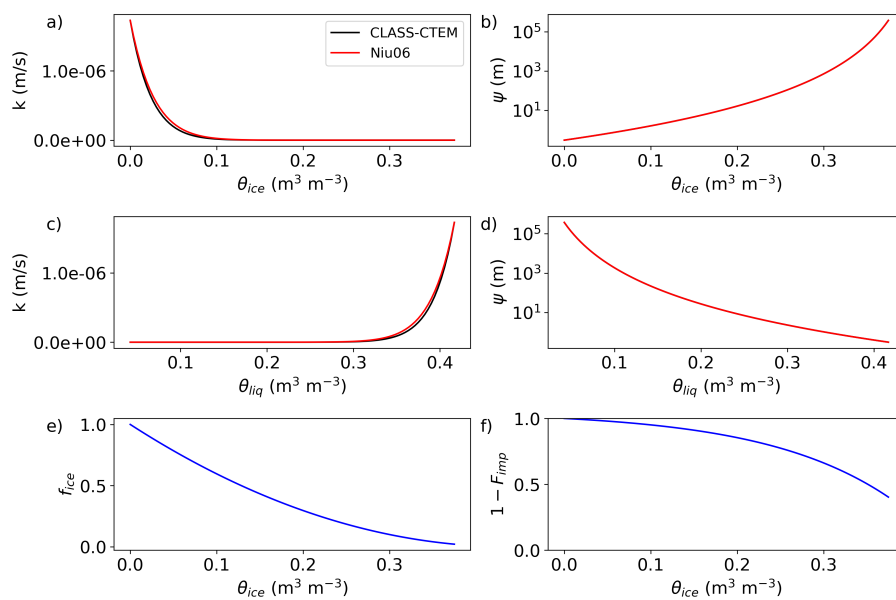


Figure A18. Same as Figure A17 but the θ_{ice} term is removed from the numerator of equations B6 and B7.



Author contributions. JRM initiated the study, performed the model simulations and analysis and wrote the paper. DV led the development of the CLASS model, conducted initial research into the recommendations of MacDonald (2015) and was liaison to the Sushama group for the work of Arman Ganji. RS-A performed the statistical analysis and plotting for SWE and MODIS albedo. SG provided the Lac de Gras data and participated in discussions around model evaluation. All authors contributed to the final version of the paper.

5 *Competing interests.* None

Acknowledgements. We thank the Global Terrestrial Network for Permafrost for generously sharing their data and for making it easily accessible on-line. We thank Dr. Vivek Arora for processing the CRUJRA55 meteorological data, Mr. Ed Chan for processing the MODIS data, and Drs. Christian Seiler and Paul Bartlett for providing comments on a pre-submission version of our MS. Sampling at the Khanovey site is supported by the RuNoCORE CPRU-2017/10015 <https://www.siu.no/eng/content/view/full/81242> ; the SAMCoT WP6

10 <https://www.ntnu.edu/web/samcot/home> and Lomonosov Moscow state university, Geology faculty, permafrost department.



References

- Alexeev, V. A., Nicolsky, D. J., Romanovsky, V. E., and Lawrence, D. M.: An evaluation of deep soil configurations in the CLM3 for improved representation of permafrost, *Geophys. Res. Lett.*, 34, 2007.
- Arora, V., Seglenieks, F., Kouwen, N., and Soulis, E.: Scaling aspects of river flow routing, *Hydrol. Process.*, 15, 461–477, <https://doi.org/10.1002/hyp.161>, 2001.
- 5 Bartlett, P. A., MacKay, M. D., and Verseghy, D. L.: Modified snow algorithms in the Canadian land surface scheme: Model runs and sensitivity analysis at three boreal forest stands, *Atmosphere-Ocean*, 44, 207–222, <https://doi.org/10.3137/ao.440301>, 2006.
- Beer, C., Porada, P., Ekici, A., and Brakebusch, M.: Effects of short-term variability of meteorological variables on soil temperature in permafrost regions, *The Cryosphere*, 12, 741–757, 2018.
- 10 Bellisario, L. M., Boudreau, L. D., Verseghy, D. L., Rouse, W. R., and Blanken, P. D.: Comparing the performance of the Canadian land surface scheme (CLASS) for two subarctic terrain types, *Atmosphere-Ocean*, 38, 181–204, <https://doi.org/10.1080/07055900.2000.9649645>, 2000.
- Boeckli, L., Brenning, A., Gruber, S., and Noetzli, J.: Permafrost distribution in the European Alps: calculation and evaluation of an index map and summary statistics, *The Cryosphere*, 6, 807, 2012.
- 15 Brown, J., Ferrians, Jr, O. J., Heginbottom, J. A., and Melnikov, E. S.: Circum-Arctic map of permafrost and ground-ice conditions, US Geological Survey Reston, 1997.
- Brown, R., Bartlett, P., MacKay, M., and Verseghy, D.: Evaluation of snow cover in CLASS for SnowMIP, *Atmosphere-Ocean*, 44, 223–238, <https://doi.org/10.3137/ao.440302>, 2006.
- Brown, R. D., Brasnett, B., and Robinson, D.: Gridded North American monthly snow depth and snow water equivalent for GCM evaluation, *Atmosphere-Ocean*, 41, 1–14, <https://doi.org/10.3137/ao.410101>, 2003.
- 20 Chadburn, S., Burke, E., Essery, R., Boike, J., Langer, M., Heikenfeld, M., Cox, P., and Friedlingstein, P.: An improved representation of physical permafrost dynamics in the JULES land-surface model, *Geoscientific Model Development*, 8, 1493–1508, <https://doi.org/10.5194/gmd-8-1493-2015>, 2015a.
- Chadburn, S. E., Burke, E. J., Essery, R. L. H., Boike, J., Langer, M., Heikenfeld, M., Cox, P. M., and Friedlingstein, P.: Impact of model developments on present and future simulations of permafrost in a global land-surface model, *The Cryosphere Discuss.*, 9, 1965–2012, <https://doi.org/10.5194/tcd-9-1965-2015>, 2015b.
- 25 Chadburn, S. E., Burke, E. J., Cox, P. M., Friedlingstein, P., Hugelius, G., and Westermann, S.: An observation-based constraint on permafrost loss as a function of global warming, *Nat. Clim. Chang.*, 7, 340, <https://doi.org/10.1038/nclimate3262>, 2017.
- Clapp, R. B. and Hornberger, G. M.: Empirical equations for some soil hydraulic properties, *Water Resour. Res.*, 14, 601–604, <https://doi.org/10.1029/WR014i004p00601>, 1978.
- 30 Cosby, B. J., Hornberger, G. M., Clapp, R. B., and Ginn, T. R.: A Statistical Exploration of the Relationships of Soil Moisture Characteristics to the Physical Properties of Soils, *Water Resour. Res.*, 20, 682–690, <https://doi.org/10.1029/WR020i006p00682>, 1984.
- Côté, J. and Konrad, J.-M.: A generalized thermal conductivity model for soils and construction materials, *Can. Geotech. J.*, 42, 443–458, <https://doi.org/10.1139/t04-106>, 2005.
- 35 Dall’Amico, M., Endrizzi, S., Gruber, S., and Rigon, R.: A robust and energy-conserving model of freezing variably-saturated soil, *The Cryosphere*, 5, 469, 2011.



- Dankers, R., Burke, E. J., and Price, J.: Simulation of permafrost and seasonal thaw depth in the JULES land surface scheme, *The Cryosphere*, 5, 773–790, <https://doi.org/10.5194/tc-5-773-2011>, 2011.
- de Vries, D.: Thermal properties of soils, *Physics of Plant Environment*, 1963.
- Dickinson, R. E.: Land Surface Processes and Climate—Surface Albedos and Energy Balance, in: *Advances in Geophysics*, edited by Saltzman, B., vol. 25, pp. 305–353, Elsevier, [https://doi.org/10.1016/S0065-2687\(08\)60176-4](https://doi.org/10.1016/S0065-2687(08)60176-4), 1983.
- Dickinson, R. E., Henderson-Sellers, A., and Kennedy, P.: Biosphere/Atmosphere Transfer Scheme (BATS) Version 1e as coupled to the NCAR Community Climate Model, Tech. rep., Climate and Global Dynamics Division, National Center for Atmospheric Research, Boulder, Colorado, 1993.
- Ekici, A., Beer, C., Hagemann, S., and Hauck, C.: Simulating high-latitude permafrost regions by the JSBACH terrestrial ecosystem model, *Geoscientific Model Development*, 7, 631–647, 2014.
- Essery, R., Martin, E., Douville, H., Fernández, A., and Brun, E.: A comparison of four snow models using observations from an alpine site, *Clim. Dyn.*, 15, 583–593, <https://doi.org/10.1007/s003820050302>, 1999.
- Farouki, O. T.: The thermal properties of soils in cold regions, *Cold Reg. Sci. Technol.*, 5, 67–75, [https://doi.org/10.1016/0165-232X\(81\)90041-0](https://doi.org/10.1016/0165-232X(81)90041-0), 1981.
- Ganji, A., Sushama, L., Verseghy, D., and Harvey, R.: On improving cold region hydrological processes in the Canadian Land Surface Scheme, *Theor. Appl. Climatol.*, 127, 45–59, <https://doi.org/10.1007/s00704-015-1618-4>, 2015.
- Giorgi, F. and Avissar, R.: Representation of heterogeneity effects in Earth system modeling: Experience from land surface modeling, *Rev. Geophys.*, 35, 413–437, <https://doi.org/10.1029/97RG01754>, 1997.
- Gornall, J. L., Jónsdóttir, I. S., Woodin, S. J., and Van der Wal, R.: Arctic mosses govern below-ground environment and ecosystem processes, *Oecologia*, 153, 931–941, <https://doi.org/10.1007/s00442-007-0785-0>, 2007.
- Gray, D. M. and Male, D. H.: *Handbook of Snow: Principles, Processes, Management and Use*, Pergamon Press, 1981.
- Gruber, S.: Derivation and analysis of a high-resolution estimate of global permafrost zonation, *Cryosphere*, 6, 221–233, 2012.
- Gruber, S., Brown, N., Stewart-Jones, E., Karunaratne, K., Riddick, J., Peart, C., Subedi, R., and Kokelj, S.: Air and ground temperature, air humidity and site characterization data from the Canadian Shield tundra near Lac de Gras, Northwest Territories, Canada, v. 1.0 (2015–2017), <http://www.cen.ulaval.ca/nordicanad/dpage.aspx?doi=45561XD-2C7AB3DCF3D24AD8>, <https://doi.org/10.5885/45561XD-2C7AB3DCF3D24AD8>, accessed: 2018-11-13, 2018.
- GTN-P: Global Terrestrial Network for Permafrost Database: Active Layer Thickness Data (CALM-Circumpolar Active Layer Monitoring), 2016.
- Gubler, S., Fiddes, J., Keller, M., and Gruber, S.: Scale-dependent measurement and analysis of ground surface temperature variability in alpine terrain, *The Cryosphere*, 5, 431–443, <https://doi.org/10.5194/tc-5-431-2011>, 2011.
- Harris, I., Jones, P. D., Osborn, T. J., and Lister, D. H.: Updated high-resolution grids of monthly climatic observations—the CRU TS3.10 Dataset, *Int. J. Climatol.*, 34, 623–642, 2014.
- Hedstrom, N. R. and Pomeroy, J. W.: Measurements and modelling of snow interception in the boreal forest, *Hydrol. Process.*, 12, 1611–1625, 1998.
- Kobayashi, S., Ota, Y., Harada, Y., Ebata, A., Moriya, M., Onoda, H., Onogi, K., Kamahori, H., Kobayashi, C., Endo, H., Miyaoka, K., and Takahashi, K.: The JRA-55 Reanalysis: General Specifications and Basic Characteristics, *Journal of the Meteorological Society of Japan*, 93, 5–48, <https://doi.org/10.2151/jmsj.2015-001>, 2015.



- Koren, V., Schaake, J., Mitchell, K., Duan, Q.-Y., Chen, F., and Baker, J. M.: A parameterization of snowpack and frozen ground intended for NCEP weather and climate models, *J. Geophys. Res.*, 104, 19 569–19 585, <https://doi.org/10.1029/1999JD900232>, 1999.
- Koven, C. D., Riley, W. J., and Stern, A.: Analysis of Permafrost Thermal Dynamics and Response to Climate Change in the CMIP5 Earth System Models, *J. Clim.*, 26, 1877–1900, <https://doi.org/10.1175/JCLI-D-12-00228.1>, 2013.
- 5 Kulik, V. Y.: Water infiltration into soil (in Russian), *Gidrometeoizdat, Moscow*, 19878, 1978.
- Kushner, P. J., Mudryk, L. R., Merryfield, W., Ambadan, J. T., Berg, A., Bichet, A., Brown, R., Derksen, C. P., Déry, S. J., Dirkson, A., Flato, G., Fletcher, C. G., Fyfe, J. C., Gillett, N., Haas, C., Howell, S., Laliberté, F., McCusker, K., Sigmond, M., Sospedra-Alfonso, R., Tandon, N. F., Thackeray, C., Tremblay, B., and Zwiers, F. W.: Assessment of snow, sea ice, and related climate process in Canada’s Earth-System model and climate prediction system, *The Cryosphere*, 12, 1137–1156, 2018.
- 10 Lafleur, P. M., Skarupa, M. R., and Verseghy, D. L.: Validation of the Canadian land surface scheme (class) for a subarctic open woodland, *Atmosphere-Ocean*, 38, 205–225, <https://doi.org/10.1080/07055900.2000.9649646>, 2000.
- Lawrence, D. M., Slater, A. G., Romanovsky, V. E., and Nicolsky, D. J.: Sensitivity of a model projection of near-surface permafrost degradation to soil column depth and representation of soil organic matter, *J. Geophys. Res.*, 113, F02 011, <https://doi.org/10.1029/2007JF000883>, 2008.
- 15 Lawrence, P. J. and Chase, T. N.: Representing a new MODIS consistent land surface in the Community Land Model (CLM 3.0), *J. Geophys. Res.*, 112, G01 023, <https://doi.org/10.1029/2006JG000168>, 2007.
- Lee, H., Swenson, S. C., Slater, A. G., and Lawrence, D. M.: Effects of excess ground ice on projections of permafrost in a warming climate, *Environ. Res. Lett.*, 9, 124 006, <https://doi.org/10.1088/1748-9326/9/12/124006>, 2014.
- Letts, M. G., Roulet, N. T., Comer, N. T., Skarupa, M. R., and Verseghy, D. L.: Parametrization of peatland hydraulic properties for the Canadian land surface scheme, *Atmosphere-Ocean*, 38, 141–160, <https://doi.org/10.1080/07055900.2000.9649643>, 2000.
- 20 Lorant, M. M., Abbott, B. W., Blok, D., Douglas, T. A., Epstein, H. E., Forbes, B. C., Jones, B. M., Kholodov, A. L., Kropp, H., Malhotra, A., Mamet, S. D., Myers-Smith, I. H., Natali, S. M., O’Donnell, J. A., Phoenix, G. K., Rocha, A. V., Sonntag, O., Tape, K. D., and Walker, D. A.: Reviews and syntheses: Changing ecosystem influences on soil thermal regimes in northern high-latitude permafrost regions, *Biogeosciences*, 15, 5287–5313, <https://doi.org/10.5194/bg-15-5287-2018>, 2018.
- 25 MacDonald, M. K.: The Hydrometeorological Response to Chinook Winds in the South Saskatchewan River Basin, Ph.D. thesis, University of Edinburgh, 2015.
- Mellor, M.: Engineering Properties of Snow, *J. Glaciol.*, 19, 15–66, <https://doi.org/10.3189/S002214300002921X>, 1977.
- Melton, J. R. and Arora, V. K.: Sub-grid scale representation of vegetation in global land surface schemes: implications for estimation of the terrestrial carbon sink, *Biogeosciences*, 11, 1021–1036, <https://doi.org/10.5194/bgd-10-16003-2013>, 2014.
- 30 Melton, J. R. and Arora, V. K.: Competition between plant functional types in the Canadian Terrestrial Ecosystem Model (CTEM) v. 2.0, *Geoscientific Model Development*, 9, 323–361, <https://doi.org/10.5194/gmd-9-323-2016>, 2016.
- Melton, J. R., Sospedra-Alfonso, R., and McCusker, K. E.: Tiling soil textures for terrestrial ecosystem modelling via clustering analysis: a case study with CLASS-CTEM (version 2.1), *Geoscientific Model Development*, 10, 2761–2783, <https://doi.org/10.5194/gmd-10-2761-2017>, 2017.
- 35 MODIS Adaptive Processing System, NASA: MODIS/Terra+Aqua Albedo 16-Day L3 Global 0.05Deg CMG V005, title of the publication associated with this dataset: MODIS/Terra+Aqua Albedo 16-Day L3 Global 0.05Deg CMG V005, 2016.
- Morse, P. D., Burn, C. R., and Kokelj, S. V.: Influence of snow on near-surface ground temperatures in upland and alluvial environments of the outer Mackenzie Delta, Northwest Territories, *Can. J. Earth Sci.*, 49, 895–913, 2012.



- Mudryk, L. R., Derksen, C., Kushner, P. J., and Brown, R.: Characterization of Northern Hemisphere snow water equivalent datasets, 1981–2010, *Journal of Climate*, 28, 8037–8051, 2015.
- Myers-Smith, I. H., Forbes, B. C., Wilming, M., Hallinger, M., Lantz, T., Blok, D., Tape, K. D., Macias-Fauria, M., Sass-Klaassen, U., Lévesque, E., Boudreau, S., Ropars, P., Hermanutz, L., Trant, A., Collier, L. S., Weijers, S., Rozema, J., Rayback, S. A., Schmidt, N. M.,
5 Schaeppman-Strub, G., Wipf, S., Rixen, C., Ménard, C. B., Venn, S., Goetz, S., Andreu-Hayles, L., Elmendorf, S., Ravolainen, V., Welker, J., Grogan, P., Epstein, H. E., and Hik, D. S.: Shrub expansion in tundra ecosystems: dynamics, impacts and research priorities, *Environ. Res. Lett.*, 6, 045 509, 2011.
- Nicolisky, D. J., Romanovsky, V. E., Alexeev, V. A., and Lawrence, D. M.: Improved modeling of permafrost dynamics in a GCM land-surface scheme, *Geophys. Res. Lett.*, 34, <https://doi.org/10.1029/2007GL029525>, 2007.
- 10 Niu, G.-Y. and Yang, Z.-L.: Effects of Frozen Soil on Snowmelt Runoff and Soil Water Storage at a Continental Scale, *J. Hydrometeorol.*, 7, 937–952, <https://doi.org/10.1175/JHM538.1>, 2006.
- O'Neill, H. B., Wolfe, S. A., and Duchesne, C.: New ground ice maps for Canada using a paleogeographic modelling approach, *The Cryosphere Discuss.*, pp. 1–37, <https://doi.org/10.5194/tc-2018-200>, 2018.
- Paquin, J.-P. and Sushama, L.: On the Arctic near-surface permafrost and climate sensitivities to soil and snow model formulations in climate
15 models, *Clim. Dyn.*, 44, 203–228, <https://doi.org/10.1007/s00382-014-2185-6>, 2014.
- Pelletier, J. D., Broxton, P. D., Hazenberg, P., Zeng, X., Troch, P. A., Niu, G., Williams, Z. C., Brunke, M. A., and Gochis, D.: Global 1-km Gridded Thickness of Soil, Regolith, and Sedimentary Deposit Layers, <https://doi.org/10.3334/ORNDAAC/1304>, 2016.
- Peng, Y., Arora, V. K., Kurz, W. A., Hember, R. A., Hawkins, B. J., Fyfe, J. C., and Werner, A. T.: Climate and atmospheric drivers of historical terrestrial carbon uptake in the province of British Columbia, Canada, *Biogeosciences*, 11, 635–649, [20 11-635-2014](https://doi.org/10.5194/bg-20), 2014.
- Pomeroy, J. W. and Gray, D. M.: Snowcover accumulation, relocation and management, *Bulletin of the International Society of Soil Science* no. 88, 1995.
- Porada, P., Ekici, A., and Beer, C.: Effects of bryophyte and lichen cover on permafrost soil temperature at large scale, *The Cryosphere*, 10, 2291–2315, <https://doi.org/10.5194/tc-10-2291-2016>, 2016.
- 25 Riseborough, D., Shiklomanov, N., Eitzelmüller, B., Gruber, S., and Marchenko, S.: Recent advances in permafrost modelling, *Permafrost Periglacial Processes*, 19, 137–156, <https://doi.org/10.1002/ppp.615>, 2008.
- Roebber, P. J., Bruening, S. L., Schultz, D. M., and Cortinas, J. V.: Improving Snowfall Forecasting by Diagnosing Snow Density, *Weather Forecast.*, 18, 264–287, [https://doi.org/10.1175/1520-0434\(2003\)018<0264:ISFBDS>2.0.CO;2](https://doi.org/10.1175/1520-0434(2003)018<0264:ISFBDS>2.0.CO;2), 2003.
- Romanovsky, V. E. and Osterkamp, T. E.: Effects of unfrozen water on heat and mass transport processes in the active layer and permafrost,
30 *Permafrost Periglacial Processes*, 11, 219–239, 2000.
- Scott, D. W.: *Multivariate Density Estimation: Theory, Practice, and Visualization*, John Wiley & Sons, 1992.
- Shangguan, W., Dai, Y., Duan, Q., Liu, B., and Yuan, H.: A global soil data set for earth system modeling, *Journal of Advances in Modeling Earth Systems*, 6, 249–263, <https://doi.org/10.1002/2013MS000293>, 2014.
- Shangguan, W., Hengl, T., Mendes de Jesus, J., Yuan, H., and Dai, Y.: Mapping the global depth to bedrock for land surface modeling, *J. Adv. Model. Earth Syst.*, 9, 65–88, <https://doi.org/10.1002/2016MS000686>, 2017.
- Shiklomanov, N. I., Streletskiy, D. A., Little, J. D., and Nelson, F. E.: Isotropic thaw subsidence in undisturbed permafrost landscapes, *Geophys. Res. Lett.*, 40, 6356–6361, <https://doi.org/10.1002/2013GL058295>, 2013.



- Smerdon, J. E. and Stieglitz, M.: Simulating heat transport of harmonic temperature signals in the Earth's shallow subsurface: Lower-boundary sensitivities, *Geophys. Res. Lett.*, 33, 2006.
- Smith, M. W.: Microclimatic Influences on Ground Temperatures and Permafrost Distribution, Mackenzie Delta, Northwest Territories, Can. *J. Earth Sci.*, 12, 1421–1438, <https://doi.org/10.1139/e75-129>, 1975.
- 5 Soulis, E. D., Snelgrove, K. R., Kouwen, N., Seglenieks, F., and Verseghy, D. L.: Towards closing the vertical water balance in Canadian atmospheric models: Coupling of the land surface scheme class with the distributed hydrological model watflood, *Atmosphere-Ocean*, 38, 251–269, <https://doi.org/10.1080/07055900.2000.9649648>, 2000.
- Sturm, M., Holmgren, J., König, M., and Morris, K.: The thermal conductivity of seasonal snow, *J. Glaciol.*, 43, 26–41, <https://doi.org/10.1017/S002214300002781>, 1997.
- 10 Tian, Z., Lu, Y., Horton, R., and Ren, T.: A simplified de Vries-based model to estimate thermal conductivity of unfrozen and frozen soil, *Eur. J. Soil Sci.*, 67, 564–572, <https://doi.org/10.1111/ejss.12366>, 2016.
- Tilley, J. S., Chapman, W. L., and Wu, W.: Sensitivity tests of the Canadian Land Surface Scheme (CLASS) for Arctic tundra, *Ann. Glaciol.*, 25, 46–50, <https://doi.org/10.1017/s0260305500013781>, 1997.
- Turetsky, M. R., Bond-Lamberty, B., Euskirchen, E., Talbot, J., Frolking, S., McGuire, A. D., and Tuittila, E.-S.: The resilience and functional
15 role of moss in boreal and arctic ecosystems, *New Phytol.*, 196, 49–67, <https://doi.org/10.1111/j.1469-8137.2012.04254.x>, 2012.
- UNESCO Press: Discharge of selected rivers of the world, vol. 2, part 2. Mean Monthly and Extreme Discharges, 1965–1984., Tech. rep., UNESCO, Paris, 1993.
- Van Der Wal, R. and Brooker, R. W.: Mosses mediate grazer impacts on grass abundance in arctic ecosystems, *Funct. Ecol.*, 18, 77–86, <https://doi.org/10.1111/j.1365-2435.2004.00820.x>, 2004.
- 20 Vaughan, D. G., Comiso, J. C., Allison, I., Carrasco, J., Kaser, G., Kwok, R., Mote, P., Murray, T., Paul, F., Ren, J., Rignot, E., Solomina, O., Steffen, K., and Zhang, T.: Observations: Cryosphere, in: *Climate Change 2013 - The Physical Science Basis*, edited by Stocker, T. F., Qin, D., K. Plattner, G., Tignor, M., Allen, S. K., Boschung, J., Nauels, A., Xia, Y., Bex, V., and Midgley, P. M., Working Group I to the Fifth Assessment Report of the Intergovernmental Panel on Climate Change, pp. 317–382, Cambridge University Press, Cambridge, <https://doi.org/10.1017/CBO9781107415324.012>, 2013.
- 25 Verseghy, D.: CLASS – The Canadian land surface scheme (v. 3.6.2), Climate Research Division, Science and Technology Branch, Environment Canada, 2017.
- Viovy, N.: CRU-NCEP Version 8, title of the publication associated with this dataset: CRU-NCEP version 8, 2016.
- Watanabe, K. and Mizoguchi, M.: Amount of unfrozen water in frozen porous media saturated with solution, *Cold Reg. Sci. Technol.*, 34, 103–110, [https://doi.org/10.1016/S0165-232X\(01\)00063-5](https://doi.org/10.1016/S0165-232X(01)00063-5), 2002.
- 30 Wen, Z., Ma, W., Feng, W., Deng, Y., Wang, D., Fan, Z., and Zhou, C.: Experimental study on unfrozen water content and soil matric potential of Qinghai-Tibetan silty clay, *Environ. Earth Sci.*, 66, 1467–1476, <https://doi.org/10.1007/s12665-011-1386-0>, 2012.
- Wiscombe, W. J. and Warren, S. G.: A Model for the Spectral Albedo of Snow. I: Pure Snow, *J. Atmos. Sci.*, 37, 2712–2733, [https://doi.org/10.1175/1520-0469\(1980\)037<2712:AMFTSA>2.0.CO;2](https://doi.org/10.1175/1520-0469(1980)037<2712:AMFTSA>2.0.CO;2), 1980.
- Wu, Y., Verseghy, D. L., and Melton, J. R.: Integrating peatlands into the coupled Canadian Land Surface Scheme (CLASS) v3.6 and the
35 Canadian Terrestrial Ecosystem Model (CTEM) v2.0, *Geoscientific Model Development*, 9, 2639–2663, <https://doi.org/10.5194/gmd-9-2639-2016>, 2016.
- Yang, Z.-L., Dickinson, R. E., Robock, A., and Vinnikov, K. Y.: Validation of the snow submodel of the Biosphere–Atmosphere Transfer Scheme with Russian snow cover and meteorological observational data, *J. Clim.*, 10, 353–373, 1997.



- Zhang, T., Barry, R. G., Knowles, K., Heginbottom, J. A., and Brown, J.: Statistics and characteristics of permafrost and ground-ice distribution in the Northern Hemisphere, *Polar Geogr.*, 23, 132–154, <https://doi.org/10.1080/10889379909377670>, 1999.
- Zhang, T., Heginbottom, J. A., Barry, R. G., and Brown, J.: Further statistics on the distribution of permafrost and ground ice in the Northern Hemisphere, *Polar Geogr.*, 24, 126–131, <https://doi.org/10.1080/10889370009377692>, 2000.
- 5 Zhang, Y., Carey, S. K., and Quinton, W. L.: Evaluation of the algorithms and parameterizations for ground thawing and freezing simulation in permafrost regions, *J. Geophys. Res.*, 113, D17 116, <https://doi.org/10.1029/2007JD009343>, 2008.
- Zhao, L. and Gray, D. M.: A parametric expression for estimating infiltration into frozen soils, *Hydrological Processes*, 11, 1761–1775, [https://doi.org/10.1002/\(SICI\)1099-1085\(19971030\)11:13<1761::AID-HYP604>3.0.CO;2-O](https://doi.org/10.1002/(SICI)1099-1085(19971030)11:13<1761::AID-HYP604>3.0.CO;2-O), <https://onlinelibrary.wiley.com/doi/abs/10.1002/%28SICI%291099-1085%2819971030%2911%3A13%3C1761%3A%3AAID-HYP604%3E3.0.CO%3B2-O>, 1997.
- 10 Zobler, L.: A world soil file for global climate modelling, title of the publication associated with this dataset: NASA Technical Memorandum 87802, 1986.